NASA TN D-1001

N16 1665

NASA

TECHNICAL NOTE

D-1001

THERMAL DESIGN OF EXPLORER XIII MICROMETEOROID SATELLITE

By Earl C. Hastings, Jr., Richard E. Turner,
and Katherine C. Speegle

Langley Research Center
Langley Station, Hampton, Va.

NATIONAL AERONAUTICS AND SPACE ADMINISTRATION

WASHINGTON   May 1962

LD

TABLE OF CONTENTS

Page

NATIONAL AERONAUTICS AND SPACE ADMINISTRATION

TECHNICAL NOTE D-1001

THERMAL DESIGN OF EXPLORER XIII MICROMETEOROID SATELLITE

By Earl C. Hastings, Jr., Richard E. Turner,
and Katherine C. Speegle

SUMMARY

The preflight thermal design study of the Explorer XIII (1961 Chi) micrometeoroid impact research satellite has established that with the coatings selected the telemetry systems can be maintained within their temperature operating limits of 15° F to 120° F from launch to injection into orbit, and also for the lifetime of the satellite in orbit. Surface temperatures of the exposed experiments have also been found to remain within their prescribed limits. Ascent heating studies indicated that during the ascent with the heat shield in place, the payload pressure cell temperature should increase 38° F and the other sensors less than 20° F. Telemetry temperatures showed no increase in this phase of the flight. After ejection of the heat shield during ascent, studies indicate that no aerodynamic heating effects will occur. An additional source of heating to the satellite is the last-stage rocket-motor case which is an integral part of the satellite. Temperatures of the motor case during burning and after burnout were estimated to raise the temperatures of some of the sensors near the motor nozzle by about 90° F. These sensors still remain within tolerable limits however.

The largest variation in telemetry temperature could occur during the orbit heating phase for the satellite spinning about the principal axis of least inertia. Extremely low telemetry temperatures could occur in this case if long periods of spin about this axis should occur. If, as studies indicate, the satellite tumbles approximately 2 weeks after launch, then this cold condition can be avoided with proper selection of launch time. After transition to the tumbling mode of spin the maximum and minimum telemetry temperatures were found to be 115° F and 30° F, respectively. The computation of the telemetry temperature was found to be appreciably affected by thermal conductivity within the satellite itself. In the tumbling mode of spin it was necessary to consider the existence of hot and cold spots on the external surfaces due to nonuniform heating. These surface gradients were found to be quite large for some materials and satellite orientations although the exposed sensors still remained within tolerable temperature values when these effects were considered. An extensive test program, as part of the thermal design study, proved invaluable in supplying engineering type answers over a wide range of subjects. In many cases, test procedures were useful in verifying estimated values, evaluating coatings and materials for the space environment, or experimentally determining data which could not be estimated with a great degree of accuracy.

INTRODUCTION

The Explorer XIII (1961 Chi) satellite was developed by the Applied Materials and Physics Division at the Langley Research Center as part of an NASA program to study the penetration hazard of micrometeoroids in space, and was placed into a near earth orbit from the NASA Wallops Station by the Scout launch vehicle. The satellite was designed to supply information on the probability of penetrations of spacecraft skins and also on micrometeoroid flux rates at altitudes between about 200 and 500 nautical miles.

Because of the relatively narrow temperature ranges over which the electronics and some of the sensors can operate, it was necessary to select coatings, materials, and heat-transfer paths which would provide acceptable temperature environments for these components during the lifetime of the satellite. The purpose of this paper is to discuss some of the analytical and experimental methods used in connection with this phase of the satellite development. Consideration is given to heat transfer in four different regimes; ascent heating with the satellite enclosed in a protective heat shield, ascent heating after ejection of the heat shield, and orbit heating for the period of 1 year. Since the satellite was constructed around the last stage of the booster (which is placed in orbit as a part of the satellite) it was also necessary to consider the effect of heat transfer from the rocket motor case to the satellite.

In the orbit heating phase of the study, emphasis is placed on some considerations which often receive only casual attention in the literature. These items include a description of an analytical program which considered radiative and conductive heat exchange between component parts of the satellite, defining the hottest and coldest orbit passes, comparative effects of spin stabilization and tumbling rotation on telemetry temperatures and surface temperature, and a discussion of the influence of the hour of launch. Materials test data which may be of general interest are also presented.

SYMBOLS

A area

a thermal accommodation coefficient, $\dfrac{T_r - T_{i,1}}{T_w - T_{i,1}}$

a_s absorptivity of solar radiation

c	specific heat of materials, $Btu/lb\text{-}^\circ R$
c_p	specific heat of air at constant pressure, $Btu/slug\text{-}^\circ F$
e	total hemispherical emissivity
f	shape factor
G_i	internal heat generated, Btu/min
$\overline{H}$	total angular momentum, $slug\text{-}ft^2/sec$
h	conduction coefficient, $Btu/^\circ F\text{-}min$
J	radiant heat intensity, $Btu/min\text{-}in.^2$
K	Boltzmann constant, 1.38×10^{-16} $ergs/^\circ K$
k	thermal conductivity, $Btu/in.\text{-}min\text{-}^\circ F$
l	distance, ft
m	pound mass
m_m	molecular mass, g
N	dimensionless flux factor
N_{Pr}	Prandtl number
N_{St}	Stanton number
n	number of molecules per cubic centimeter
P	orbit period, min
p	percent time in sunlight per orbit pass
q	heat-transfer rate, $Btu/ft^2\text{-}sec$
R	radiation coefficient, $Btu/^\circ R^4\text{-}min$
$\overline{R}_e$	mean radius of earth, 3,438 nautical miles
r	recovery factor, $\dfrac{T_{aw} - T_l}{T_t - T_l}$

r_e earth-atmosphere albedo, 0.4

S solar constant, 0.04968 Btu/in.^{2}-min

$s = \dfrac{V}{\bar{v}}$

T temperature, $^O F$ or $^O R$

T_∞ free-stream temperature

t thickness of material

V velocity, ft/sec

$\bar{v}$ mean molecular particle velocity, ft/sec

α angle between line from satellite to center of earth and line from satellite to element on earth surface, deg

α^2 thermal diffusivity of material, $\dfrac{k}{\rho c}$

γ_0 angle between satellites momentum vector projection on orbit plane and local horizon at orbit perigee, deg

δ orbit angle, deg (zero at perigee)

ϵ angle between sun's unit vector and orbital plane, deg

ζ angle between perigee and projection of sun's unit vector on orbit plane, deg

η angle between line from center of emitting source to satellite and satellite principal axis, deg

η_s angle between line from center of earth to sun and satellite angular momentum vector

θ angle between line from center of earth to satellite and line from center of earth to element on earth surface

θ_s angle between line from center of earth to sun and line from center of earth to satellite

Λ angular displacement of point on surface of cylinder measured from angular momentum vector

ν angle between angular momentum vector and orbit plane

$\xi = \delta - \zeta$

ρ density, lb/ft^3 or $slug/ft^3$

ρ_0 radius of hemisphere or cylinder

σ Stefan-Boltzmann constant, 2.00×10^{-13} $Btu/in.^2\text{-}min\text{-}^\circ R^4$

τ time, sec or min

Φ radiant heat flux, Btu/min

ϕ azimuth angle in spherical coordinates, deg

Ω for circular orbits, angular displacement of satellite in sunlight between darkness intersections

Ω_0 longitude of descending node

Subscripts:

a   air

aw   adiabatic wall

c   cross sectional

e   earth

i,1   incident molecule stream

l local

m   mean

p   projected

r   reflected molecule stream

rs   reflected solar

s   solar

T   total

w   wall

SATELLITE AND LAUNCH VEHICLE

Satellite

The general arrangement of the Explorer XIII (1961 Chi) satellite consists of the forward nose-cone section and three separate groups of sensors, all permanently attached to the last stage of the launch vehicle (shown by the dashed lines in fig. 1). Five types of sensors are used as can be seen in this figure.

Mounted around the exterior surface of the fourth-stage (ABL-X-248-A5) rocket motor are 160 pressurized cells made of beryllium copper of various thicknesses between 0.001 inch and 0.005 inch. Each cell is about 2 inches in diameter and 7.40 inches long. The cells are mounted to an aluminum inner heat shield encircling the rocket-motor case as can be seen from the enlarged cross-sectional sketch. These cells are pressurized with helium so that a puncture by a micrometeoroid will allow pressure to leak out. By means of a pressure activated switch located on the bottom of each cell, the pressure loss can be detected and telemetered.

Two additional micrometeoroid experiments, developed by the Lewis Research Center and the Goddard Space Flight Center, are mounted around the fourth-stage transition section. The Lewis Research Center experiment is composed of 60 grid detectors made of type 304 stainless steel of thicknesses between 0.003 and 0.006 inch. Beneath each of the steel segments is a printed circuit about 60 microinches thick attached to 1/4-mil-thick Mylar.

The experiment developed by the Goddard Space Flight Center consists of 46 sensors, each consisting of one continuous winding of enameled copper wire on a rectangular melamine laminate card. The wires used for winding were 0.002 inch and 0.003 inch in diameter. Both the Lewis and Goddard sensors record micrometeroid penetrations by indicating a change in resistance when the sensor circuit is broken.

As indicated in figure 1, the nose cone is also instrumented with two additional detectors developed by the Goddard Center. These are cadmium sulfide cells which are mounted in aluminized lucite glass flasks covered with a sheet of 1/4-mil-thick Mylar coated with aluminum on both sides. When small particles penetrate this sheet, light enters the flask and is focused on the cadmium sulfide cell causing a change in its resistance. Piezoelectric impact detectors are mounted on two separate sounding boards on the nose cone to record impacts received on the boards. The same type of sensor is also used on the bottom of the pressure cells.

The cadmium sulfide detectors and sounding boards were attached to the nose cone which was made of sandblasted 410 stainless steel. Two

large power solar cell groups and three small solar cell groups for various test purposes were mounted on the forward flat face, and eight large and two small solar cell groups were mounted on an aluminum ring which was located around the cylindrical part of the nose cone. A photograph of the nose cone is shown in figure 2.

The two PIM/FM/AM telemeter canisters were mounted to a fiber-glass bulkhead serving as the base of the nose cone. A photograph of this assembly on the satellite is shown in figure 3. Table I is a description of the materials and surface coatings used on Explorer XIII.

Total payload weight (excluding the last-stage rocket motor) is 125 pounds. The payload weight plus burned-out motor weight is approximately 190 pounds.

Launch Vehicle and Trajectory

The launch vehicle for the Explorer XIII satellite was the Scout developed at the Langley Research Center. A drawing of the Scout is shown in figure 4 and a photograph of the launch vehicle prior to launch is shown in figure 5. Scout is a four-stage solid-fuel launch vehicle, capable of orbiting payloads of about 150 pounds. A more detailed discussion of the "Scout" launch vehicle can be found in reference 1.

Nominal Trajectory

The satellite was launched from the NASA Wallops Station at an elevation angle of 80° and an azimuth angle of 90° from true north. Figure 6 is a plot of the estimated ascent trajectory profile with a notation of ignition and burnout of the various stages. The trajectory parameters which effect the ascent heating of the vehicle through third-stage burnout (altitude and velocity) are plotted as a function of flight time in figure 7 for a particle, spherical, nonrotating earth trajectory. The ignition and burnout points as computed for a particle trajectory and an oblate, rotating earth are shown for comparison.

An azimuth plot is shown in figure 8 where predicted impact of the stages is also noted. Typical track of subsatellite point after injection into orbit is shown in figure 9. Injection point, initial apogee, and initial perigee as well as the locations of Minitrack receiving stations are also shown in this figure. Estimated injection conditions and orbit characteristics are as follows for the nominal trajectory:

Injection inertial velocity, ft/sec 25,708
Injection inertial flight-path angle, deg . . . . -0.47

Geodetic latitude at injection, deg N. 35.85
Longitude at injection, deg W. . . . .   -56.31
Geodetic azimuth at injection, deg from N. 104.15
Orbit perigee, nautical miles   207
Orbit apogee, nautical miles   527
Orbit inclination with respect to equator, deg 38.0
Orbit period, min 98.1

Subsequent to the work discussed herein, Explorer XIII was placed
into orbit from the NASA Wallops Station in August of 1961. Apparently
as a result of a large tipoff angle, the actual trajectory flown by the
satellite was much different from the nominal trajectory used in this
paper, and the lifetime in orbit was only about 2.5 days. Therefore no
attempt will be made in this paper to correlate flight data with the
estimates presented.

ANALYSIS AND DISCUSSION

As is well known, the function of the thermal design of a satellite
is that of temperature control during both the ascent and orbiting phases
of the satellite operation. Although this control is sometimes thought
of in terms of telemetry temperature, it is equally important for all
parts of the satellite where surface temperatures can cause permanent
damage or a decrease in reliability. This was particularly true in the
case of the Explorer XIII satellite where so many of the experiments
were mounted externally. The experimentally determined maximum and
minimum temperature limits which were the design values for Explorer XIII
are listed in the following table. These values do not necessarily
represent temperatures where permanent damage would occur but represent
values which the designers or experimenters felt might impare reliability
or accuracy.

Component	Maximum allowable temperature, °F	Minimum allowable temperature, °F
Telemetry	120	15
Pressure cells	250	-50
Lewis foil gages	180	-100
Goddard wire cards	300	None given
Solar cells	250	-50
Cadmium sulfide cells	200	None given
Impact detectors	250	-50

The first phase of the thermal design was concerned with the satel-
lite surface temperatures from launch until injection into orbit. This

ascent heating phase was studied in two parts. The surface temperatures of the satellite experienced by radiation from the heat shield were determined analytically and by prefiring ground tests from launch until cover ejection. After cover ejection, analytical methods were used to estimate the maximum temperature rise to be experienced by the pressure cells during this part of the ascent flight.

Ascent Heating - Cover On

Computing method.- From launch until ignition of the third-stage rocket motor, the satellite is enclosed in a protective heat shield as is shown in figure 10. A photograph of Explorer XIII with a half section of the heat shield installed is shown in figure 11. The hemispherical blunt nose tip is made of 0.125-inch-thick stainless steel and the conical and cylindrical sections are made of two layers of 0.05-inch-thick laminated glass phenolic separated by a 0.50-inch-thick inner core of glass-fiber batting, as shown in figure 10. Temperatures have been predicted for three locations on the heat shield; stagnation point of the hemispherical nose, conical section, and the cylindrical section. The locations of these stations are also shown in figure 10.

The calculations of stagnation-point temperature time histories were performed on an IBM 7090 electronic data processing system, using a particle-trajectory for a spherical nonrotating earth. This program assumes the wall is thermally thin which indicates the mean temperature of the wall is very close to the outside surface temperature with the inside surface insulated. The thermal properties of the 0.125-inch-thick stainless steel at the stagnation point, and the low accelerations of the Scout motors combine to make a thin-wall solution adequate since temperature rates of change are low and near equilibrium temperatures exist.

For velocities less than 3,000 ft/sec, the stagnation-point heat-transfer theory of Sibulkin (ref. 2) was used to obtain convective heating rates. The theory used for velocities above 3,000 ft/sec is a modification of the theory of Fay and Riddell discussed in reference 3. The latter theory indicates the real gas effects. The program includes only the quantities of heat contributed by convection and lost by radiation. Temperature is computed step by step from the equation
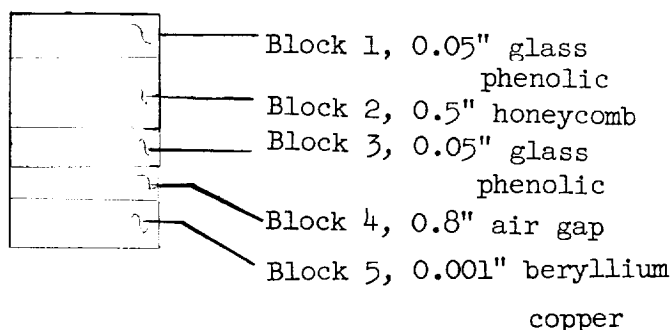
$$\Delta T = \frac{d\tau}{\rho_w t_w c_w}\left(q_{convection} - q_{radiation}\right) \tag{1}$$

and

$$q_{radiation} = e\sigma T_w^4 \tag{2}$$

The IBM 7090 system is also programed to handle thick-wall problems involving the temperature rise in solids, parts of which may be of different materials. The materials may also be separated by mechanical joints or air gaps. The program is set up to include the quantities of heat transmitted by convection, conduction, and radiation. The composition of the glass phenolic walls of the heat shield on the conical and cylindrical sections necessitated the use of this program for calculating the temperatures on these sections.

In order to apply the thick-wall solution, the heat-shield cross section is analytically divided into a number of small volumes or blocks and the general method of Dusinberre (ref. 4) is used to set up heat-balance equations for each block. The temperature of each block is then obtained by making a simultaneous solution of all the heat-balance equations by an iterative process. The following diagram is a typical cross-sectional block diagram:

Block 1, 0.05" glass phenolic
Block 2, 0.5" honeycomb
Block 3, 0.05" glass phenolic
Block 4, 0.8" air gap
Block 5, 0.001" beryllium copper

Convective heating rates for block 1 were determined from the equation

$$q = N_{St}(\rho V c_p)_l (T_{aw} - T_1) \tag{3}$$

The nondimensional heat-transfer coefficient N_{St} was obtained from turbulent theory of Van Driest (ref. 5) which can be applied for both flat-plate and conical surfaces. The adiabatic wall temperature T_{aw} was obtained from the definition of recovery factor r where

$$r = \frac{T_{aw} - T_l}{T_T - T_l} \tag{4}$$

and the turbulent recovery factor was assumed equal to $N_{Pr}^{1/3}$. The local conditions, Mach number, velocity, density, and temperature were obtained by using reference 6.

The radiative heating rate for a block I separated from a radiant source II by an air gap was obtained from the equation

$$q_{radiation} = \frac{\sigma\left(T_{II}^4 - T_I^4\right)}{\frac{1}{e_I} + \frac{1}{e_{II}} - 1} \tag{5}$$

and the external radiation was computed from the equation

$$q_{radiation} = -e_I\sigma T_I^4 \tag{6}$$

The equation for the conduction between blocks 1 and 2 is

$$q_{conduction} = \frac{k_1\left(T_2 - T_1\right)}{l} \tag{7}$$

If block 1 is separated from block 2 by an air mass

$$q_{conduction} = \frac{k_A\left(T_2 - T_1\right)}{l} \tag{8}$$

The thermal properties of the materials of the heat shield which were subjected to aerodynamic heating are given in the following table. The thermal properties of the payload pressure cells are also included.

Material	$k,$ Btu/sec-ft-$^\circ$F	$\rho_w,$ lb/ft^3	$c,$ Btu/lb-$^\circ$R	e
Stainless steel Glass phenolic Beryllium copper	0.264 × 10^{-4} .061	494 112 516	0.139 .277 .09	0.8 .8 .16

Temperature time histories.- The estimated temperature at the stagnation point (station (1)) during ascent is shown in figure 12 from launch to 138 seconds. The heat loss to the payload was not included in the stagnation-point temperature computation.

Station (2) was on the conical section of the shield at a point 10 inches along the surface from the nose tip. The temperatures plotted in figure 13 were computed by assuming that the honeycomb inner core functioned as air as an insulator between the two layers of glass phenolic. No heat loss to the payload was included in the calculations of temperatures of the conical section. The station chosen for calculating temperatures on the cylindrical section of the heat shield was 32.5 inches along the surface from the stagnation point (or at a point above the first row of pressure cells). The temperature time history of the heat shield and the pressure cells at this point (station (3)) is shown in figure 14 from launch until heat shield ejection. Figure 14 indicates a maximum inside-wall temperature for the cylinder of 185° F at cover release and a temperature of 155° F on the thinnest pressure cell at that time. In comparing the outer-surface temperatures at the three stations, it can be seen that temperatures at stations (2) and (3) are considerably higher than at the stagnation point (station (1)) over a large portion of the ascent. This can be explained by considering that the nose-cone cap is steel but the cone and cylinder are glass phenolic. The much lower thermal conductivity of the phenolic restricts the inward transfer of heat away from the outside surface by conductivity resulting in the higher surface temperatures shown, although the heat flux experienced at stations (2) and (3) is generally lower than at station (1).

No attempt was made to estimate the change in telemetry temperature during this phase of the ascent since this change should be quite small. The combined effects of thermal isolation of the telemetry packs and the relatively short ascent heating period should have a negligible influence on telemetry temperatures.

Simulated ascent heating.- A preflight test was conducted by using the prototype Explorer XIII satellite mounted inside a protective heat shield of the type discussed (fig. 11). The satellite was instrumented with thermocouples on the various experiment surfaces and in the telemetry

packs. The heat shield was also instrumented with thermocouples at
various longitudinal stations on the outside and inside walls. Banks
of quartz lamps enclosing the conical and cylindrical sections of the
heat shield were used as the heat-flux source. The estimated external
surface temperatures given in figures 13 and 14 were used as the programer
temperatures for the conical and cylindrical sections, respectively. Fig-
ure 15 is a sketch of the test setup showing three programed temperature
locations. The same time history was used for both stations 2 and 3. A
comparison of programed and measured temperatures at these stations is
shown in figure 16. This figure indicates very close duplication of the
temperature rise and the maximum temperature estimated. The cooling rate
in the test was slower than that predicted at each station, possibly as a
result of the room environment. The effect, however, is that the test was
slightly more severe than was predicted from 42 seconds to cover ejection
at 138 seconds.

Some results of this preflight test are shown in figure 17 where the
calculated surface temperature of a 0.001-inch-thick pressure cell during
ascent is compared with the most severe measured value on a cell of the
same thickness. Surface temperatures of the Lewis and Goddard sensors
are also shown. The data of figure 17 show surface temperature rises of
38° F for the pressure cells and less than 20° F for the Lewis and
Goddard sensors. Although not shown in this figure, an examination of
the measured temperature time history of the telemetry pack showed no
discernible rise during this phase of the ascent.

It is indicated by analysis and experiment that during the ascent
with cover on, the surface temperatures should remain below their upper
limit values, and the increase in telemetry temperature should be negli-
gible.

Ascent Heating - Cover Off

The programed ascent trajectory of Explorer XIII called for release
of the payload cover and third-stage ignition to occur at an altitude of
350,000 feet. Estimates were made to determine whether the exposed
experiments of the satellite would experience "aerodynamic" heating in
the altitude range from 300,000 to 400,000 feet with the cover off.
Reference 7 treats the subject of heating in free-molecule flow and was
used for the computations discussed herein since the satellite will be
in this flow regime after cover release. The estimates are made for the
case of an idealized pressurized cell with a free-molecule heating flux
and surface radiation. Solar heating is neglected in these calculations.
This effect is discussed in detail in other sections of this paper, but
was not considered here, in an attempt to isolate the heating due solely
to free-molecule flow.

For a perfectly conducting cylinder at hypersonic speeds, the temperature of the radiating surface subject to the energy flux in free-molecule flow can be expressed

$$T = \left(\frac{\sqrt{2} a n K^{3/2} T_\infty^{3/2} s^2}{\sqrt{m_m} e \sigma}\right)^{1/4} N^{1/4} \qquad (9)$$

where

m_m molecular mass, 47.7×10^{-24} g (for nitrogen)

$\sigma = 5.76 \times 10^{-5}$ ergs/cm^2-sec-$^\circ$K^4

The temperature T_∞ is expressed in $^\circ$K.

The dimensionless parameter N is dependent upon the shape and orientation of the body. For a cylinder, of radius ρ_0 and length l, parallel to the flow

$$N = \frac{1}{2\sqrt{\pi}\left(1 + \frac{\rho_0}{l}\right)} \times \frac{\rho_0}{l} \qquad (10)$$

and for the case considered herein had a value of 0.035. To make the calculations as conservative as possible, the accommodation coefficient a was taken as unity. The use of equation (9) to compute T involved merely finding the particle speed, number of particles, and the free-stream temperature from altitude tables (ref. 8). A summary of the results of these calculations is presented in the following table:

Altitude of exposed cylinder, ft	Satellite velocity, ft/sec	Temperature rise due to free-molecule heating, $^\circ$F
300,000	9,000	25
302,000	9,000	11
303,400	9,000	0
350,000	9,000	0
400,000	9,000	0

Although these estimates are not very elaborate they serve to illustrate that the effect of free-molecule heating after cover release will be negligible for the conditions discussed and that space radiation heat transfer is by far the greater factor in this case. Surface and telemetry temperatures as influenced by radiation heat transfer in the space environment will be discussed in later sections of the paper.

Payload Heating Due to Elevated Rocket-Motor

Temperatures

As mentioned previously, the Explorer XIII payload is permanently attached to the last stage of the launch vehicle which goes into orbit with the payload. As a result, the temperature of the rocket-motor case has an influence on the temperatures of the satellite. Figure 18 shows experimentally determined temperature time histories from the static firing of a motor quite similar to the last stage of the Scout launch vehicle (ref. 9). The data in this figure indicate that following ignition of the last stage ($\Delta_T = 0$), temperatures of the rocket motor generally reach maximum values by about $\Delta_T = 500$ seconds and then decrease with increasing time.

An analytical program was used to consider the influence of the nozzle temperature (point 5) and the motor-case temperature (point 3), on the pressure cells and Lewis and Goddard sensors. To be as conservative as possible, a constant T at point 5 of 600° F and a constant T at point 3 of 400° F were assumed to exist from $\Delta_T = 0$ minute to $\Delta_T = 28$ minutes. Direct and reflected solar radiation and earth thermal radiation were also taken into account. The results are shown in figure 19.

These data show a constant increase in the temperature of the Lewis sensors after $\Delta_T = 4$ minutes with a value near the upper limit at $\Delta_T = 28$ minutes where the satellite enters the earth shadow. However, these calculations are highly conservative since figure 19 shows values of source temperatures after $\Delta_T \approx 600$ seconds which are much less than the constant 600° F and 400° F values which were used in these estimates. Figure 19 indicates temperatures of 142° F and 122° F for the last row of pressure cells and the Goddard sensors, respectively, at $\Delta_T = 28$ minutes. The decrease in sensor temperatures from $\Delta_T = 0$ to $\Delta_T \approx 4$ minutes indicates an initial cooling due to radiation before the effect of rocket-motor temperatures were felt by the sensors.

This phase of the thermal-design study indicated that although a considerable rise in the temperature of the sensors is associated with rocket-motor heating, the sensors remain within their temperature limits when this source of heating is considered. A preflight ground test

established that a constant temperature of 120° F on the Lewis sensors for 28 minutes did not affect the telemetry temperature.

Orbit Heating

A number of very good papers discussing the mechanics of orbit heating and passive thermal control using external coatings have been published (for example, refs. 10 to 13). For this reason only a brief review of these factors is presented in this section of the paper, although the equations used are derived in appendix A.

The sources of heat received by a satellite in orbit are the sun, earth, and instrumentation onboard the satellite. Thermal design in orbit is concerned with the temperatures of the satellite resulting from these heating sources. The radiant energy received from the sun at short wavelengths is determined by the solar absorptivity a_s and the energy radiated away by the surface is influenced by the total hemispherical emissivity e. By selecting surfaces or coatings with the proper ratio of a_s to e, it is possible to control surface temperatures (and therefore the mean temperature) within certain limits.

To illustrate, the general heat-flux equation expressed in equation (A4) of appendix A is

$$mc\left(\frac{dT}{d\tau}\right) = \Phi_s a_s + \Phi_{rs} a_s + \Phi_e e - A_T e \sigma T^4$$

For the equilibrium conditions with the sun and earth, the time derivative is zero and the mean satellite temperature is

$$T_m^4 = \frac{\left(\Phi_s\right)_m a_s}{A_T \sigma e} + \frac{\left(\Phi_{rs}\right)_m a_s}{A_T \sigma e} + \frac{\left(\Phi_e\right)_m}{A_T \sigma} \tag{11}$$

where

$$\Phi_m = \frac{1}{P} \int_0^P \Phi \, d\tau$$

Since the largest heat flux comes from the direct solar radiation (as expressed by the first term) it is important to select external coatings for the satellite outer shell which will produce mean temperatures over which the telemetry can operate.

In practical terms, however, the problem of thermal design is to consider the combined effects of all the exposed sectors of the satellite. Explorer XIII is a good illustration of this additional complexity. In this case there are a number of separate exposed sectors having different coatings and heat-sink capacities. Table II presents some material properties used for the exposed surfaces of Explorer XIII. The different temperatures of the sectors result in conductive and radiative heat exchange which influence the telemetry temperature in a different manner than would be estimated for the general case of equation (11). The analytical and experimental approaches to the thermal design of Explorer XIII in orbit consisted of several phases which are now discussed.

Digital computer program.- The IBM 7090 Electronic Data Processing System was used to compute the satellite temperatures in orbit. A digital program was set up on the basis of the heat flow paths shown schematically in figure 20. This program considered both radiative and conductive heat flow between the sectors.

The general equation for the temperature time derivative of a sector denoted by subscript i, subjected to the three external radiation sources and also receiving radiant and conducted heat from a section denoted by subscript j, was derived in appendix A (eq. (A7)) as

$$mc\left(\frac{dT}{d\tau}\right)_i = A_{s,i}Sa_{s,i} + A_{c,i}f(1 - \cos\,\alpha_0)Sr_e a_{s,i}\cos\,\theta_s$$

$$+ A_{c,i}f(1 - \cos\,\alpha_0)\sigma T_e^4 e_i + G_i + \sum_{j=1}^{N} h_{i-j}\left(T_j - T_i\right)$$

$$+ \sum_{j=1}^{N} R_{i-j}\left(T_j^4 - T_i^4\right) - A_{T,i}e_i\sigma T_i^4$$

An equation of this type was written for each of the sectors shown in figure 20, and all were solved simultaneously at time points during an orbital pass.

The term $1 - \cos\,\alpha_0$ is the spherical altitude correction factor where α_0 is defined as

$$\alpha_0 = \arcsin\,\frac{R_e}{R_e + \text{Altitude}}$$

18

and accounts for the variation in radiation intensity from the earth due to the angle at which the satellite "sees" the earth. Space orientation angles are shown in figure 21.

For any external sector of Explorer XIII it was necessary to determine the area A_s exposed to direct solar radiation and the area exposed to reflected solar radiation from the earth $A_c f$. Derivation of the values of the shape factor f is discussed in appendix A, and values for cones and cylinders are plotted in figures 22 and 23. The shape factors are plotted as a function of the angle η_e between the angular momentum vector and a line from the satellite to the center of the earth. Values of the ratio A_s/A_c for cones and cylinders were derived by the method of appendix A and are plotted in figures 24 and 25 for the stable and tumbling modes of rotation. These values are plotted as a function of η_s, the angle between the sun and the angular momentum vector. Throughout this paper "stable mode" refers to the condition where the satellite is rotating about the principal axis of least inertia, and "tumbling mode" refers to the condition where the satellite is rotating about the axis of maximum moment of inertia.

Since the first two terms in the generalized equation (eq. (A4)) drop out when the satellite is in the earth's shadow, it was necessary to determine the times at which the satellite entered and emerged from the shadow. The determination of these values is also discussed in appendix A.

It was necessary to tabulate the following information in order to compute a temperature time history for an orbital pass:

  (1) Solar absorptivities and total hemispherical emissivities of
       the exposed sectors

  (2) Conductive and radiative heat-transfer coefficients as shown
       in figure 20

  (3) Mass and specific heat of materials

  (4) Areas exposed to direct solar radiation and reflected earth
       radiation

  (5) Times of entry into and emergence from the earth's shadow

  (6) Orbit characteristics

     (a) Apogee altitude

     (b) Perigee altitude

(c) Orbit angle variation with time (fig. 26)

(d) Altitude variation with orbit angle (fig. 27)

(e) Angle between the sun and orbit plane, ϵ

(f) Angular distance between perigee point and closest point to the sun in the orbit plane, ζ

Several tests were made by using various subassemblies of the satellite in a vacuum to determine the magnitude of the conduction coefficients h and the radiation coefficients R to be used in this program. It was found from these tests that the telemetry temperature was strongly affected by conductive heat transfer through the bulkhead from the pressure cells and Lewis and Goddard experiments. These experimentally determined values were used in the computer program and the results indicated that for continuously repeated temperature cycles, the telemetry temperature will seek the mean temperature of the pressure cells. If the telemetry temperature was taken as the mean temperature of the surrounding shell (as is commonly assumed) an error of as much as 15° F could result for this satellite. These results serve to illustrate the importance of considering conductive heat transfer in a thermal design problem.

It is also important to note in connection with this analytical program that the calculated surface temperatures of the exposed components represent mean temperatures of the surfaces at any time, where no circumferential gradients exist. This assumption is also commonly made, but it will be shown in a later section of the paper that for the satellite in a tumbling spin considerable errors can result in some cases unless these gradients are accounted for.

Alternative method for computing telemetry temperatures.- Although the digital computer program was used in all cases to determine mean surface temperatures and their combined effect on the telemetry, the need became apparent for an alternative method by which the telemetry temperature could be quickly estimated. Such a method is developed in appendix A and is given by equation (A9) as

$$T_m^{\ 4} = \left[\frac{A_s}{A_T} p + \frac{(1 - \cos \alpha_0) r_e \cos \epsilon}{2\pi}\right]\frac{Sa_s}{\sigma e} + \left(\frac{1 - \cos \alpha_0}{2}\right)T_e^{\ 4}$$

where p is the percent time in sunlight.

Although equation (A9) is limited by the assumptions that conductivity between sectors is negligible and that the surface temperatures are uniform, it still proved to be a valuable working tool due to its relative simplicity. Since results previously discussed have established that the telemetry temperature in orbit will be essentially controlled by the mean temperature of the pressure cells, this method showed very good agreement with the more sophisticated method when applied to a large cylinder having the properties of the pressure cell sector. Agreement between values of telemetry temperature from the computer program and the alternative method for the tumbling satellite (still assuming no surface gradients) was within $\pm 5^\circ$ F in all cases examined.

Determination of maximum and minimum telemetry temperatures for tumbling mode.- By making use of the digital-computer program, it was possible to make a series of generalized calculations to predict orbiting temperature limits. In order to determine the maximum and minimum temperatures to be experienced by the telemetry with given coatings on the satellite, a family of time histories was determined for the tumbling satellite. These studies were limited to the tumbling case since it has been estimated that the stable condition (spinning about its longitudinal axis) will convert to a tumbling condition (spinning about the axis of maximum moment of inertia) in less than 2 weeks. It is therefore possible to select launch times such that both the hottest and coldest cases will occur in the tumbling mode as is discussed in the section of the paper entitled "Launch time effects."

The maximum telemetry temperature for the tumbling condition will occur when A_s/A_c is a maximum and the minimum value when A_s/A_c is a minimum. Since these values were known, the generalized cases could be evaluated for the variables ϵ (the angle between the sun and orbit plane) and ζ (the angular position of the perigee and the closest point to the sun in the orbit plane). The latter variable was selected as either 0° or 180° (perigee toward sun or away from sun, respectively) and a series of time histories were computed for various values of ϵ. The results are shown in figure 28. The hottest tumbling case occurs at $\zeta = 0^\circ$, $\epsilon = 60^\circ$ and has a value of 111° F. The coldest tumbling case is for $\zeta = 180^\circ$, $\epsilon = 0^\circ$ and the value of telemetry temperature, T_m is 34° F. Percent times in sunlight p for these two cases are 95.9 percent and 65.3 percent, respectively.

In order to establish whether the maximum and minimum percent times in sunlight had been evaluated in the generalized study, a time history of p was computed for the period of a year from a launch date of June 15 and launch hours of 0800, 1100, and 1300 E.S.T. This is shown in figure 29 where the minimum value of p is shown as 62.5 percent and the maximum value as 100 percent. The apparent differences in the values of p from the previous discussion and from figure 29 have been estimated

to reduce the minimum telemetry temperature to 30° F and raise the maximum telemetry temperature to 115° F. Figures 30 and 31 show the temperature time histories for the coldest and hottest tumbling cases discussed, respectively. This phase of the program served to establish that the coatings to be used provide a satisfactory temperature environment for the telemetry for the tumbling mode for uniformly distributed surface temperatures.

Surface temperature distributions.- After estimates were made of surface temperatures with the assumption of uniform surface distribution, the method of appendix A was used to consider nonuniform temperature distributions. Two effects of gradients are important in a thermal design problem. One is the surface temperature itself, which may be higher than that predicted over some of the surface and lower than that predicted over another part of the surface; the other is the effect of this gradient on the telemetry temperature.

Because of the low upper temperature limit of the Lewis sensors, it is the most seriously affected experiment when nonuniform surface temperatures exist. Figure 32 shows the calculated time mean surface temperature distribution on this experiment from equation (A41) for the hottest and coldest tumbling orbits already discussed. A numerical example is also given in appendix A. Only tumbling orbits need to be considered since gradients will not exist to any appreciable degree for a stabilized satellite with high rates of spin (ref. 14).

It can be seen from figure 32 that for the hottest tumbling orbit the surface temperature can be 106° F higher or 65° F lower than the value predicted when uniform temperatures are assumed. Therefore, from figures 30 and 31 the highest surface temperature on the Lewis sensors when gradients are considered may be 171° F and the coldest may be -110° F for short periods of time. It is obvious that this experiment is marginal as far as surface temperatures are concerned. This problem is further complicated by the fact that the paint on the Lewis sensors is very thin and the substrate has an a_S/e value near 3.0 as measured by two independent sources. (See appendix B.) This illustrates the need for having the highest practical upper temperature limit on experiments where surface temperatures are important.

The surface gradient effects of figure 32 for the coldest tumbling orbit are moderate, varying ±9° F on the average from the predicted value with uniform temperatures. This difference in magnitude of gradients between the hottest and coldest cases is explained by considering the satellite position with respect to the sun. For the hottest case $\eta_S = 0°$ and as the satellite tumbles, one side remains constantly sunlit; therefore, circumferential gradients are larger. In the coldest case, $\eta_S = 90°$ and all of the area is alternately lit during each tumble. Gradients are smaller in this case.

It will now be shown that if the telemetry temperature is being influenced totally or in part by conductivity, the existence of surface gradients on external parts such as shown in figures 32, 33, and 34 will influence this temperature in a manner different from that predicted for uniform surface temperatures.

As an example, consider a telemetry unit whose mean temperature is controlled by conduction from a cylinder of the type discussed in appendix A. This is a tumbling cylinder with the material properties given in the numerical example of appendix A which represents the Lewis sensors. Let the cylinder have insulated ends, nonradiating inner walls, and let the principal axis of the cylinder be at right angles to the sun. Figures 33 and 34 show the surface temperature distribution around such a cylinder of wall thickness of 0.02 inch and 0.04 inch, respectively, as determined from the linearized solution developed in appendix A. This linearized solution however has been found not to satisfy the condition of equilibrium where absorbed heat must be equal to the radiated heat. Equation (A38) of appendix A defines a constant Z as

$$Z^4 = \frac{2\pi T_m^4}{\int_0^{2\pi} T^4 d\Lambda}$$

where T_m is the mean temperature of the cylinder when uniform temperatures are assumed. Integration of the linearized solution will yield the denominator in this expression. When the constant Z is multiplied by the surface temperature values from equation (A37) the resulting curves (labeled "corrected linearized solution" in figs. 33 and 34) show excellent agreement with the numerically integrated solutions shown in these figures.

To consider gradient effects on telemetry units controlled by conduction from such a cylinder then, the surface temperature distributions are computed from equation (A37) and integrated to get a mean T^4 value. The ratio of the mean T^4 for no gradients to the mean T^4 from this equation is the constant Z^4 which corrects the telemetry temperature for gradients. For this problem, $Z = 0.954$ and $T_m = 419^\circ$ R for the uniform temperature condition. The mean temperature with gradients therefore is 399° R, indicating a decrease of 20° F in telemetry temperature if it is driven by the cylinder.

Although this example has been used for illustrative purposes, the values are not directly applicable to the Explorer XIII satellite. The

surface temperatures of figure 33 are applicable to the Lewis experiment for the conditions discussed but the telemetry of Explorer XIII is in reality rather insensitive to the Lewis sensors.

The following general comments can be made as a result of this part of the program. For a spin stabilized satellite the assumption of uniform surface temperature distribution is satisfactory. For a tumbling satellite, strong circumferential gradients can exist which are more severe for hot orbits than cold orbits. The effects of surface gradients are to produce a mean temperature which is lower than that predicted by assuming uniform temperatures; thus, a reduction in telemetry temperature is caused if it is strongly influenced by conduction.

Launch time effects.- Having established that the coatings to be used provide a satisfactory temperature environment for Explorer XIII in the tumbling mode over its lifetime in orbit, the next phase of the thermal design consisted of an evaluation of initial temperatures at injection into orbit for a particular launch date and hour. A launch date of June 15, 1961 was used for the data discussed herein.

The variation of A_s/A_c of cones and cylinders with η_s in the stable mode of rotation (figs. 24 and 25) shows that the stable values are very strongly influenced by η_s in comparison with the tumbling mode. This effect can be used to advantage in selecting a launch hour since the satellite will be stable at injection into orbit. A plot of η_s at injection for various launch times on June 15 is shown in figure 35. A value of $\eta_s = 0°$ would indicate the nose cone pointed directly at the sun, and for $\eta_s = 180°$ the nozzle is pointed directly at the sun. It can be noted that this latter condition will occur for a late evening launch.

A series of time histories for the stable satellite was computed for various launch times and the resulting telemetry temperature values are shown in figure 30. Values computed for the tumbling satellite are shown for comparison. It is apparent that late evening launches must be avoided. The two curves shown in figure 36 indicate that with the exception of launch times between 1430 and 1830 E.S.T., telemetry temperatures are within limits for the stable mode.

Because of several instrumentation requirements, the launch time for Explorer XIII could not be selected solely on the basis of telemetry temperatu-- e additional requirement was that the satellite not nercent sunlit orbit while in a spin stabilized ition can result in a battery overcharge problem. consider the look angle between the solar cells the effect of launch time on the lifetime of

L
1
7
3
7

the nickle cadmium batteries. Consideration of these four factors indicated that the launch time should be between 1000 and 1330 E.S.T. for the June 15 launch date considered. Calculations showed that between the period of June 15 to July 15, the effect of launch day on initial telemetry temperature was negligible. Figure 37 shows surface temperature time histories for the stable satellite launched at 1200 on June 15.

For the range of launch times considered it was also necessary to evaluate two effects which might be introduced by the last-stage launch vehicle velocity and flight-path angle at burnout. As pointed out in reference 10 should the flight-path angle at burnout be different from the nominal value, perigee will not occur at burnout and the apogee and perigee altitudes will change. If the injection velocity is different from the nominal, only the apogee and perigee altitudes will change. These effects were examined separately for the stable satellite to determine the changes in telemetry temperature resulting from selected error values at the launch times considered. The results are given in the following table:

Error effect	Change in initial telemetry temperature, °F
Flight-path angle in error ±1°	<+5
Perigee altitude in error ±50 nautical miles	<∓2
Apogee altitude in error ±100 nautical miles	<∓5

Although it is possible to select a launch time for which initially acceptable conditions will exist for a spinning satellite of cylindrical shape, two other factors are important if the satellite remains spin stabilized for a long period of time. First is the possibility that during the lifetime of the satellite the extremely cold case may be encountered where the minimum area may become exposed to the sun. The second is that of "wandering" of the angular momentum vector in space, as indicated by analysis of data for Explorer IV (ref. 15). The first condition might be eliminated by the use of a very highly inclined (nearly polar) orbit. But if the second condition existed as in reference 15, the spinning satellite could still have any

therefore a different mean orbit temperature. If f
long periods of time is essential, the use of ac
or attitude orientation devices appears more r

shaped satellites. However, since Explorer XIII should begin to tumble within 2 weeks after launch, estimates have established that these effects will not be serious for the launch times considered.

Materials Evaluation

In the thermal design of the Explorer XIII satellite, materials evaluation was considered as an integral part of the program. This applied not only to the flight hardware to be used but was a large part of the development of the satellite itself. Since the time available to develop Explorer XIII was relatively short, materials or coatings which had performed satisfactorily on earlier satellites were used wherever possible. A number of proof tests were conducted however on these and other materials and coatings. The results of some tests of general interest given in appendix B are

(1) Effects of long-term vacuum ultraviolet radiation

(2) Effects of high-energy proton radiation

(3) Measured solar absorptivity and total hemispherical emissivity values

Additional tests were conducted to observe

(4) Effects of temperature cycling and long-term hot and cold soaking periods in a vacuum

(5) Effects of solar radiation in a simulated space environment

Another possible environmental effect on the thermal control surfaces of a satellite is that of erosion arising mainly from micrometeoroid impact and sputtering due to collisions with neutral and charged atmospheric particles. Tests for these effects, however, were not considered mandatory for Explorer XIII for several reasons. Calculations and tests to study these erosion effects are discussed in reference 16. A study of these data indicated that Explorer XIII should not be seriously affected by these sources for a year in orbit. In addition, all the external coatings on this satellite (with the exception of the paint on the Lewis sensors) have been flight tested on earlier Explorer and Vanguard satellites and no adverse erosion effects had been noted.

discussed in appendix B consisted
m alloys. Beryllium copper,
some tests. Coatings were
ide and silicone monoxide

surface deposits. Various external treatments to the basic steel and aluminum surfaces were also examined.

Although the evaluation work done in this program was in the nature of relatively crude proof testing, some general conclusions can be made. Long-term ultraviolet radiation at one intensity in a vacuum had little effect on the basic metals tested. Optical properties of white paints were all affected to some degree and some were discarded because of extreme discoloration in less than 100 hours. Acrylic based white paints and the aluminum oxide coating showed good resistance to ultraviolet discoloration after almost 400 hours.

Proton radiation tests at 22 Mev for 5 minutes had very adverse effects on the performance of solar cells and transistors. Of the materials tested, quartz glass and silicone rubber adhesives changed color in the radiated area. Silicone rubber showed a large reduction in ultimate tensile load and elongation after exposure.

Absorptivity and total hemispherical emissivity data were determined experimentally for a number of promising spacecraft materials and coatings. These data are presented in tabular form and discussed in appendix B.

These and other materials-evaluation tests were of great value in selecting and evaluating materials and in many cases supplied information which could not be reliably obtained from other sources. From the engineering viewpoint, a satellite thermal design problem should include extensive materials evaluation experiments wherever possible to obtain the highest degree of reliability.

CONCLUDING REMARKS

The preflight study of the passive thermal design used for temperature control of the Explorer XIII (1961 Chi) satellite established the following results:

The temperatures of the exposed sensors and the telemetry units will remain within the desired limits throughout the lifetime of the satellite.

Ascent heating with the protective heat shield in place did not have a large effect on temperatures of   ell
temperatures of 113° F were indi-
reached values less than 80° r
telemetry temperature duri·

Materials tested in the programs ... mainly of steels and aluminum and magnesium ... bonding agents, and rubbers were also used in ... mainly paints of various types, and aluminum c...

the satellite. Pressure cell

...cated, and Lewis and Goddard sensors

There was no discernible rise in the

...g this phase of the flight.

Following ejection of the protective heat shield at 350,000 feet (third-stage ignition) there were no aerodynamic heating effects on the satellite.

Temperature increases in the case and nozzle of the last-stage rocket motor during burning and after burnout had a considerable effect on the sensors mounted in the area of the rocket nozzle although the temperatures of these sensors did not become excessive. A maximum surface temperature of 172° F was indicated for the Lewis sensors and 142° F for the rear row of pressure cells.

Orbit heating calculations for the spin stabilized mode indicated that extremely low telemetry-temperature values could be experienced if Explorer XIII remained spin stabilized over a long period of time. It was established however that for the short stable life of this satellite, the temperatures were tolerable for the launch times selected.

Orbit heating calculations for the tumbling mode indicated maximum and minimum telemetry temperatures of 115° F and 30° F, respectively. It was found that some of the external surfaces could be subject to extremely large temperature nonuniformities in this mode of spin resulting in hot and cold spots on the surfaces.

Thermal conductivity between various sectors of the satellite was found to have an appreciable effect on the calculated value of telemetry temperature.

The largest possible amount of materials evaluation and testing should be conducted to achieve high reliability of the surfaces and coatings to be used.

Langley Research Center,
    National Aeronautics and Space Administration,
        Langley Air Force Base, Va., January 3, 1962.

APPENDIX A

DEVELOPMENT OF EQUATIONS

General Heat-Flux Equation

To begin the development of the general heat-flux equation, consider the radiant heat exchange between two bodies separated by a distance so great that reflections between their surfaces may be neglected
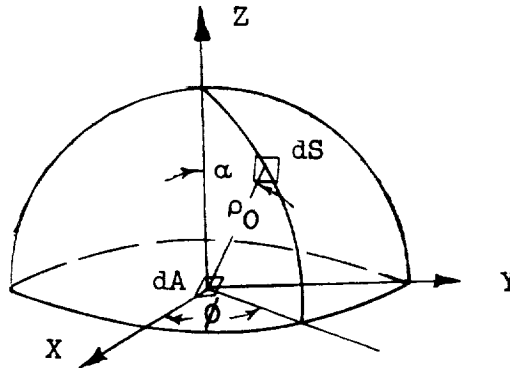
In this sketch let the element dA emit radiant heat with intensity $J(0,0)$, the heat flux from dA is $J(0,0)dA$. If this radiation is perfectly diffuse, it is possible to define the heat-flux distribution on the hemisphere of radius ρ. The intensity is proportional to the cosine of α, so the flux distribution at (α,ρ_0) must be $J(0,\rho_0) \cos \alpha$, where $J(0,\rho_0)$ is found by integrating the heat flux over the hemispherical surface and equating it to $J(0,0)dA$

$$J(0,0)dA = \oiint_S J(0,\rho_0) \cos \alpha \, dS$$

where

$$dS = \rho_0^2 \sin \alpha \, d\alpha \, d\phi$$

$$J(0,0)dA = J(0,\rho) \int_0^{2\pi} \int_0^{\pi/2} \left(\rho_0^2 \cos \alpha\right) \sin \alpha \, d\alpha \, d\phi$$

$$J(0,0)dA = \rho_0^2 \, \pi J(0,\rho) \left[\sin^2 \alpha\right]_0^{\pi/2} = \pi J(0,\rho)\rho_0^2$$

$$J(0,\rho) = \frac{J(0,0)dA}{\pi\rho_0^2}$$

<div align="right">(A1)</div>

From equation (A1) the heat-flux distribution on the hemisphere becomes

$$J(\rho_0,\alpha) = \frac{J(0,0)\cos\alpha\ dA}{\pi\rho_0^2}$$

If a body has area A_P projected on this hemisphere the elemental heat flux received by the body from dA is

$$d\Phi = J(\alpha,\rho_0)A_P = \left[\frac{J(0,0)A_P}{\pi}\right]\left(\frac{\cos\alpha\ dA}{\rho_0^2}\right)$$

If a spherical coordinate system is centered at the body as indicated in the following sketch
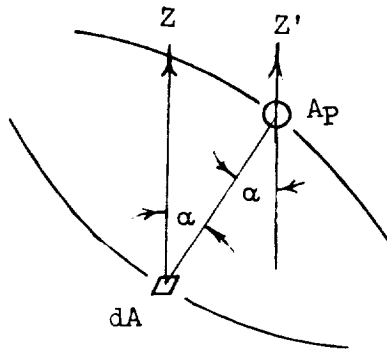
$\dfrac{\cos\alpha\ dA}{\rho_0^2}$ becomes $\sin\alpha\ d\alpha\ d\phi$ then

$$d\Phi = \frac{J(\alpha,\phi)A_P}{\pi}\sin\alpha\ d\alpha\ d\phi$$

<div align="right">(A2)</div>

and

$$\Phi = \frac{1}{\pi}\int_0^{2\pi}\int_0^{\alpha_0} J(\alpha,\phi)A_P(\alpha,\phi)\sin\alpha\ d\alpha\ d\phi$$

<div align="right">(A3)</div>

To illustrate equation (A3), the heat flux on a spherical satellite from the earth thermal radiation is calculated. Assume that

$$J(\alpha, \phi) = \sigma T_e^4$$

$$A_p(\alpha, \phi) = A_c$$

then

$$\Phi_e = 2 \int_0^{\alpha_0} \sigma T_e^4 A_c \sin \alpha \, d\alpha$$

$$= -2\sigma T_e^4 A_c \left[\cos \alpha\right]_0^{\alpha_0}$$

$$= 2A_c \sigma T_e^4 (1 - \cos \alpha_0) = \frac{A_T}{2} \sigma T_e^4 (1 - \cos \alpha_0)$$

The factor $1 - \cos \alpha_0$ is called the spherical satellite altitude correction factor. In a similar manner it is possible to calculate the heat received from all the sources acting on a satellite. The two sources giving external heat to the satellite are the earth and sun. From the sun comes direct solar radiation and the solar heat reflected by the earth onto the satellite; also, there is direct radiant energy from the earth. If a satellite is influenced by these sources only, the total heat flux may be written as

$$mc\left(\frac{dT}{d\tau}\right) = \Phi_s a_s + \Phi_{rs} a_{rs} + \Phi_e a_e - A_T e \sigma T^4 \qquad (A4)$$

Throughout this paper it is assumed that $a_e = e$ and $a_{rs} = a_s$.

Equation (A3) may be used to calculate the heat flux from each source. To calculate the heat flux on Explorer XIII, the heat-flux integrals were simplified enough so that closed solutions could be found in the tumbling mode and were integrated numerically in the stable mode. The long time phase of Explorer XIII is with the principal axis at a right angle to the angular momentum vector. In this mode the area A_p was taken as the time average area projected to a viewer for a given angle between the momentum vector and the viewer η_e. The area variation was represented by

$$A_p(\eta) = \sum_{K=0}^{K=N} i_k \cos K\eta$$

where the values of i_k were determined by the theory of Fourier series. In all cases the error in $A_P(\eta)$ introduced by this approximation was less than 3 percent. If $J(\alpha, \phi)$ is constant, Φ_e is obtainable in closed form. The flux Φ_e was calculated by

$$\Phi_e = J(0,0)A_c(1 - \cos \alpha_0)f_e(\eta_e)$$

where

$$f_e(\eta_e) = \frac{1 \displaystyle\int_0^{2\pi} \int_0^{\alpha_0} A_P(\alpha, \phi)\sin \alpha \, d\alpha \, d\phi}{A_c\pi(1 - \cos \alpha_0)}$$

The general heat-flux equation can now be developed. The reflected solar heat flux is approximately

$$\Phi_{rs} \approx A_c J(0,0)f_{rs}(1 - \cos \alpha_0)\cos \theta_s \tag{A6}$$

where

$$f_{rs} \approx f_e$$

The errors introduced by this convention are of minor importance for a tumbling satellite and are discussed in reference 10. The direct solar heat flux Φ_s is merely

$$\Phi_s = SA_s$$

where A_s is the area projected to the sun. Now assuming uniform temperatures on the different external components the heat radiated away by the body is

$$A_T e \sigma T^4$$

The assumption of uniform temperatures will introduce an error because usually large circumferential gradients will exist (and possibly longitudinal gradients if two thermally linked components have different mean temperatures). These effects will be discussed later in this appendix; however, for the sake of developing the heat-flux equation, uniform surface temperatures are assumed, and the subscripts i and j denote two sectors with heat flow between them. For sector i, the general equation may be written as

$$mc\left(\frac{dT}{d\tau}\right)_i = A_{s,i}Sa_{s,i} + A_{c,i}f(1 - \cos \alpha_0)Sr_e a_{s,i} \cos \theta_s$$

$$+ A_{c,i}f(1 - \cos \alpha_0)\sigma T_e^4 e_i + G_i + \sum_{j=1}^{N} h_{i-j}(T_j - T_i)$$

$$+ \sum_{j=1}^{N} R_{i-j}\left(T_j^4 - T_i^4\right) - A_{T,i}e\sigma T_i^4 \tag{A7}$$

where

G_i internal heat generated

h conduction coefficient

R radiation coefficient

Equation (A7) is the most general equation for the heat flux on a satellite's components and is different from equation (A4) since it considers all possible heat transfer between components.

Shape Factors

In order to calculate shape factors for equation (A7) it was necessary to first determine the area distribution for the satellite sectors for both stable and tumbling spin modes. To illustrate this, the area distribution for a cone will be calculated with the symbol notation shown in the following sketch:
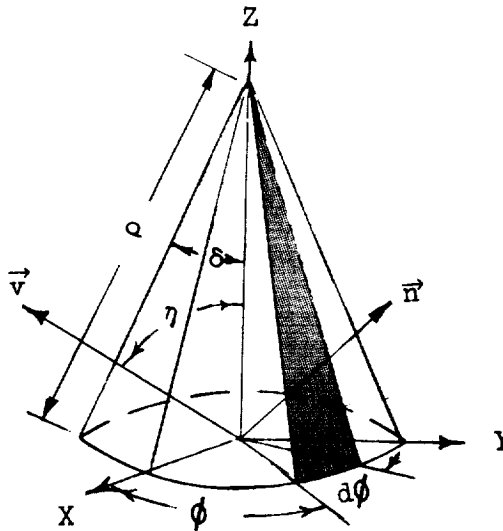
From this sketch, the area of the small shaded triangle is

$$dA = \frac{\rho^2}{2} \sin \delta \, d\phi$$

let

$$\overrightarrow{dA} = \vec{n}(dA)$$

To the viewer $\vec{v}$ the projected elemental area is $\vec{v} \cdot \overrightarrow{dA}$ where the limits of integration are fixed by

$$\vec{v} \cdot \overrightarrow{dA} = 0$$

Also from the sketch

$$\vec{n} = i(\cos \delta \cos \phi) + j(\cos \delta \sin \phi) + k(\sin \delta)$$

$$\vec{v} = i(\sin \eta) + j(\cos \eta)$$

Then $\vec{v} \cdot \vec{n} = (\sin \eta \cos \delta \cos \phi) + (\sin \delta \cos \eta)$

$$A_P = 2 \int_0^{\cos^{-1}\phi_1} \left(\sin \eta \cos \delta \cos \phi + \sin \delta \cos \eta\right)\frac{\rho^2}{2} \sin \delta \, d\phi$$

and the integration limits are fixed by

$$\cos \phi_1 = -\tan \delta \cot \eta$$

The resulting expression is

$$A_P(\eta) = \rho^2 \left[(\sin \eta \cos \delta)\sin \phi + (\sin \delta \cos \eta)\phi\right]_0^{\phi_1} \sin \delta$$

with the convention that

$$\cos \phi_1 = -\tan \delta \cot \eta \qquad \left((\tan \delta \cot \eta) < 1\right)$$

$$\phi_1 = \pi \qquad (-\tan \delta \cot \eta < -1)$$

$$\phi_1 = 0 \qquad (-\tan \delta \cot \eta > 1)$$

This is the area for a cone for view angles η if the cone is spinning about its principal axis. For the cone in a tumbling spin (i.e., with

the momentum vector at right angles to the principal axis)
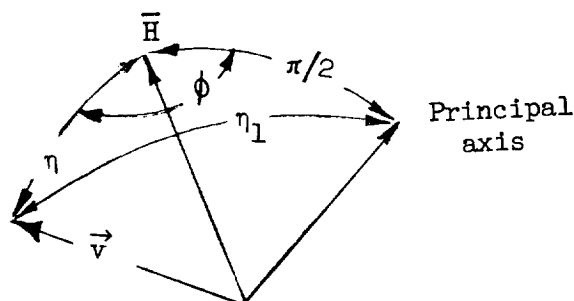
$$Ap(\eta)_{tumbling} = \frac{1}{2\pi} \oint_0^{2\pi} {}^{A}P(\eta_1)_{stable} \, d\phi$$

where $\cos \eta_1 = \sin \eta \cos \phi$ and η_1 is a dummy variable. This integral is easily evaluated numerically and the results may be fitted to

$$\frac{A_P}{A_c}(\eta) = \sum_{K=0}^{\infty} i_K \cos K\eta$$

where K is an even integer because $\frac{A_P}{A_c}(\eta)$ has double symmetry and can be truncated with a high degree of accuracy for $K > 4$. With trigonometric identities this series can be changed to the form

$$\frac{A_P}{A_c}(\eta)_{tumbling} = \sum_{K=0}^{\infty} I_K \cos^K \eta$$

but

$$(\cos \eta)^K = (\cos \eta_e \cos \alpha + \sin \eta_e \sin \alpha \cos \phi)^K$$

so that equation (A3) can be integrated analytically to find the required shape factors. Let $\frac{A_P}{A_c}(\eta)$ be expressed by

$$\frac{A_P}{A_c}(\eta) \approx i_0 + i_2 \cos 2\eta + i_4 \cos 4\eta$$

This expression can be represented by

$$\frac{A_P}{A_c}(\eta) \approx I_0 + I_2 \cos^2\eta + I_4 \cos^4\eta$$

where

$$I_0 = (i_0 - i_2 + i_4)$$

$$I_2 = (2i_2 - 8i_4)$$

$$I_4 = 8i_4$$

after substituting for $\cos \eta$

$$\cos \eta = \cos \eta_e \cos \alpha + \sin \eta_e \sin \alpha \cos \phi$$

The results are substituted into equation (A3) and the resulting shape factor is

$$(1 - \cos \alpha_0)f(\eta_e, \alpha_0) \approx 2I_0(1 - \cos \alpha_0) + \frac{2I_2}{3} \cos^2\eta_e\left(1 - \cos^3\alpha_0\right)$$

$$+ \frac{I_2}{3} \sin^2\eta_e\left[2 - \cos \alpha_0\left(\sin^2\alpha_0 + 2\right)\right] + \frac{2I_4}{5} \cos^4\eta_e\left(1 - \cos^5\alpha_0\right)$$

$$+ \frac{I_4}{20} \sin^4\eta_e\left[8 - 3 \sin^4\alpha_0 \cos \alpha_0 - 4 \cos \alpha_0\left(\sin^2\alpha_0 + 2\right)\right]$$

$$+ \frac{6}{5} I_4 \cos^2\eta_e \sin^2\eta_e\left[\frac{2}{3} - \cos^3\alpha_0\left(\sin^2\alpha_0 + \frac{2}{3}\right)\right]$$

This equation gives the shape factor for earth thermal radiation for any body whose area distribution is expressed with sufficient accuracy by the equation

$$\frac{A_P}{A_c}(\eta) \approx i_0 + i_2 \cos 2\eta + i_4 \cos 4\eta$$

Values of $f(\eta)$ are plotted in figure 22 for a 45° cone at an altitude of 400 nautical miles. Calculated area distributions for a 45° cone for both the stable and tumbling conditions are shown in figure 24.

Alternative Method for Mean Orbit Temperatures

In order to determine a check for possible errors in the general
method, an alternative method was developed, by which the mean tempera-
ture T_m of any sector during an orbit pass could be obtained for the
tumbling satellite by a relatively simple analysis independent of the
IBM 7090 program and is based on the heat transfer between an infinite
flat plate and the satellite.

First it is necessary to find a unit heat-flux distribution as a
function of η_e. Consider the following sketch, where the plate's normal
represents the satellite surface and dS is an element on the earth's
surface.
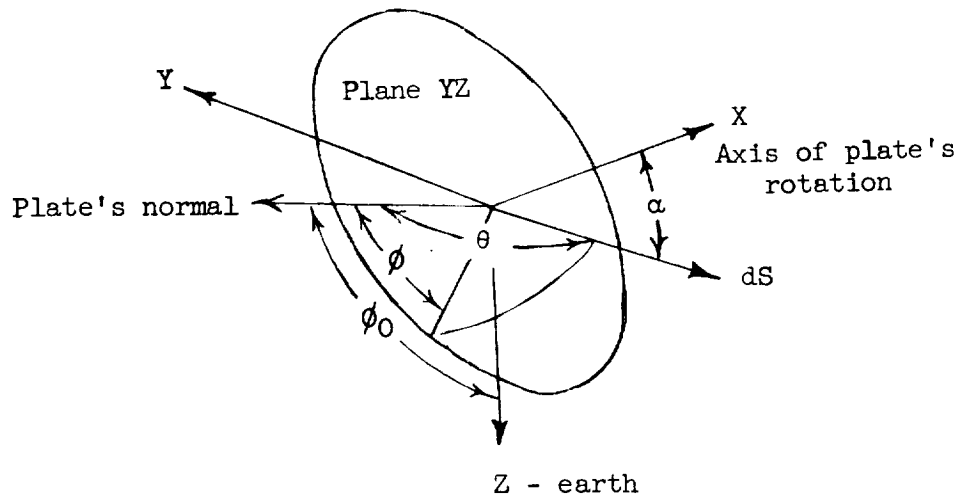
Z - earth

Equation (A2) can be expressed as

$$dJ(\phi,\alpha) = \frac{J(0,0)}{\pi} \cos\theta \sin\alpha \, d\alpha \, d\phi$$

and where $\cos\theta = \sin\alpha \cos\phi$ then

$$J(\phi_0) = \frac{J(0,0)}{\pi} \int_{-\frac{\pi}{2}}^{\frac{\pi}{2}-\phi_0} \int_0^\pi \sin^2\alpha \cos\phi \, d\alpha \, d\phi = \frac{J(0,0)}{2}(1 + \cos\phi_0)$$

Now let $\phi_0 = \eta_e$ so that

$$J(\tau_{le}) = \frac{J(0,0)}{2}(1 + \cos \tau_{le}) \qquad (A8)$$

By integration over the surface of a sphere

$$\Phi_e = \frac{A_T}{2} J(0,0)$$

The exact expression for a sphere and a round earth is

$$\Phi_e = \frac{A_T}{2} J(0,0)(1 - \cos \alpha_0)$$

Further integration shows that, for a tumbling cone or cylinder with their axis of symmetry perpendicular with the axis of rotation,

$$\Phi_e = \frac{A_T}{2} J(0,0)$$

When the altitude correction factor is applied for any nonconcave surface satellite $\Phi_e = \frac{A_T}{2} J(0,0)(1 - \cos \alpha_0)$. Numerical checks have shown this expression to be in close agreement with the more sophisticated method. Following the convention previously developed that

$$f_{rs} = f_e$$

the total heat-flux equation can be expressed as

$$mc \frac{dT}{d\tau} = A_s S a_s + \frac{A_T}{2}(1 - \cos \alpha_0)\cos \theta_s S r_e a_s + \frac{A_T}{2}(1 - \cos \alpha_0)e\sigma T_e^4 - A_T e\sigma T^4$$

Let $\cos \theta_s = \cos \epsilon \cos \delta$ and let the temperature time history of the satellite be repeated over each orbit, then

$$\int_0^P \frac{dT}{d\tau} = 0$$

Also assume that the orbit is circular and integrate $\frac{dT}{d\tau}$ through one orbit period P to obtain

$$\Omega A_S Sa_S + A_T(1 - \cos \alpha_0)\cos \epsilon Sr_e a_S + \pi A_T(1 - \cos \alpha_0)e\sigma T_e{}^4 - 2\pi A_T e\sigma T_m{}^4 = 0$$

Division by 2π gives

$$A_T e\sigma T_m{}^4 = \left[A_S \frac{\Omega}{2\pi} + \frac{A_T}{2\pi}(1 - \cos \alpha_0)\cos \epsilon r_e \right] Sa_S + \frac{A_T}{2}(1 - \cos \alpha_0)e\sigma T_e{}^4$$

or

$$T_m{}^4 = \left[\frac{A_S}{A_T} p + \frac{(1 - \cos \alpha_0)r_e \cos \epsilon}{2\pi} \right] \frac{Sa_S}{\sigma e} + \left(\frac{1 - \cos \alpha_0}{2} \right) T_e{}^4 \qquad (A9)$$

for any sector with uniform surface temperatures. In equation (A9), p is percent time in sunlight and ϵ is the angle between the orbit plane and a vector from the center of the earth pointing to the sun. A term by term check of this equation shows that the first term is exact, the second term contains errors already discussed, and the last term has about 3-percent error if the orbit is circular, and the satellite is tumbling.

Percent Time in Sunlight

In order to calculate any orbit temperature time history it is necessary to know the times in and out of the earth's shadow (or percent time in sunlight). A method of determining these values for an eccentric orbit is now developed. The equations for percent time in sunlight are based on a right-hand, orthogonal, nonrotating coordinate system with the z-axis alined with the earth's axis of rotation (North Pole), and the y-axis perpendicular to a line in space connecting the centers of the earth and sun at the summer solstice as shown in the following sketch:
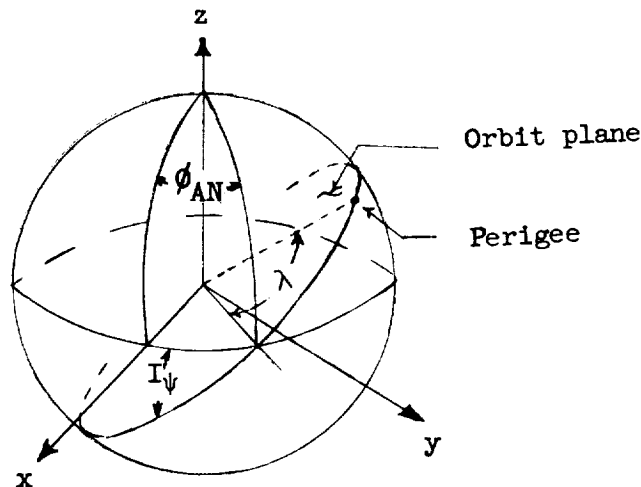
where

ϕ_{AN} angle (measured in plane of equator) between x-axis and orbit ascending node

λ angle (measured in plane of orbit) between ascending node and orbit perigee

I   orbit inclination relative to equatorial plane

Let the x',y',z' axis system lie with the z'-axis perpendicular to the orbit plane and the x'-axis passing through orbit perigee. To express the satellite's position relative to the x,y,z system use the following matrix transformations:

$$\begin{Bmatrix} x' \\ y' \\ z' \end{Bmatrix} = T(\lambda)T(I)T(\phi_{AN}) \begin{Bmatrix} x \\ y \\ z \end{Bmatrix}$$

where

$$T(\phi_{AN}) = \begin{bmatrix} \cos\phi_{AN} & \sin\phi_{AN} & 0 \\ -\sin\phi_{AN} & \cos\phi_{AN} & 0 \\ 0 & 0 & 1 \end{bmatrix}$$

$$T(I) = \begin{bmatrix} 1 & 0 & 0 \\ 0 & \cos I & \sin I \\ 0 & -\sin I & \cos I \end{bmatrix}$$

$$T(\lambda) = \begin{bmatrix} \cos\lambda & \sin\lambda & 0 \\ -\sin\lambda & \cos\lambda & 0 \\ 0 & 0 & 1 \end{bmatrix}$$

so that

$$
\begin{Bmatrix} x' \\ y' \\ z' \end{Bmatrix} = \begin{bmatrix} \left(\cos \lambda \cos \phi_{AN} - \sin \lambda \cos I \sin \phi_{AN}\right) & \left(\cos \lambda \sin \phi_{AN} + \sin \lambda \cos I \cos \phi_{AN}\right) & \left(\sin \lambda \sin I\right) \\ \left(-\sin \lambda \cos \phi_{AN} - \cos \lambda \cos I \sin \phi_{AN}\right) & \left(-\sin \lambda \sin \phi_{AN} + \cos \lambda \cos I \cos \phi_{AN}\right) & \left(\cos \lambda \sin I\right) \\ \left(\sin I \sin \phi_{AN}\right) & \left(-\sin I \cos \phi_{AN}\right) & \left(\cos I\right) \end{bmatrix} \begin{Bmatrix} x \\ y \\ z \end{Bmatrix}
$$

where $\begin{bmatrix}\ \end{bmatrix}$ denotes square matrix and $\begin{Bmatrix}\ \end{Bmatrix}$ denotes column matrix. The x'-axis may be made to coincide with the satellite by adding the orbit angle δ to λ since x' and y' lie in the orbit plane. Then the satellite unit vector position is

$$
x' = x\left[\cos(\lambda + \delta)\cos \phi_{AN} - \sin(\lambda + \delta)\cos I \sin \phi_{AN}\right] + y\left[\cos(\lambda + \delta)\sin \phi_{AN} \right.
$$

$$
\left. + \sin(\lambda + \delta)\cos I \cos \phi_{AN}\right] + z\left[\sin(\lambda + \delta)\sin I\right]
$$

Next take an axis system (x", y", z") which lies in the ecliptic plane and let x" point toward the sun as shown in the following sketch:
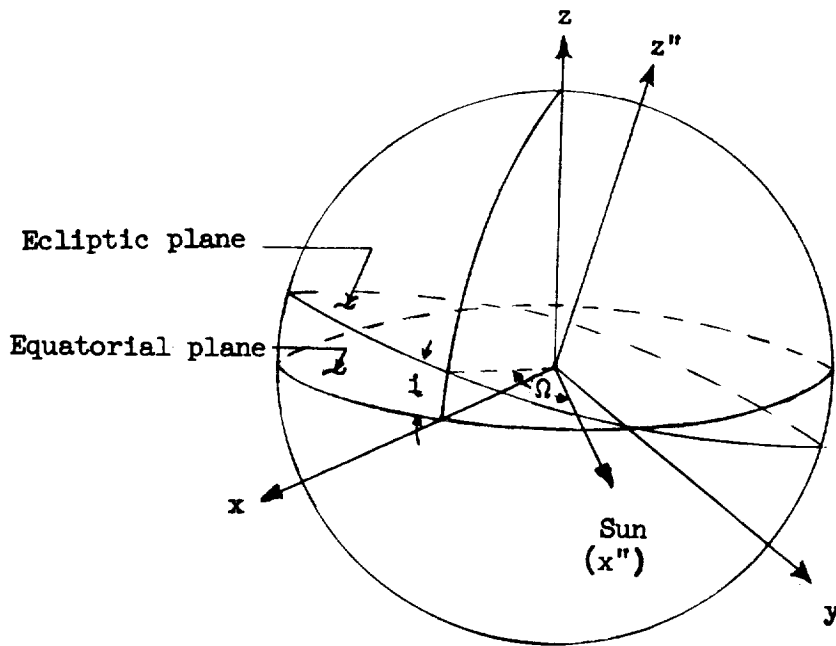
so that

$$\begin{Bmatrix} x'' \\ y'' \\ z'' \end{Bmatrix} = T(\Omega)T(i) \begin{Bmatrix} x \\ y \\ z \end{Bmatrix}$$

where

$$T(i) = \begin{bmatrix} \cos i & 0 & \sin i \\ 0 & 1 & 0 \\ -\sin i & 0 & \cos i \end{bmatrix}$$

$$T(\Omega) = \begin{bmatrix} \cos \Omega & \sin \Omega & 0 \\ -\sin \Omega & \cos \Omega & 0 \\ 0 & 0 & 1 \end{bmatrix}$$

Therefore,

$$\begin{Bmatrix} x'' \\ y'' \\ z'' \end{Bmatrix} = \begin{bmatrix} \cos \Omega \cos i & \sin \Omega & \cos \Omega \sin i \\ -\sin \Omega \cos i & \cos \Omega & -\sin \Omega \sin i \\ -\sin i & 0 & \cos i \end{bmatrix} \begin{Bmatrix} x \\ y \\ z \end{Bmatrix}$$

and

$$x'' = (\cos \Omega \cos i)x + y(\sin \Omega) + z(\cos \Omega \sin i)$$

Because x'' is the sun's unit vector position,

$$\cos \theta_S = x' \cdot x'' \tag{A10}$$

42

$$\cos \theta_s = \Big(\cos \Omega \cos i \cos \phi_{AN} + \sin \Omega \sin \phi_{AN}\Big)\cos(\lambda + \delta)$$

$$+ \Big(\cos \Omega \sin i \sin I + \sin \Omega \cos I \cos \phi_{AN}$$

$$- \cos \Omega \cos i \cos I \sin \phi_{AN}\Big)\sin(\lambda + \delta)$$

and if A equals the first term in parentheses and B equals the third term in parentheses, this equation becomes

$$\cos \theta_s = A \cos(\lambda + \delta) + B \sin(\lambda + \delta)$$

$$= (A \cos \lambda + B \sin \lambda)\cos \delta + (B \cos \lambda - A \sin \lambda)\sin \delta$$

But this form is equivalent to

$$\cos \theta_s = \cos \epsilon \cos(\delta - \zeta) = \cos \epsilon \cos \zeta \cos \delta + \cos \epsilon \sin \zeta \sin \delta \qquad (A11)$$

so that

$$\cos \epsilon = \sqrt{A^2 + B^2}$$

$$\cos \zeta = \frac{A \cos \lambda + B \sin \lambda}{\cos \epsilon}$$

$$\sin \zeta = \frac{B \cos \lambda - A \sin \lambda}{\cos \epsilon}$$

The terms ϕ_{AN}, λ, and Ω are expressible in the form

$$\phi_{AN} = \phi_0 + \dot{\phi}D$$

$$\lambda = \lambda_0 + \dot{\lambda}D$$

$$\Omega = \Omega_0 + \Delta\Omega$$

where ϕ_0, λ_0, and Ω_0 are initial values which may be determined graphically from the orbit plotted on a round globe and dots denote differentiation with respect to time. The terms $\dot{\phi}$ and $\dot{\lambda}$ are produced by an oblate earth and may be determined from reference 17, and D is

the time elapsed in days since the launch date. The term $\Delta\Omega$ is the sun's movement relative to the earth in the ecliptic plane since the launch day.
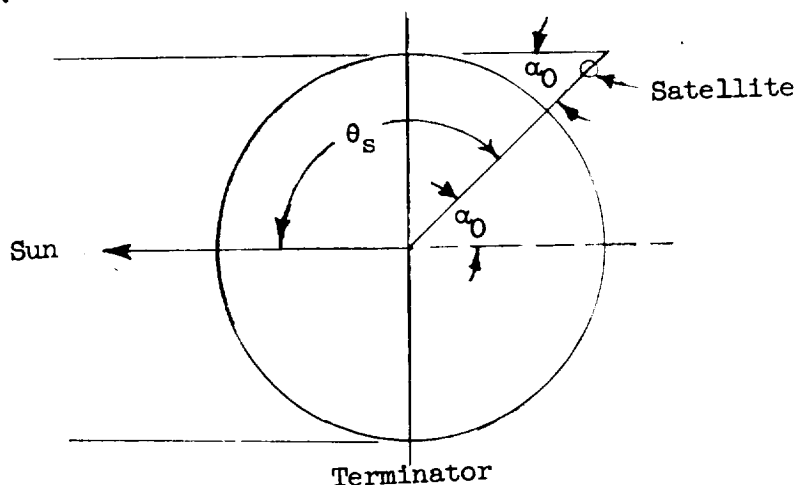
If the earth's shadow is assumed to be cylindrical, the satellite enters or leaves the earth's shadow when

$$\alpha_0 = \pi - \theta_s \qquad \left(0 \leqq \theta_s \leqq \pi\right)$$

$$\alpha_0 = \theta_s - \pi \qquad \left(\pi \leqq \theta_s \leqq 2\pi\right)$$

Actual intersections occur only when

$$\frac{\pi}{2} \leqq \theta_s \leqq \frac{3\pi}{2}$$

so that extraneous intersections may be excluded by comparing cosines. Therefore, an intersection occurs only when

$$\cos \alpha_0 = -\cos \theta_s$$

To solve this equation, first make a family of plots for $-\cos \theta_s$ as a function of δ_1 with

$$\epsilon = 0^\circ, \; 5^\circ, \; 10^\circ, \; 15^\circ, \; \ldots \; 90^\circ$$

and δ_1 is a dummy variable; also make a transparent plot of $\cos \alpha_0$ as a function of δ. To aline these two plots notice that $\cos \theta_s$ is 0 and increasing negatively at

$$(\delta - \zeta) = \frac{\pi}{2}$$

44

or

$$\delta = \frac{\pi}{2} + \zeta$$

so that the two graphs are correctly alined when the point

$$\delta_1 = \frac{\pi}{2}$$

from the $(-\cos \theta_S)$ plot coincides with $\delta = \frac{\pi}{2} + \zeta$ on the following $\cos \alpha_0$ plot:

δ, radians
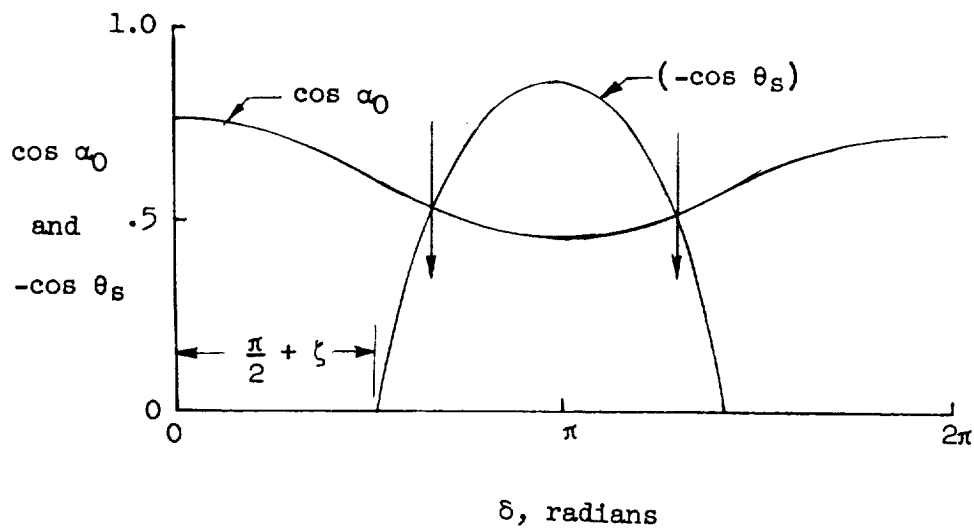
The sunlight intersections are shown by the two arrows, and the satellite is in the earth's shadow when

$$-\cos \theta_S > \cos \alpha_0$$

These intersections may be converted to time from a plot of time against orbit angle.

Surface Temperature Distributions

The method developed in this section is concerned with surface temperature distributions due to a combination of two effects; the circumferential distribution on a cylinder wall from nonuniform illumination and the position of the satellite in orbit with respect to the heating sources. The effect of surface distribution on the telemetry temperature will also be developed.

To arrive at expressions for circumferential gradients, begin by considering a thin-wall cylinder exposed to direct solar, earth thermal, and reflected solar radiation. Let the cylinder's ends be insulated, also let there be no heat transferred by radiation on the cylinder's inner walls. The cylinder is assumed to be in a circular orbit and in a tumbling mode such that its principal axis is at a right angle to its angular momentum vector as shown in the following sketch:
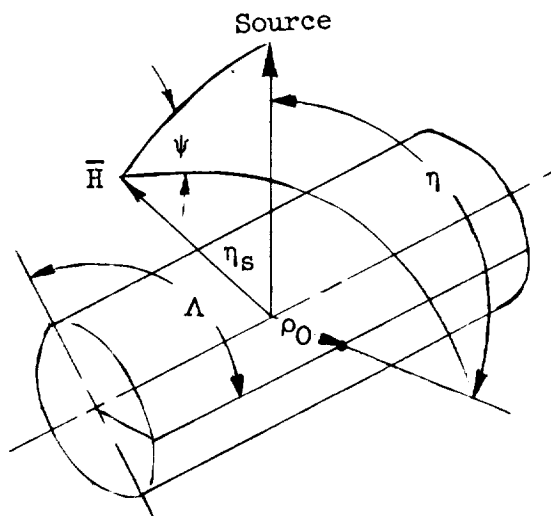
The direct solar heat flux per unit area on the cylinder's wall is $S \cos \eta$. By the law of cosines from spherical trigonometry

$$\cos \eta = \cos \eta_s \cos \Lambda + \sin \eta_s \sin \Lambda \cos \psi \qquad (A12)$$

If the cylinder is spinning fast enough so that the temperature fluctuations over one cycle are small, the incident heat flux per unit area on each point of the cylinder may be taken as the average during one cycle. The direct solar heat incident on the cylinder surface is

$$HS \overline{\cos \eta}$$

where H has a value of unity when the satellite is in sunlight and zero in the earth's shadow. The term $\overline{\cos \eta}$ is defined by

$$\frac{1}{\pi} \int_0^{\pi} \cos^* \eta \; d\psi$$

where * denotes that all negative values of $\cos \eta$ are taken as zero. Because of the symmetry of $\cos \eta$ with respect to η_s,

$$0 \leqq \eta_s \leqq \frac{\pi}{2}$$

$$0 \leqq \Lambda \leqq \pi$$

with this convention $\cos \eta$ is negative for

$$\cos^{-1}\left(-\cot \eta_s \cot \Lambda\right) \leqq \psi \leqq \pi$$

so that

$$\overline{\cos \eta} = \frac{1}{\pi}\left[\left(\cos \eta_s \cos \Lambda\right)\psi + \left(\sin \eta_s \sin \Lambda\right)\sin \psi\right] \qquad (A13)$$

where ψ is defined by

$$\cos \psi = -\cot \eta_s \cot \Lambda$$

The two cases of interest in this paper are

$$\eta_s = 0$$

$$\eta_s = \frac{\pi}{2}$$

if $\eta_s = 0$, then

$$\overline{\cos \eta_s} = \cos{}^*\Lambda \tag{A14}$$

and if $\eta_s = \dfrac{\pi}{2}$, then

$$\overline{\cos \eta_s} = \frac{1}{\pi}\left|\sin \Lambda\right| \tag{A15}$$

From equation (A8) the earth thermal and reflected solar radiation for low orbits is approximately

$$\frac{J(0,0)}{2}\left(1 + \cos \eta_e\right)$$

Because this expression is nonnegative, the negative values of $\cos \eta_e$ may be included in the integration and

$$\overline{\cos \eta_e} = \frac{1}{\pi}\left(\cos \eta_e \cos \Lambda\right)\pi$$

$$= \cos \eta_e \cos \Lambda \tag{A16}$$

the expressions relating η_s, η_e, and θ_s are found by vectors
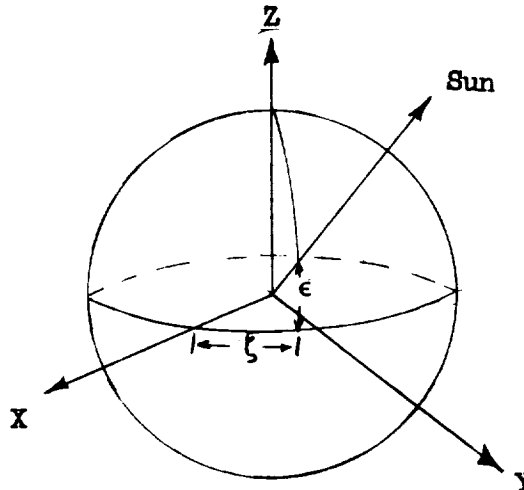
Let the XY-plane be the orbit plane with the X-axis passing through the perigee and γ_0 be the angle between the satellite angular momentum vector projection onto the orbit plane and the local horizon at the orbit perigee, with ν being the angle between the orbit plane and the angular momentum vector. Let $\vec{R}_u$ be an arbitrary unit vector originating at the earth's center, then

$$\vec{R}_{u,1} = \left(\vec{R}_u\right)_{sun} = (\cos \epsilon \cos \zeta)i + (\cos \epsilon \sin \zeta)j + (\sin \epsilon)k$$

$$\vec{R}_{u,2} = \left(\vec{R}_u\right)_{satellite} = (\cos \delta)i + (\sin \delta)j$$

$$\vec{R}_{u,3} = \left(\vec{R}_u\right)_{momentum\ vector} = (\cos \nu \sin \gamma_0)i + (\cos \nu \cos \gamma_0)j + (\sin \nu)k$$

Therefore, the following quantities may be written:

$$\cos \eta_e = -\vec{R}_{u,3} \cdot \vec{R}_{u,2} = -\cos \nu \sin\left(\gamma_0 + \delta\right) \tag{A17}$$

$$\cos \eta_s = \vec{R}_{u,1} \cdot \vec{R}_{u,3}$$
$$= \cos \nu \sin \gamma_0 \cos \epsilon \cos \zeta + \cos \nu \cos \gamma_0 \cos \epsilon \sin \zeta + \sin \nu \sin \epsilon$$
$$= \cos \nu \cos \epsilon \sin\left(\gamma_0 + \zeta\right) + \sin \nu \sin \epsilon$$

$$\cos \theta_s = \vec{R}_{u,1} \cdot \vec{R}_{u,2} = \cos \epsilon \cos(\delta - \zeta) \tag{A18}$$

The term $J(0,h)$ has been defined as the radiant heat intensity per unit area received by a plate, at a distance h from the earth's surface, and whose normal passes through the earth's center. The flux per unit area leaving the earth's surface is approximately

$$\sigma T_e^4 + r_e S \cos \theta_s = \sigma T_e^4 + r_e S \cos \epsilon \cos^*(\delta - \zeta)$$

and is multiplied by the correction factor

$$2 \sin^2 \frac{\alpha_0}{2} = (1 - \cos \alpha_0)$$

Therefore $J(0,h)$ is approximately $2 \sin^2 \frac{\alpha_0}{2} \, e\sigma T_e^4 \left(1 + \frac{a_s r_e S}{e\sigma T_e^4} \cos \epsilon \, \cos^* \xi\right)$

where $\xi \approx \delta - \zeta$ for near circular orbits. The solution may be simplified by writing

$$1 + \left(\frac{a_s r_e S}{e\sigma T_e^4}\right) \cos \epsilon \, \cos^* \xi = \sum_K b_K \cos K\xi$$

If

$$g = \frac{a_s r_e S}{e\sigma T_e^4} \cos \epsilon$$

then

$$b_0 = 1 + \frac{g}{\pi}$$

$$b_1 = \frac{g}{2}$$

$$b_K = \frac{2g}{\pi}(-1)^{K/2}\left[\frac{1}{1 - K^2}\right] \quad \text{for even values of } K$$

$$b_K = 0 \quad \text{for odd values of } K, \text{ if } K > 2$$

the term $\overline{\cos \eta_e}$ may be written as

$$\overline{\cos \eta_e} = -\cos \nu \, \sin\left(\gamma_0 + \delta\right)\cos \Lambda$$

since

$$\xi \approx \delta - \zeta$$

then

$$\gamma_0 + \delta \approx \left(\gamma_0 + \zeta\right) + \xi$$

so that the earth's contribution to the cylinder's heating is approximately

$$\sin^2\left(\frac{\alpha_0}{2}\right)e\sigma T_e^4 \left\{1 - \cos \nu \cos \Lambda \sin\left[\left(\gamma_0 + \zeta\right) + \xi\right]\right\} b_0$$

$$+ \sin^2\left(\frac{\alpha_0}{2}\right)e\sigma T_e^4 \left\{1 - \cos \nu \cos \Lambda \sin\left[\left(\gamma_0 + \zeta\right) + \xi\right]\right\} \sum_{K=1}^{\infty} b_K \cos K\xi$$

$$= \frac{J(0,h)}{2}\left(1 + \overline{\cos \eta_e}\right)$$

By trigonometric manipulation the earth's contribution becomes

$$\sin^2\left(\frac{\alpha_0}{2}\right)e\sigma T_e^4 b_0 - \sin^2\left(\frac{\alpha_0}{2}\right)e\sigma T_e^4\cos \nu \cos \Lambda \sin\left[\left(\gamma_0 + \zeta\right) + \xi\right] b_0$$

$$+ \sin^2\left(\frac{\alpha_0}{2}\right)e\sigma T_e^4 \sum_{K=1}^{\infty} b_K \cos K\xi - \frac{\sin^2\left(\frac{\alpha_0}{2}\right)}{2}e\sigma T_e^4\cos \nu \cos \Lambda \sum_{K=1}^{\infty} b_K \left\{\sin\left[\left(\gamma_0\right.\right.\right.$$

$$\left.\left.+ \zeta\right) + (1 + K)\xi\right] + \sin\left[\left(\gamma_0 + \zeta\right) + (1 - K)\xi\right]\bigg\} \tag{A19}$$

To complete the direct solar heating assume

$$\overline{\cos \eta_s} = \sum_{K} a_K \cos K\Lambda \tag{A20}$$

Now let $\eta_s = \dfrac{\pi}{2}$ so that

$$\overline{\cos \eta_s} = \frac{1}{\pi}\left|\sin \Lambda\right|$$

The constants a_K determined by the theory of Fourier series are

$$a_0 = \frac{2}{\pi^2}$$

$$a_1 = 0$$

$$a_K = \frac{4}{\pi^2}\left(1 - K^2\right) \quad \text{for even values of } K$$

$$a_K = 0 \quad \text{for odd values of } K$$

The time dependent differential equation governing heat flow is expressed as

$$\nabla^2 T + \frac{Q'}{k} = \frac{1}{\alpha^2}\frac{\partial T}{\partial \tau} \tag{A21}$$

where Q' is the rate at which heat is being internally generated per unit volume of mass. Physically there is no internally generated heat, but for the case of vanishing radial gradient the nonlinear radiation boundary conditions may be considered as internally generated heat. For a cylinder of radius ρ_0 and thickness t,

$$\frac{Q'\rho_0^2}{k} = \frac{\rho_0^2 H S a_s \,\overline{\cos \eta_s}}{kt} + \frac{\rho_0^2 J(0,h)\left(1 + \overline{\cos \eta_e}\right)e}{2kt} - \frac{\rho_0^2 e\sigma T^4}{kt}$$

where k is thermal conductivity.

52

or

$$\frac{\rho_0{}^2 Q'}{k} = \frac{\rho_0{}^2 HSa_s}{tk} \sum_{K=0}^{\infty} a_K \cos K\Lambda + \rho_0{}^2 \sin^2\left(\frac{\alpha_0}{2}\right)\frac{e\sigma T_e{}^4}{kt} b_0$$

$$- \rho_0{}^2 \sin^2\left(\frac{\alpha_0}{2}\right)\frac{e\sigma T_e{}^4}{kt} \cos \nu \cos \Lambda \sin\left[\left(\gamma_0 + \zeta\right) + \xi\right] b_0$$

$$+ \rho_0{}^2 \sin^2\left(\frac{\alpha_0}{2}\right)\frac{e\sigma T_e{}^4}{kt} \sum_{K=1}^{\infty} b_K \cos K\xi$$

$$- \rho_0{}^2 \frac{\sin^2}{2}\left(\frac{\alpha_0}{2}\right)\frac{e\sigma T_e{}^4}{kt} \cos \nu \cos \Lambda \sum_{K=1}^{\infty} b_K \left\{ \sin\left[\left(\gamma_0 + \zeta\right) + (1 + K)\xi\right] \right.$$

$$\left. + \sin\left[\left(\gamma_0 + \zeta\right) + (1 - K)\xi\right] \right\} - \frac{\rho_0{}^2 e\sigma T^4}{tk} \tag{A22}$$

where H is unity when the satellite is in the sunlight and zero when the satellite is in the earth's shadow. Let

$$T^4 \approx T_m{}^4 + 4T_m{}^3(T - T_m) = 4T_m{}^3 T - 3T_m{}^4$$

$$\frac{\partial T}{\partial \tau} = \frac{\partial T}{\partial \xi}\frac{d\xi}{d\tau} \approx \dot{\delta}\frac{\partial T}{\partial \xi}$$

$$\nabla^2 T = \frac{1}{\rho_0{}^2}\frac{\partial^2 T}{\partial^2 \Lambda}$$

$$e\sigma T_m{}^4 = E_m$$

$$\frac{1}{tk} = \lambda$$

$$Sa_s = E_s$$

$$e\sigma T_e{}^4 = E_e$$

$$\rho_0{}^2 \lambda E_s = \mu_s$$

$$\rho_0{}^2 \lambda E_m = \mu_m$$

$$\rho_0{}^2 \lambda E_e = \mu_e$$

$$\overline{\alpha^2} = \frac{\alpha^2}{\dot{\delta}}$$

where $\dot{\delta}$ is the time derivative of the orbit angle and α^2 is the thermal diffusivity.

The differential equation may be rewritten as

$$\frac{\partial^2 T}{\partial \lambda^2} - \frac{4\mu_m}{T_m} T - \left(\frac{\rho_0}{\overline{\alpha}}\right)^2 \frac{\partial T}{\partial \xi} = -3\mu_m - H\mu_s \sum_{K=0}^{\infty} a_K \cos K\Lambda$$

$$- \sin^2\!\left(\frac{\alpha_0}{2}\right)\mu_e b_0 + \sin^2\!\left(\frac{\alpha_0}{2}\right)\cos \nu \, \cos \Lambda \mu_e \, \sin\left[\left(\gamma_0\right.\right.$$

$$\left. + \zeta\right) + \xi \Big] b_0 - \sin^2\!\left(\frac{\alpha_0}{2}\right)\mu_e \sum_{K=1}^{\infty} b_K \cos K\xi$$

$$+ \sin^2\!\left(\frac{\alpha_0}{2}\right)\cos \nu \, \cos \Lambda \mu_e \sum_{K=1}^{\infty} \frac{b_K}{2} \left\{ \sin\left[\left(\gamma_0 + \zeta\right)\right.\right.$$

$$\left. + (1 + K)\xi\right] + \sin\left[\left(\gamma_0 + \zeta\right) + (1 - K)\xi\right]\Big\}$$

To determine $T(\xi,\Lambda)$, which is the surface temperature as a function of the orbit position and the angle Λ, assume a solution of the form

$$T(\xi,\Lambda) = T_H + T_p \tag{A23}$$

54

where

$$T_p(\xi,\Lambda) = H\left[\sum_{K=0}^{\infty} A_K(\xi)\cos K\Lambda\right] + \cos\Lambda\left[B_0(\xi) + B_K(\xi)\right] + \left[C_0 + C_K(\xi)\right] \quad (A24)$$

and T_H is the solution for no heat generation. If the assumed solution is operated on by the differential equation (A20) then

$$H\left[-K^2 \sum_{K=0}^{\infty} A_K(\xi)\cos K\Lambda\right] - \cos\Lambda\left[B_0(\xi) + B_K(\xi)\right] - \frac{4\mu_m}{T_m}\left\{H\sum_{K=0}^{\infty} A_K(\xi)\cos K\Lambda\right.$$

$$+ \cos\Lambda\left[B_0(\xi) + B_K(\xi)\right] + \left[C_0 + C_K(\xi)\right]\right\} - \left(\frac{\rho_0}{\bar{\alpha}}\right)^2 \left\{H\sum_{K=1}^{\infty} A_K'(\xi)\cos K\Lambda\right.$$

$$+ \cos\Lambda\left[B_0'(\xi) + B_K'(\xi)\right] + \left[C_K'(\xi)\right]\right\}$$

$$= -H\left(\mu_s \sum_{K=0}^{\infty} a_K \cos K\Lambda\right) + \cos\Lambda\left[\sin^2\left(\frac{\alpha_0}{2}\right)\cos \nu\mu_e \left(\sin\left[\left(\gamma_0 + \zeta\right) + \xi\right]b_0\right.\right.$$

$$+ \sum_{K=1}^{\infty} \frac{b_K}{2}\left\{\sin\left[\left(\gamma_0 + \zeta\right) + (1 + K)\xi\right] + \sin\left[\left(\gamma_0 + \zeta\right) + (1 - K)\xi\right]\right\}\right)\right]$$

$$+ \left\{\left[-3\mu_m - \sin^2\left(\frac{\alpha_0}{2}\right)\mu_e b_0\right] - \left[\sin^2\left(\frac{\alpha_0}{2}\right)\mu_e \sum_{K=1}^{\infty} b_K \cos K\xi\right]\right\}$$

where prime denotes differentiation with respect to ξ. This equation must be an identity and when similar parts are equated, the following equations result:

$$-K^2 A_K(\xi) - \frac{4\mu_m}{T_m} A_K(\xi) - \left(\frac{\rho_0}{\bar{\alpha}}\right)^2 A_K'(\xi) = -\mu_s a_K \quad (A25)$$

$$-B_0(\xi) - \frac{4\mu_m}{T_m} B_0(\xi) - \left(\frac{\rho_0}{\bar{\alpha}}\right)^2 B_0'(\xi) = \sin^2\left(\frac{\alpha_0}{2}\right)\cos \nu\mu_e \sin\left[\left(\gamma_0 + \zeta\right) + \xi\right]b_0$$

$$(A26)$$

$$-B_K(\xi) - \frac{4\mu_m}{T_m} B_K(\xi) - \left(\frac{\rho_0}{\bar{\alpha}}\right)^2 B_K'(\xi) = \sin^2\left(\frac{\alpha_0}{2}\right)\cos \nu\mu_e \sum_{K=1}^{\infty}\left(\frac{b_K}{2}\right)\left\{\sin\left[(\gamma_0 + \zeta)\right.\right.$$

$$\left.\left. + (1 + K)\xi\right] + \sin\left[(\gamma_0 + \zeta) + (1 - K)\xi\right]\right\}$$

(A27)

$$-\frac{4\mu_m}{T_m} C_0 = -3\mu_m - \sin^2\left(\frac{\alpha_0}{2}\right)\mu_e b_0$$

(A28)

$$-\frac{4\mu_m}{T_m} C_K(\xi) - \left(\frac{\rho_0}{\bar{\alpha}}\right)^2 C_K'(\xi) = -\sin^2\left(\frac{\alpha_0}{2}\right)\mu_e \sum_{K=1}^{\infty} b_K \cos K\xi$$

(A29)

The solutions to this set of five equations may be found by the use of integration factors or, in the case of constants, by algebraic manipulation as follows:

$$A_K(\xi) = \frac{\mu_s a_K}{\left(K^2 + \frac{4\mu_m}{T_m}\right)} + \hat{D}_K e^{-\left(\frac{\bar{\alpha}}{\rho_0}\right)^2\left(K^2 + \frac{4\mu_m}{T_m}\right)\xi}$$

(A30)

$$B_0(\xi) = -b_0\left(\frac{\bar{\alpha}}{\rho_0}\right)^2 \sin^2\left(\frac{\alpha_0}{2}\right)\cos \nu\mu_e \frac{\left(\frac{\bar{\alpha}}{\rho_0}\right)^2\left(1 + \frac{4\mu_m}{T_m}\right)\sin\left[(\gamma_0 + \zeta) + \xi\right] - \cos\left[(\gamma_0 + \zeta) + \xi\right]}{\left(\frac{\bar{\alpha}}{\rho_0}\right)^4\left(1 + \frac{4\mu_m}{T_m}\right)^2 + 1}$$

(A31)

$$B_K(\xi) = -\left(\frac{\bar{\alpha}}{\rho_0}\right)^2\cos \nu \sin^2\left(\frac{\alpha_0}{2}\right)\mu_e \sum_{K=1}^{\infty}\frac{b_K}{2}\left\{\frac{\left(\frac{\bar{\alpha}}{\rho_0}\right)^2\left(1 + \frac{4\mu_m}{T_m}\right)\sin\left[(\gamma_0 + \zeta) + (1 + K)\xi\right]}{\left(\frac{\bar{\alpha}}{\rho_0}\right)^4\left(1 + \frac{4\mu_m}{T_m}\right)^2 + (1 + K)^2} - \frac{(1 + K)\cos\left[(\gamma_0 + \zeta) + (1 + K)\xi\right]}{\left(\frac{\bar{\alpha}}{\rho_0}\right)^4\left(1 + \frac{4\mu_m}{T_m}\right)^2 + (1 + K)^2}\right.$$

$$\left. + \frac{\left(\frac{\bar{\alpha}}{\rho_0}\right)^2\left(1 + \frac{4\mu_m}{T_m}\right)\sin\left[(\gamma_0 + \zeta) + (1 - K)\xi\right]}{\left(\frac{\bar{\alpha}}{\rho_0}\right)^4\left(1 + \frac{4\mu_m}{T_m}\right)^2 + (1 - K)^2} - \frac{(1 - K)\cos\left[(\gamma_0 + \zeta) + (1 - K)\xi\right]}{\left(\frac{\bar{\alpha}}{\rho_0}\right)^4\left(1 + \frac{4\mu_m}{T_m}\right)^2 + (1 - K)^2}\right\}$$

(A32)

$$C_0 = \frac{3}{4} T_m + \frac{\sin^2 \frac{\alpha_0}{2}}{4} \frac{\mu_e}{\mu_m} T_m b_0 \tag{A33}$$

$$C_K(\xi) = \left(\frac{\overline{\alpha}}{\rho}\right)^2 \sin^2 \frac{\alpha_0}{2} \mu_e \sum_{K=1}^{\infty} b_K \frac{\left(\frac{\overline{\alpha}}{\rho}\right)^2 \frac{4\mu_m}{T_m} \cos K\xi + K \sin K\xi}{\left(\frac{\overline{\alpha}}{\rho}\right)^4 \left(\frac{4\mu_m}{T_m}\right)^2 + K^2} \tag{A34}$$

The homogeneous solution (T_H) is

$$T_H(\xi,\Lambda) = \sum_{K=0}^{\infty} D_K e^{-\left(\frac{\overline{\alpha}}{\rho}\right)^2 \left(K^2 + \frac{4\mu_m}{T_m}\right)\xi} \cos K\Lambda \tag{A35}$$

To determine D_K and $\hat{D}_K$, notice that all terms are continuous and remain finite except those multiplied by D_K and $\hat{D}_K$; therefore, in order to complete the solution it is necessary only to determine D_K and $\hat{D}_K$ so that $T(\xi,\Lambda)$ be continuous at

$$\xi = \pm \frac{\Omega}{2}$$

and remain finite. Let

$$x_K = \left(\frac{\overline{\alpha}}{\rho_0}\right)^2 \left(K^2 + \frac{4\mu_m}{T_m}\right)$$

$$G_K = \frac{\mu_s a_K \left(\frac{\overline{\alpha}}{\rho}\right)^2}{x_K}$$

The proper selections of D_K and $\hat{D}_K$ are

$$D_K = G_K \frac{\sinh x_K\left(\frac{\Omega}{2}\right)}{\sinh x_K \pi} e^{x_K \pi} H_2$$

$$\hat{D}_K = -G_K \frac{\sinh x_K\left(\pi - \frac{\Omega}{2}\right)}{\sinh x_K \pi} H_1$$

where

$$H_1 = 1 \quad \text{and} \quad H_2 = 0 \qquad \left(-\frac{\Omega}{2} \leqq \xi \leqq \frac{\Omega}{2}\right)$$

$$H_1 = 0 \quad \text{and} \quad H_2 = 1 \qquad \left[\frac{\Omega}{2} \leqq \xi \leqq \left(2\pi - \frac{\Omega}{2}\right)\right]$$

and

$$-\frac{\Omega}{2} \leqq \xi \leqq \left(2\pi - \frac{\Omega}{2}\right)$$

The formal solution is

$$T(\xi,\Lambda) = T_H(\xi,\Lambda) + T_p(\xi,\Lambda)$$

$$= H_1 \sum_{K=0}^{\infty} G_K\left[1 - \frac{\sinh x_K\left(\pi - \frac{\Omega}{2}\right)}{\sinh x_K \pi} e^{-x_K \xi}\right]\cos K\Lambda$$

$$+ H_2 \sum_{K=0}^{\infty} G_K \frac{\sinh x_K \frac{\Omega}{2}}{\sinh x_K \pi} e^{-x_K(\xi-\pi)}\cos K\Lambda$$

$$+ \cos \Lambda\left[B_0(\xi) + B_K(\xi)\right] + \left[C_0 + C_K(\xi)\right] \tag{A36}$$

where $e = 2.7183$.

The accuracy of equation (A36) is dependent on three primary conditions: magnitude of the temperature variations, the satellite orbital elements, and the satellite tumble rate.

The first condition determines the validity of the linearization of the differential equation. To examine the effect of the linearization of equation (A21), it is advantageous to solve a simpler problem. Consider a tumbling cylinder, with open ends and nonradiating inner walls,

58

and let the principal axis be 90° from the sun; neglect earth thermal and reflected solar radiation. The governing differential equation is

$$\nabla^2 T + \frac{Q'}{k} = 0$$

where

$$\frac{\rho_0^2 Q'}{k} = \frac{\rho_0^2 S a_s}{tk} \cos^* \Lambda - \frac{\rho_0^2 e\sigma T^4}{tk}$$

when

$$T^4 \approx T_m^4 + 4T_m^3(T - T_m) = 4T_m^3 T - 3T_m^4$$

$$\lambda = \frac{1}{tk}$$

$$e\sigma T_m^4 = E_m$$

$$S a_s = E_s$$

$$\rho_0^2 \lambda E_m = \mu_m$$

$$\rho_0^2 \lambda E_s = \mu_s$$

$$\nabla^2 T = \frac{1}{\rho_0^2} \frac{d^2 T}{d\Lambda^2}$$

$$\omega^2 = \frac{4\mu_m}{T_m}$$

Then the differential equation becomes

$$\frac{d^2 T}{d\theta^2} - (\omega^2)T = -\mu_s \cos^* \Lambda - 3\mu_m$$

with the straightforward solution from reference 14

$$T = \frac{\mu_s}{2\omega} \frac{\cosh \omega\Lambda}{(1 + \omega^2)\sinh \frac{\omega\pi}{2}} + \frac{\mu_s}{1 + \omega^2} \cos \Lambda + \frac{3T_m}{4} \qquad \left(0 \leqq \Lambda \leqq \frac{\pi}{2}\right)$$

(A37)

$$T = \frac{\mu_s \cosh \omega(\Lambda - \pi)}{2\omega(1 + \omega^2)\sinh \frac{\omega\pi}{2}} + \frac{3T_m}{4} \qquad \left(\frac{\pi}{2} \leqq \Lambda \leqq \pi\right)$$

which satisfies the linearized differential equation along with continuity of T and $dT/d\theta$. However, this solution does not satisfy the conditions of equilibrium, specifically

Absorbed heat = Radiated heat

This can be corrected by multiplying the solution by some suitable constant, which is determined by requiring that

$$\frac{z_1^4}{2\pi} \int_0^{2\pi} T^4 d\Lambda = T_m^4$$

and

$$z^4 = \frac{2\pi T_m^4}{\int_0^{2\pi} T^4 d\Lambda}$$

(A38)

where T is given by equation (A37). In figures 33 and 34 the linearized and the corrected linearized solutions are shown with the numerically integrated solution for two material thicknesses. In both cases the linearized solution is consistently higher than the numerical solution. This may be explained by noticing that the linearized expression $4T_m^3 - 3T_m^4$ is always less than T^4 except for T equal to T_m; but T^4 is directly proportional to the energy being radiated away, so that T in the linearized solution must be too high in order to compensate for the loss in radiative power.

The second condition determines the applicability of equation (A8). It should be noted that equation (A8) is exact only for zero altitude, but the effect of this term in the temperature distribution is always small and considering the additional complexity that would be required to correct it, the use of equation (A8) is justifiable for altitudes on the order of 200 to 300 nautical miles. The third condition may be checked by the method of reference 14.

It has been shown that one corrected form of equation (A36) is

$$T_{corr}(\xi,\Lambda) = ZT(\xi,\Lambda) \tag{A39}$$

where

$$Z^4 = \frac{4\pi^2 T_m{}^4}{\displaystyle\int_0^{2\pi}\int_0^{2\pi}\Bigl[T(\xi,\Lambda)\Bigr]^4 d\xi\ d\Lambda} \tag{A40}$$

The correction factor Z in most cases must be determined numerically. An approximate Z may be found much simpler by the following method. Let

$$T(\Lambda) = \frac{1}{2\pi}\int_0^{2\pi} T(\xi,\Lambda)d\xi \tag{A41}$$

$$T(\xi) = \frac{1}{2\pi}\int_0^{2\pi} T(\xi,\Lambda)d\Lambda \tag{A42}$$

Then find

$$Z_\Lambda{}^4 = \frac{2\pi T_m{}^4}{\displaystyle\int_0^{2\pi}\Bigl[T(\Lambda)\Bigr]^4 d\Lambda} \tag{A43}$$

$$Z_\xi{}^4 = \frac{2\pi T_m{}^4}{\displaystyle\int_0^{2\pi}\Bigl[T(\xi)\Bigr]^4 d\xi} \tag{A44}$$

so that

$$Z \approx Z_\Lambda Z_\xi \qquad \text{(A45)}$$

Numerical Example of Surface Temperature Distributions

To illustrate the method used in this paper for finding surface temperature distributions the following example is presented. The case selected is for the Lewis sensors since the gradient effects on this experiment are critical. Consider the satellite to be tumbling and in the attitude where the coldest telemetry temperature is expected. For this condition

$\zeta = 180^\circ$ $\qquad\qquad$ $\gamma_0 = 0^\circ$

$\Omega = 225^\circ = 3.92$ radians $\qquad\qquad$ $\epsilon = 0^\circ$

$\dfrac{A_s}{A_T} = \dfrac{118}{584} = 0.202$ $\qquad\qquad$ $p = 0.625$

$\sin \alpha_0 = \dfrac{R_0}{R_0 + \text{Altitude}} = \dfrac{3438}{3438 + 400} = 0.895$ $\qquad$ $v = 0^\circ$

$\cos \alpha_0 = 0.446$ $\qquad\qquad$ $\alpha_0 = 63.5^\circ$

Material properties are taken as

$k = 0.164 \dfrac{\text{Btu}}{\text{min-in-}^\circ\text{F}}$ $\qquad a_s = 0.32$ $\qquad e = 0.82$

$t = 0.02$ in. $\qquad \rho_0 = 11.0$ in. $\qquad \alpha^2 = 8.78$ in.^{2}/min

First the mean orbit temperature T_m will be found from the alternative method (eq. (A9)) where the surface is at uniform temperature as follows:

$$T_m^4 = \left[\frac{A_s}{A_T} p + \frac{(1 - \cos \alpha_0)r_e}{2\pi} \cos \epsilon\right]\frac{S a_s}{\sigma e} + \left(\frac{1 - \cos \alpha_0}{2}\right)T_e^4$$

62

$$T_m^4 = \left[(0.202)(0.625) + \frac{(1 - 0.446)(0.4)(1.0)}{6.28}\right] \frac{(0.04968)(0.32)}{\left(2 \times 10^{-13}\right)(0.82)}$$

$$+ \left(\frac{1 - 0.446}{2}\right)(450)^4$$

$$T_m^4 = \left(157.0 \times 10^8\right) + \left(114.2 \times 10^8\right) = 271.2 \times 10^8$$

$$T_m = 406^\circ \text{ R} = -54^\circ \text{ F}$$

Now a numerical expression for temperature will be found. Equation (A41) can be expressed in the form

$$T(\Lambda) = \frac{1}{2\pi} \int_0^{2\pi} T(\xi, \Lambda) d\xi$$

$$= T_m + \frac{\Omega}{2\pi} \sum_{K=1}^{\infty} G_K \cos K\Lambda - \left(\frac{\bar{a}}{\rho_0}\right)^2 \cos \nu \, \sin^2\left(\frac{\alpha_0}{2}\right)\left(\frac{\mu_e}{\mu_m}\right) \frac{b_1}{2}\left[\frac{\sin\left(\gamma_0 + \zeta\right)}{x_1}\right] \cos \Lambda$$

where

$$\lambda = \frac{1}{tk} = \frac{1}{(0.02)(0.164)} = 304.87$$

$$E_s = Sa_s = (0.04968)(0.32) = 0.01589$$

$$E_e = e\sigma T_e^4 = (0.82)\left(2 \times 10^{-13}\right)(450)^4 = 0.006724$$

$$E_m = e\sigma T_m^4 = (0.82)\left(2 \times 10^{-13}\right)(406)^4 = 0.004407$$

$$\rho_0^2 = 121 \text{ in.}^2$$

$$\mu_s = \rho_0^2 \lambda E_s = (121)(304.87)(0.01589) = 586.44$$

$$\mu_e = \rho_0^2 \lambda E_e = (121)(304.87)(0.006724) = 248.04$$

$$\mu_m = \rho_0 \lambda E_m = (121)(304.87)(0.004407) = 162.57$$

$$\dot{\delta} = \frac{2\pi}{P} = \frac{6.28}{98.1} = 0.0641 \text{ radian/min}$$

$$\overline{\alpha}^2 = \frac{\alpha^2}{\dot{\delta}} = \frac{8.78}{0.0641} = 137$$

$$\left(\frac{\overline{\alpha}}{\rho_0}\right)^2 = \frac{137}{121} = 1.132$$

$$\frac{4\mu_m}{T_m} = \frac{4(162.57)}{406} = 1.60$$

$$a_0 = \frac{2}{\pi^2} = 0.2028$$

$$a_1 = 0$$

$$a_2 = \frac{4}{\pi^2\left[1 - (2)^2\right]} = -0.1352$$

$$a_4 = \frac{4}{\pi^2\left[1 - (4)^2\right]} = -0.0270$$

$$a_6 = \frac{4}{\pi^2\left[1 - (6)^2\right]} = -0.0116$$

$$a_8 = -0.0064$$

$$a_{10} = -0.0041$$

$$g = \frac{a_s r_e S \cos \epsilon}{e\sigma T_e^4} = \frac{(0.32)(0.4)(0.04968)(1.0)}{(0.82)\left(2 \times 10^{-13}\right)(450)^4} = 0.9457$$

$$b_0 = \frac{1 + g}{\pi} = 1 + \frac{0.9457}{3.14} = 1.301$$

$$b_1 = \frac{g}{2} = 0.4728$$

Now select even values of K and solve for x_K and G_K as shown in the following table:

K	K^2	$K^2 + \dfrac{4\mu_m}{T_m}$	$x_K = \left(K^2 + \dfrac{4\mu_m}{T_m}\right) x \left(\dfrac{\bar{\alpha}}{\rho_0}\right)^2$	a_K	$a_K \mu_s$	$G_K = \dfrac{\mu_s a_K \left(\dfrac{\bar{\alpha}}{\rho_0}\right)^2}{x_K}$
0	0	1.60	1.8179	0.2028	118.93	65.42
2	4	5.60	6.3459	-.1352	-79.28	-12.49
4	16	17.60	19.9299	-.0270	-15.83	-.79
6	36	37.60	42.569	-.0116	-6.80	-.16
8	64	65.60	74.265	-.0064	-3.75	-.05
10	100	101.60	115.017	-.0041	-2.40	-.02

For $K = 1.0$,

$$x_1 = \left(K^2 + \frac{4\mu_m}{T_m}\right)\left(\frac{\bar{\alpha}}{\rho_0}\right)^2 = (1.0 + 1.60)(1.132) = 2.9450$$

Now the surface temperature T can be found as a function of the polar angle Λ

$$T(\Lambda) = T_m + \frac{\Omega}{2\pi}\sum_{K=1}^{\infty} G_K \cos K\Lambda$$

$$- \left(\frac{\bar{\alpha}}{\rho_0}\right)^2 \cos \nu \, \sin^2\left(\frac{\alpha_0}{2}\right)\left(\frac{\mu_e}{\mu_m}\right)\left(\frac{b_1}{2}\right)\left[\frac{\sin(\gamma_0 + \zeta)}{x_1}\right]\cos \Lambda$$

$$T(\Lambda) = 406 + \frac{3.92}{6.28}\left[(-12.49)\cos 2\Lambda + (-0.79)\cos 4\Lambda + \ldots\right]$$

$$- (1.132)(\cos 0^\circ)\left[\sin^2\left(\frac{63.5}{2}\right)\right]\left(\frac{248.04}{162.57}\right)\left(\frac{0.4728}{2}\right)\left[\frac{\sin(0^\circ + 180^\circ)}{2.9450}\right]\cos \Lambda$$

Since $\sin 180^\circ = 0$, the second term becomes 0 and

$$T(\Lambda) = 406 + (0.625)(-12.49)\cos 2\Lambda$$

$$T(\Lambda) = 406 - 7.80 \cos 2\Lambda \quad \text{(given in } ^\circ R)$$

The solution to this problem is plotted in figure 32.

Next find the surface temperature effects due to time $T(\xi)$ from equation (A42)

$$T(\xi) = \frac{1}{2\pi} \int_0^{2\pi} T(\xi,\Lambda)d\Lambda$$

$$T(\xi) = T_m - \frac{\Omega}{2\pi} G_0 + H_1\left\{G_0\left[1 - \frac{\sinh x_0\left(\pi - \frac{\Omega}{2}\right)}{\sinh x_0\pi} e^{-x_0\xi}\right]\right\}$$

$$+ H_2\left[G_0 \frac{\sinh x_0\frac{\Omega}{2}}{\sinh x_0\pi} e^{-x_0(\xi-\pi)}\right]$$

$$+ \left(\frac{\alpha}{\rho}\right)^2 \sin^2\left(\frac{\alpha_0}{2}\right)\mu_e \sum_{K=1}^{\infty} b_K \frac{\left(\frac{\alpha}{\rho}\right)^2\left(\frac{4\mu_m}{T_m}\right)\cos K\xi + K\sin K\xi}{\left(\frac{\alpha}{\rho}\right)^4\left(\frac{4\mu_m}{T_m}\right)^2 + K^2}$$

where $e = 2.7183$. After dropping negligible terms the equation becomes

$$T(\xi) \approx 365 + H_1\left(65.4 - 1.504e^{-1.82\xi}\right) + H_2\left[7.25e^{-1.82(\xi-\pi)}\right]$$

$$+ 15.5\cos \xi + 8.6\sin \xi + 3.9\cos 2\xi + 4.3\sin 2\xi$$

The solution is plotted in figure 38. It should be noted that in figure 38 the effects of conductivity from other sectors to the Lewis sensors has been neglected.

Solutions for Z_Λ and Z_ξ from equations (A43) and (A44) for this problem gives

$$Z_\Lambda = 0.999$$

$$Z_\xi = 0.993$$

and from equation (A45)

$$Z \approx Z_\Lambda Z_\xi$$

$$Z = 0.9923$$

Then, the corrected mean temperature in the cold case (considering circumferential surface gradients and time gradients) is

$$ZT_m = 0.992 \times 406 = 402.8$$

The mean temperature drop in this case is only 3.2° F, although calculations have shown that in the hot case the mean temperature drop is 13° F.

APPENDIX B

DEVELOPMENT TESTS AND TEST RESULTS

A large amount of testing was done as part of the thermal design of Explorer XIII. Although the approach taken in these tests was that of proof testing rather than basic research, the results which may be of general interest are included in this paper. These results, however, do not represent the entire test program conducted with materials and coatings for Explorer XIII.

Vacuum Ultraviolet Radiation

A long recognized problem associated with thermal design is the detrimental effect of the ultraviolet portion of the solar spectrum on surface coatings. This effect most often appears as a change in solar absorptivity, although in some cases the material itself may be adversely affected. To study this effect in a quantitative manner, a test was conducted using a General Electric B-H6 mercury arc lamp to irradiate specimens in a bell jar evacuated to 1×10^{-4} mm of mercury. The solar spectrum was duplicated between wavelengths of 0.24 and 0.42 micron and the radiation intensity at the surface over this wavelength range was 0.01236 watt/cm^2. A photograph of the test setup is shown in figure 39 and the results are presented in the following table. The temperature of the specimens during radiation was approximately 85° F.

Material or coating	Type	Thickness, mils	Source	Exposure time, hr	Results
Titanium dioxide white paint	Silicone resin	3	Marshall Space Flight Center (MSFC)	385	Severe yellowing in first 70 hours, no appreciable increase after 70 hours, no change in adhesion or composition
Aluminum lacquer	Acrylic (A-10)	1	U.S. Naval Research Laboratory (NRL)	385	No color change, no change in adhesion or composition
Aluminum oxide	Rokide A	13	Norton Company	385	Slight darkening during first 100 hours, no appreciable increase after first 100 hours, no change in adhesion or composition
Sandblasted 410 stainless steel, heated at 600° F for 5 minutes				400	No color change
Vapor deposited aluminum and silicon monoxide films on beryllium copper		0.28 (approximately)	U.S. Army Engineer Research and Development Laboratory	400	No color change, no change in adhesion or composition
Strong black lacquer	Acrylic (DMA 358)	3	Ditzler Color Division, Pittsburg Plate Glass Company	400	No color change, no change in adhesion or composition
Mixing white lacquer	Acrylic (DMA 311)	3	Ditzler Color Division, Pittsburg Plate Glass Company	400	Slight yellowing in first 60 hours, no change in adhesion
Enameled copper wire		3	Goddard Space Flight Center		No color change, no change in adhesion or composition
Lusterless white enamel	Resin (F93-WC9)	1	Sherwin-Williams Paint Company	385	Moderate yellowing in first 60 hours, no change in adhesion
Flat black enamel	Resin (F65-B2)	1	Sherwin-Williams Paint Company	385	No color change, no change in adhesion
Silicone rubber	No. 916		Dow Corning Corporation	385	No color change, no change in texture

Some general observations can be made from even this simple test. It appears that the white surfaces show discoloration effects within about the first 100 hours and do not become appreciably worse after that time. This characteristic would indicate that if this is the only ultraviolet effect to be studied, tests at one solar intensity might not have to exceed this duration.

It can also be noted from the table that, of the paints examined, the acrylics seem superior in their ability to resist color change.

Although considerable work is being done on vacuum ultraviolet radiation (for example, refs. 18 and 19) these tests are generally performed at several solar intensities. A need appears to exist for experimental studies on long term vacuum ultraviolet effects at one intensity.

L
1
7
3
7

Proton Radiation

The Explorer XIII micrometeoroid satellite is not expected to experience high levels of proton and electron radiation because of its relatively low orbit, however, some preliminary proof testing was done on some materials of Explorer XIII jointly with a program being conducted by the Langley Instrument Research Division (IRD). These tests were conducted in the 22 Mev proton accelerator at the Oak Ridge National Laboratory (ORNL). Although the primary purpose of these tests was to evaluate the performance of solar cells and transistors (ref. 20), the testing of material samples was useful in determining high energy radiation effects on some of the material properties. Reference 21 contains a good discussion of high energy particle effects on a number of material properties. The specimens irradiated at the Oak Ridge National Laboratory, however, were examined primarily to observe the following effects:

(1) Optical properties

(2) Crystalline structure

(3) Tensile yield load

(4) Bonding characteristics of adhesives

Table III is a list of the specimens radiated at ORNL. Reference 20 presents a description of the test setup and photographs of the mounting apparatus. The material test specimens were irradiated for 5 minutes in a 22 Mev proton beam flux of 6.5×10^{10} protons/cm2/sec (1.95×10^{13} protons/cm^2 total).

Optical properties: Only three of the specimens radiated showed discoloration effects. Strangely, all of these materials were involved in the solar cell installation. Two possible bonding agents were tested and both discolored. The General Electric Company's RTV-40 silicone rubber elastomer turned from white to grey, the Armstrong Products Company's modified C-1 epoxy adhesive turned from white to tan, and the quartz glass solar cell window turned to a darkened shade in the radiated area. The red Dow Corning silicone rubber, however (which is used as a quartz glass mounting gasket) did not discolor as did the white RTV-40 silicone rubber bonding agent.

Crystalline structure: All of the specimens radiated were examined under a 250 power microscope and compared with nonradiated duplicates. It was found that for all the specimens, including those which discolored, there was no change in the crystalline structure of the materials discernible at this magnification.

Tensile load tests: Table IV presents a summary of the effects of the radiation on the percentage changes in ultimate tensile load and elongation in a 4-inch specimen. Generally the accuracy of these data appears to be in the order of ±5 percent. Because of the limited number of specimens tested, however, it is difficult to be certain whether the changes noted in some of the materials is a result of the radiation or of some discrepancies in the specimens themselves. It does appear from the quantitative data, however, that the silicone rubber is affected strongly, and shows an appreciable reduction in ultimate tensile load and elongation after radiation. In every case where an external coating was applied, the coating spalled during the tensile test, both on radiated and nonradiated specimens.

Adhesive bonding characteristics: A cursory comparison was made between the bonding characteristics of the radiated and nonradiated adhesives (RTV-40 silicone rubber and C-1 epoxy adhesive). No appreciable change was detected, and the bonding characteristics of both of these agents, for the radiated and nonradiated conditions, appeared satisfactory. The results of the 22 Mev proton radiation test at ORNL, as given in reference 20 and this paper can be summarized as follows: The largest effects as noted in the reference were in the performance of the solar cells and transistors. Large losses in short circuit current and load current were experienced by the solar cells, and large losses in transistor gains were also noted after radiation. Radiation effects on the materials to be used in the Explorer XIII showed discoloration of the adhesives and quartz glass and a reduction of tensile load and elongation of silicone rubber.

Absorptivity and Emissivity Measurements

When a survey of the literature was made to find reliable values of surface absorptivity and emissivity of the materials and coatings to be used, it became apparent that direct measurements using material samples were necessary. Wherever possible the measurements were made at the Langley Research Center, and where the necessary facilities were not available, measurements were made on a contract basis. Samples were prepared by the identical processes used in fabrication of the satellite surfaces. Tables V and VI present the results of these tests. It will be noted that some of the values were for materials and coatings which were not used on Explorer XIII, but were considered promising for use in other satellite applications. The compositions of some of the paints used in this investigation are given in table VII.

These data were obtained from reflectance curves for different wavelength ranges. The Langley values of solar absorptivity were obtained from reflectance values between 0.26 and 2.6 microns with the Beckman DK-1 spectrophotometer. These data were obtained by Langley IRD. Values at wavelengths between 0.3 and 1.8 microns were obtained at Lockheed Aircraft Corporation with a Cary spectrophotometer and at wavelengths between 2 and 22 microns with a Perkin-Elmer Model 13-U spectrophotometer and Hohlraum reflectometer. The Lockheed measurements were made on contract using samples prepared at Langley.

Solar absorptivity and total hemispherical emissivity were reduced from the reflectance curves by the method of reference 22. The solar energy distribution used by the Langley center to obtain a_s is that given in reference 23, although the Lockheed values were based on the solar spectrum of reference 24. Very good agreement between the Langley and Lockheed values of a_s can be noted however. Values of a_s and e from reference 22 are also compared in table V. Good agreement in emissivity is noted. The largest discrepancy seen between the a_s values is the value for 410 stainless steel with sandblast and thermal treatment as given in reference 22. For this specimen, a difference of about 10 percent in a_s is apparent. This may be due to the fact that since the specimens discussed in reference 22 were not prepared at Langley, the method of preparation may have been slightly different thus affecting the surface properties.

REFERENCES

1. Posner, Jack, ed.: Considerations Affecting Satellite and Space Probe Research With Emphasis on the "Scout" as a Launch Vehicle. NASA TR R-97, 1961.

2. Sibulkin, M.: Heat Transfer Near the Forward Stagnation Point of a Body of Revolution. Jour. Aero. Sci. (Readers' Forum), vol. 19, no. 8, Aug. 1952, pp. 570-571.

3. Fay, J. A., and Riddell, F. R.: Theory of Stagnation Point Heat Transfer in Dissociated Air. Jour. Aero. Sci., vol. 25, no. 2, Feb. 1958, pp. 73-85, 121.

4. Dusinberre, G. M.: Numerical Methods for Transient Heat Flow. Trans. A.S.M.E., vol. 67, no. 8, Nov. 1945, pp. 703-712.

5. Van Driest, E. R.: The Problem of Aerodynamic Heating. Aero. Eng. Rev., vol. 15, no. 10, Oct. 1956, pp. 26-41.

6. Ames Research Staff: Equations, Tables and Charts for Compressible Flow. NACA Rep. 1135, 1953. (Supersedes NACA TN 1428.)

7. Abarbanel, Saul: Radiative Heat Transfer in Free-Molecule Flow. Jour. Aerospace Sci., vol. 28, no. 4, Apr. 1961, pp. 299-307.

8. Minzner, R. A., Champion, K. S. W., and Pond, H. L.: The ARDC Model Atmosphere, 1959. Air Force Surveys in Geophysics No. 115 (AFCRC-TR-59-267), Air Force Cambridge Res. Center, Aug. 1959.

9. Morris, J. A., and Byrd, R. J.: Ballistic Performance and Outgassing Studies of X248-A9 Rockets at Simulated Altitude Conditions. AEDC-TN-60-229 (Contract No. AF 40(600)-800 S/A 11(60-110)), Arnold Eng. Dev. Center, Dec. 1960.

10. Hibbs, A. R.: The Temperature of an Orbiting Missile. Progress Rep. No. 20-294 (Contract No. DA-04-495-Ord 18), Jet Propulsion Lab., C.I.T., Mar. 28, 1956.

11. Heller, Gerhard: Thermal Control of the Explorer Satellites. ARS Jour., vol. 30, no. 4, Apr. 1960, pp. 344-352.

12. Hass, Georg, Drummeter, L. F., Jr., and Schach, Milton: Temperature Stabilization of Highly Reflecting Spherical Satellites. Jour. Optical Soc. of America, vol. 49, no. 9, Sept. 1959, pp. 918-924.

L
1
7
3
7

13. Drummeter, L., and Schach, M.: Satellite Temperature Control. NRL Participation in the CSAGI Rocket and Satellite Conference September 30 - October 5, 1957, Rep. 5165, U.S. Naval Res. Lab., Jan. 5, 1959, pp. 67-72.

14. Charnes, A., and Raynor, S.: Solar Heating of a Rotating Cylindrical Space Vehicle. ARS Jour., vol. 30, no. 5, May 1960, pp. 479-484.

15. Snoddy, W. C.: Theoretical and Measured Temperatures of Explorer IV. Rep. No. DV-TN-6-59, Dev. Operations Div., Army Ballistic Missile Agency (Redstone Arsenal, Ala.), Mar. 14, 1959.

16. Gaumer, R. E.: Determination of the Effects of Satellite Environment on the Thermal Radiation Characteristics of Surfaces. [Preprint] 339C, Soc. Automotive Eng., 1961.

17. King-Hele, D. G., and Gilmore, D. M. C.: The Effect of the Earth's Oblateness on the Orbit of a Near Satellite. Tech. Note No. G.W. 475, British R.A.E., Oct. 1957.

18. Cowling, J. E., Alexander, A., Noonan, F., Kagarixe, R., and Stokes, S.: The Effects of Ultraviolet Radiation on Organic, Film-Forming Polymers. First Symposium - Surface Effects on Spacecraft Materials, Francis J. Clauss, ed., John Wiley & Sons, Inc., c.1960, pp. 364-377.

19. Gaumer, Roger E., Clauss, Francis J., Sibert, Merle E., and Shaw, Clyde C.: Materials Effects in Spacecraft Thermal Control. LMSD-704019, Lockheed Aircraft Corp., Nov. 1960.

20. Hulten, W. C., Honaker, W. C., and Patterson, John L.: Irradiation Effects of 22 and 240 Mev Protons on Several Transistors and Solar Cells. NASA TN D-718, 1961.

21. Chalmers, Bruce: Physical Metallurgy. John Wiley & Sons, Inc., c.1959.

22. Shipley, W. S., and Thostesen, T. O.: Radiative Properties of Surfaces Considered for Use on The Explorer Satellites and Pioneer Space Probes. Memo. No. 20-194 (Contract No. DA-04-495 ORD 18), Jet Propulsion Lab., C.I.T., Feb. 15, 1960.

23. Forsythe, William Elmer: Smithsonian Physical Tables. Ninth rev. ed., Smithsonian Misc. Coll., vol. 120, 1956.

24. Johnson, Francis S.: The Solar Constant. Jour. Meteorology, vol. 11, no. 6, Dec. 1954, pp. 431-439.

L
1
7
3
7

L-1737

TABLE I.- DESCRIPTION OF MATERIALS AND COATINGS USED ON

THE EXPLORER XIII MICROMETEOROID SATELLITE

Component	Material	Coating	Source
Nose cone	410 stainless steel	Exposed exterior - sandblasted with 100 mesh grit heated in air at 600° F for 5 minutes	Langley Research Center
		Exterior surface under sounding boards - 2 coats flat black enamel (F65B2)	Sherwin-Williams Paint Co.
		Interior - vapor deposited gold	Swedlow, Inc.
Telemetry packs	2024-T aluminum alloy	Vapor deposited gold	Swedlow, Inc.
Mounting bulkhead	Fiberglas	Vapor deposited gold	Swedlow, Inc.
Antennas	6061 aluminum alloy	Chromic acid anodizing	Langley Research Center
Solar cell ring	1100-H14 aluminum	Exposed exterior - 2 coats primer and 4 coats strong black lacquer (DMA 358)	Ditzler Color Div., Pittsburg Plate Glass Co.
		Interior - sulphuric acid anodize with black dye	Langley Research Center
Solar cell frames	2024 aluminum alloy	Exterior - 0.013-inch aluminum oxide (Rokide A)	Norton Corp.
		Interior - 1 coat primer and 2 coats flat black enamel (F65B2)	Sherwin-Williams Paint Co.
Solar cell bonding agent	Silicone rubber compound (RTV-40)	--------------------------	General Electric Co.
Sounding boards	410 stainless steel	Exterior - sandblasted with 100 mesh grit - heated in air at 600° F for 5 minutes	Langley Research Center
		Interior - 2 coats flat black enamel (F65B2)	Sherwin-Williams Paint Co.
Langley pressure cell detectors	Beryllium copper	Exterior - vapor deposited aluminum and silicon monoxide films	U.S. Army Engineer Research and Development Laboratories
Lewis grid detectors	304 stainless steel	Exterior - 1 coat white lusterless quick dry white enamel (F93-WC9)	Sherwin-Williams Paint Co.
		Interior - aluminum foil sheet	Langley Research Center
Goddard detectors	Enameled copper wire	Exterior - none	Goddard Space Flight Center
		Interior - aluminum foil sheet	Langley Research Center
Fourth-stage transition section	AZ31B magnesium alloy	Exposed exterior - 2 coats primer and 4 coats strong black lacquer (DMA 358)	Ditzler Color Div., Pittsburg Plate Glass Co.
		All other - aluminum foil sheet or tape	Astronautics Div., Chance Vought Corp.

TABLE II.- MATERIAL PROPERTIES OF EXPOSED SURFACE USED IN THE

EXPLORER XIII SATELLITE THERMAL DESIGN

Component	a_s	e	mc, Btu/°F	A_T, in.^{2}
Nose cone less sounding boards and solar cells . .	0.71	0.42	1.354	504
Sounding boards	0.71	0.42	0.217	222
Composite solar cell ring	0.57	0.79	1.451	337
Composite solar cells on forward face	0.41	0.89	0.145	32.4
Pressure cell sector	0.19	0.16	3.30	2816
Lewis sector	0.32	0.82	1.677	584
Goddard sector	0.66	0.69	0.925	565
Fourth-stage transition sector	0.93	0.74	0.598	380

TABLE III.- SPECIMENS RADIATED AT ORNL

Specimen	Description
1	General Electric RTV-40 silicone rubber on AZ31B magnesium alloy
2	Armstrong Products Co. modified C-1 epoxy adhesive on AZ31B magnesium alloy
3	Bare solar cell bonded to AZ31B magnesium alloy with RTV-40 silicone rubber
4	Bare solar cell bonded to AZ31B magnesium alloy with C-1 epoxy adhesive
5	Solar cell with 1/16-inch quartz glass window bonded to AZ31B magnesium alloy with RTV-40 silicone rubber
6	Solar cell with 1/16-inch quartz glass window bonded to AZ31B magnesium alloy with C-1 epoxy adhesive
7	3-mil-thick TiO_2 silicone base white paint on 2024-T3 aluminum alloy
8	3-mil-thick TiO_2 silicone base white paint on AZ31B magnesium alloy
9	1/2-mil annealed aluminum foil
10	2-mil-thick flat black enamel on 2024-T3 aluminum alloy
11	1-mil aluminum paint (formula A-10, NRL) on 2024-T3 aluminum alloy
12	6061-T6 aluminum alloy with chromic anodized surface
13	1/16-inch quartz glass
14	1-mil beryllium copper
15	Dow Corning silicone rubber
16	410 stainless steel, sandblasted and thermally treated
17	410 stainless steel, sandblasted and thermally treated, 12-mil Rokide A sprayed on
18	410 stainless steel, sandblasted
19	Duplicate of specimen 8
20	Duplicate of specimen 17

TABLE IV.- EFFECTS OF 22 MEV PROTON RADIATION

ON PROPERTIES OF MATERIALS

Material	Treatment	Percent change in ultimate tensile load (a)	Percent change in elongation of a 4-inch specimen (a)
410 stainless steel	Sandblasted with 100 mesh grit	0	-1.1
410 stainless steel	Sandblasted with 100 mesh grit, heated in air at 600° F for 5 minutes	0	+2.1
410 stainless steel	Sandblasted with 100 mesh grit, heated in air at 600° F for 5 minutes, 0.014-inch Rokide A coating	+1.5	+5.3
2024-T3 aluminum alloy	3 coats titanium dioxide white paint (MSFC)	-5.8	+3.7
2024-T3 aluminum alloy	1 coat zinc chromate primer - 2 coats Sherwin Williams flat black enamel F65B2	(b)	(b)
2024-T3 aluminum alloy	1 coat aluminum paint (formula A-10, NRL)	-1.7	+12.5
AZ31B magnesium alloy	3 coats titanium dioxide white paint (MSFC)	-1.3	+2.4
6061-T3 aluminum alloy	Chromic acid anodized	-1.7	+4.1
Beryllium copper	----------------------	+5.6	-16.3
Silicone rubber	----------------------	-41.6	-45.0

^aPlus sign indicates an increase after radiation and minus sign indicates a decrease after radiation.

^bTensile specimen accidentally notched; therefore, no valid results.

TABLE V.- SOLAR ABSORPTIVITY AND TOTAL HEMISPHERICAL EMISSIVITY OF MATERIALS AND COATINGS

Specimen	Material	Treatment or coating	Solar absorptivity			Total hemispherical emissivity at 80° F		
			Langley	Lockheed	Ref. 22	Langley	Lockheed	Ref. 22
1	410 stainless steel	Sandblasted with 100 mesh grit, heated in air at 600° F for 5 minutes	0.74	0.71	0.81		0.42	0.43
2	410 stainless steel	Same as specimen 1 but with 0.013-inch Rokide A coating	.25	.27	.28		.71	.77
3	347 stainless steel	Sandblasted with 100 mesh grit		.63			.46	
4	347 stainless steel	Sandblasted with 100 mesh grit, heated in air at 600° F for 5 minutes		.67			.44	
5	347 stainless steel	Same as specimen 4 but with 0.014-inch Rokide A coating		.27			.74	
6	347 stainless steel	Sandblasted with 100 mesh grit, 0.014-inch Rokide A coating (no thermal treatment)		.27			.74	
7	2024-T3 aluminum alloy	Sandblasted with 100 mesh grit, 0.013-inch Rokide A coating		.32			.75	
8	2024T-3 aluminum alloy	2 coats zinc chromate primer, 4 coats Ditzler mixing white lacquer (DMA 511)	.23	.21			.86	
9	AZ31B magnesium alloy	Same as specimen 8	.23				.78	
10	AZ31B magnesium alloy	2 coats zinc chromate primer, 4 coats Ditzler strong black lacquer (DMA 358)	.97	.92			.74	
11	Beryllium copper	Buffed-vapor deposited aluminum and silicon monoxide films	.21	.19			.16	
12	Enameled copper wire (Goddard sensor)	None	.63	.69			.69	
13	Enameled copper wire (Goddard sensor)	1 coat zinc chromate primer, 1 coat Sherwin-Williams flat black enamel F65B2		.94			.81	
[a]14	304 stainless steel (substrate of Lewis sensor)	Oxide salt bath	.87	.87		0.31	.29	
15	Beryllium copper	1 coat zinc chromate primer, 2 coats Sherwin-Williams flat black enamel F65B2	.96	.94			.83	
16	AZ31B magnesium alloy	0.014-inch silicone rubber compound (GE RTV-40)		.32			.80	
17	2024T-3 aluminum alloy	Sandblasted with 1F silicon carbide - 18 inches from specimen	.55	.67			.27	

[a]This process consists of immersing the steel surfaces in a boiling bath of Dulite 3-0 salt to produce a black oxide finish. The specimen is particularly interesting because of the relatively low emissivity of the surface which is black at the visible wavelengths.

L-1737

78

TABLE VI.- SOLAR ABSORPTIVITIES OF MATERIALS AND COATINGS

Description of specimen	a_s
2024-T3 aluminum alloy as received, cleaned with methyl ethyl ketone	0.42
2024-T3 aluminum alloy, 1 coat zinc chromate primer, 2 coats flat black enamel (Sherwin-Williams F65B2)	0.96
2024-T3 aluminum alloy, 1 coat of aluminum paint (formula A-10,NRL)	0.44
2024-T3 aluminum alloy with 10 minutes caustic etch at 160° F	0.16
Magnesium alloy, 3 coats titanium dioxide white paint (MSFC)	0.16
Beryllium copper as received, cleaned with methyl ethyl ketone	0.37

L-1737

TABLE VII.- COMPOSITIONS OF SOME PAINTS CONSIDERED FOR EXPLORER XIII[1]

Paint	Pigment by weight, percent	Vehicle by weight, percent	Pigment		Vehicle	
			Composition	Percent by weight	Composition	Percent by weight
Strong black lacquer (IMA 358)	1.1	28.0	Carbon black	100	Acrylic polymer Chemical plasticizer Nitrocellulose	69 25 6
Mixing white lacquer (IMA 311)	10.6	26.7	Titanium dioxide	100	Acrylic polymer Chemical plasticizer Nitrocellulose	69 25 6
Flat black enamel (F65B2)	31.0	69.0	Silicates Calcium carbonate Carbon black	84 8 8	Linseed alkyd phenolic resin Mineral spirits Driers	31 67 2
Lusterless white enamel (F93-WC9)	38.0	62.0	Titanium dioxide Magnesium silicate	52 48	Styrenated soya-tung alkyd Xylene solvent Driers	31 67 2

[1]All values given in this table were supplied by the manufacturers.

Pressure cell

Inner heat shield

Fourth-stage rocket motor

Pressure cell
mounting bracket

Enlarged typical cross section showing pressure cell mountings

Pressurized tube
detectors (Langley)

Grid detectors
(Lewis)

Wire detector
(Goddard)

Terminal block
assembly

Antenna, folded

Stainless steel
nose cone

Phantom outline of
telemetry package

Solar cells

22.892 (max. diam.)

Cadmium-sulfide
detector (Goddard)

Sta.
76.42

Sta.
0

Sounding boards
(Langley)

✳ Denotes location of
piezoelectric impact
detectors.

Figure 1.- General arrangement of Explorer XIII micrometeoroid satellite.

L-1737

L-1737

Figure 2.- Satellite nose cone.   L-61-2146
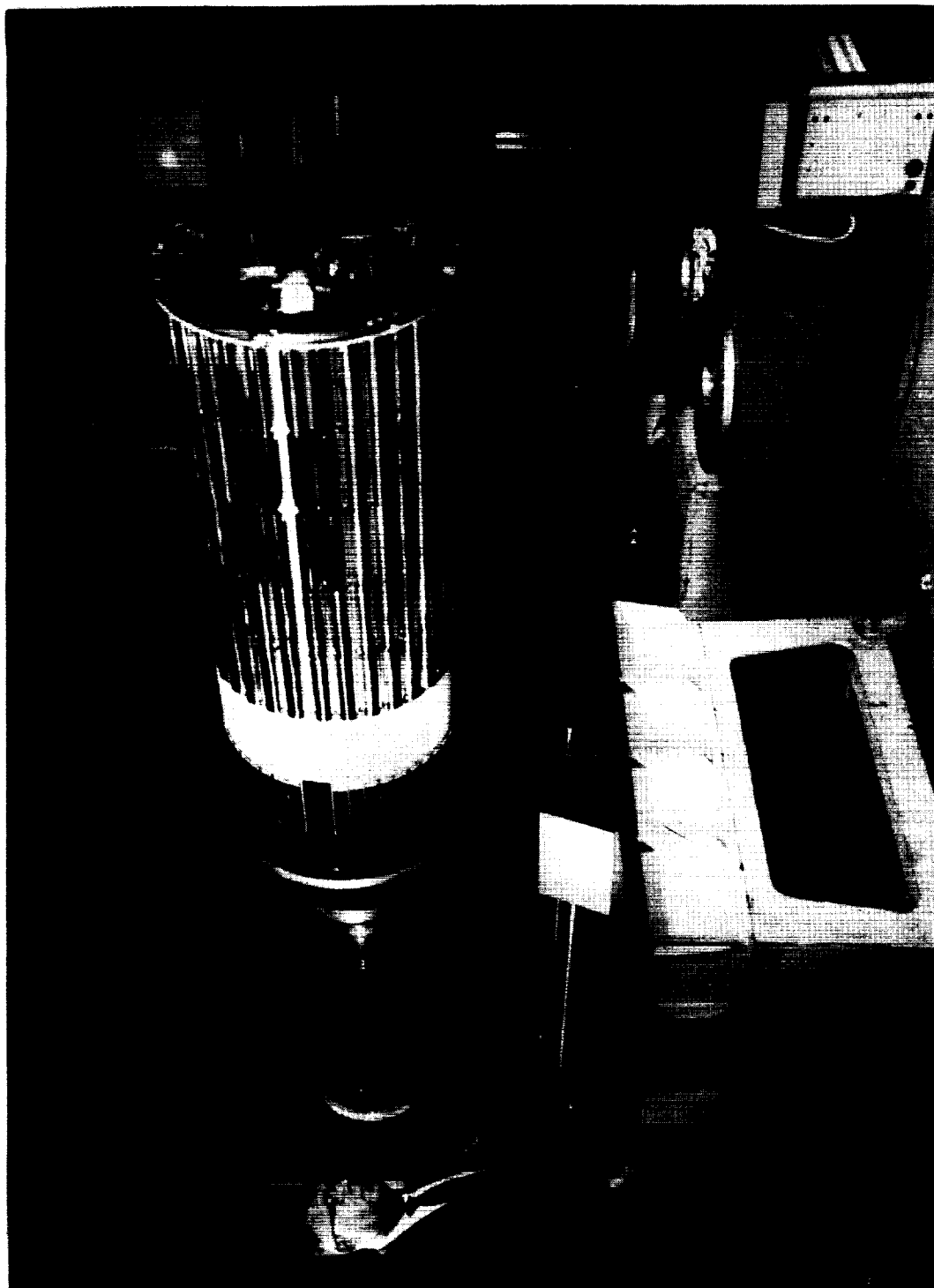
Figure 3.- Satellite with nose cone removed.   L-61-2260

L-1737
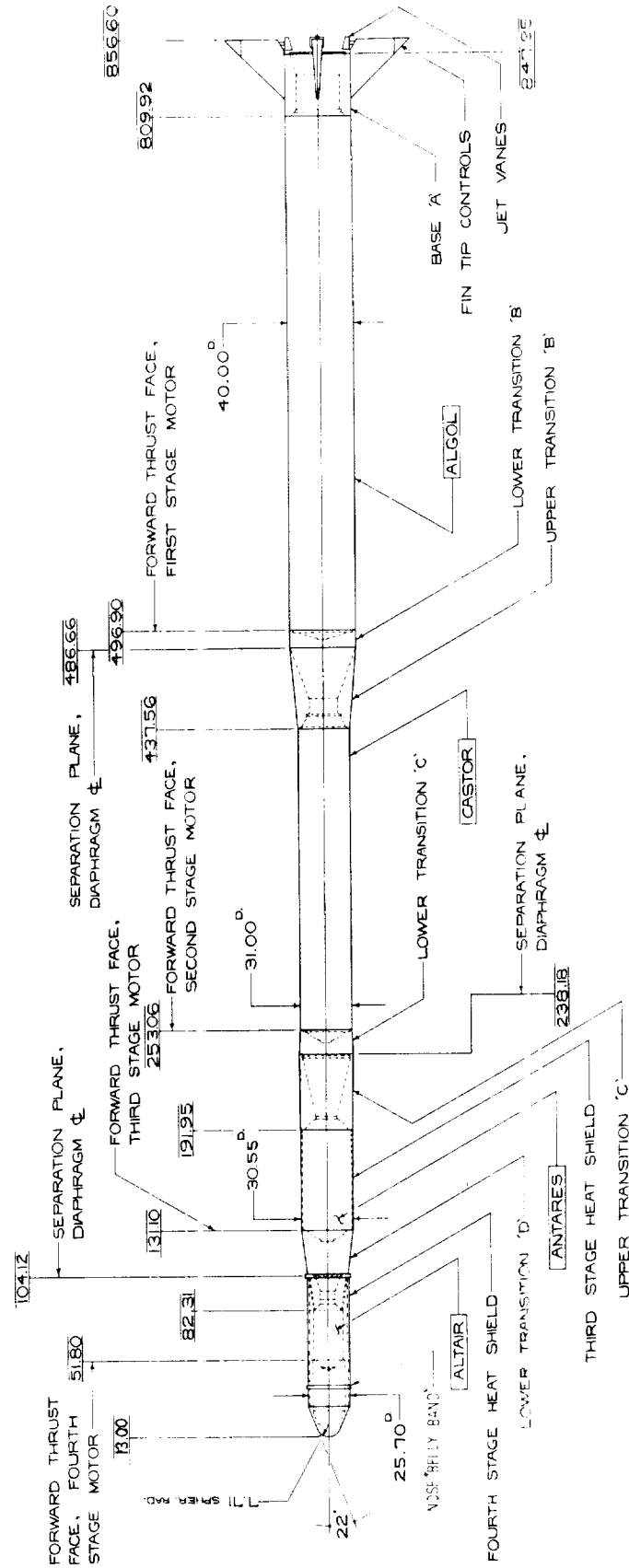
Figure 4.- General arrangement of Scout launch vehicle.
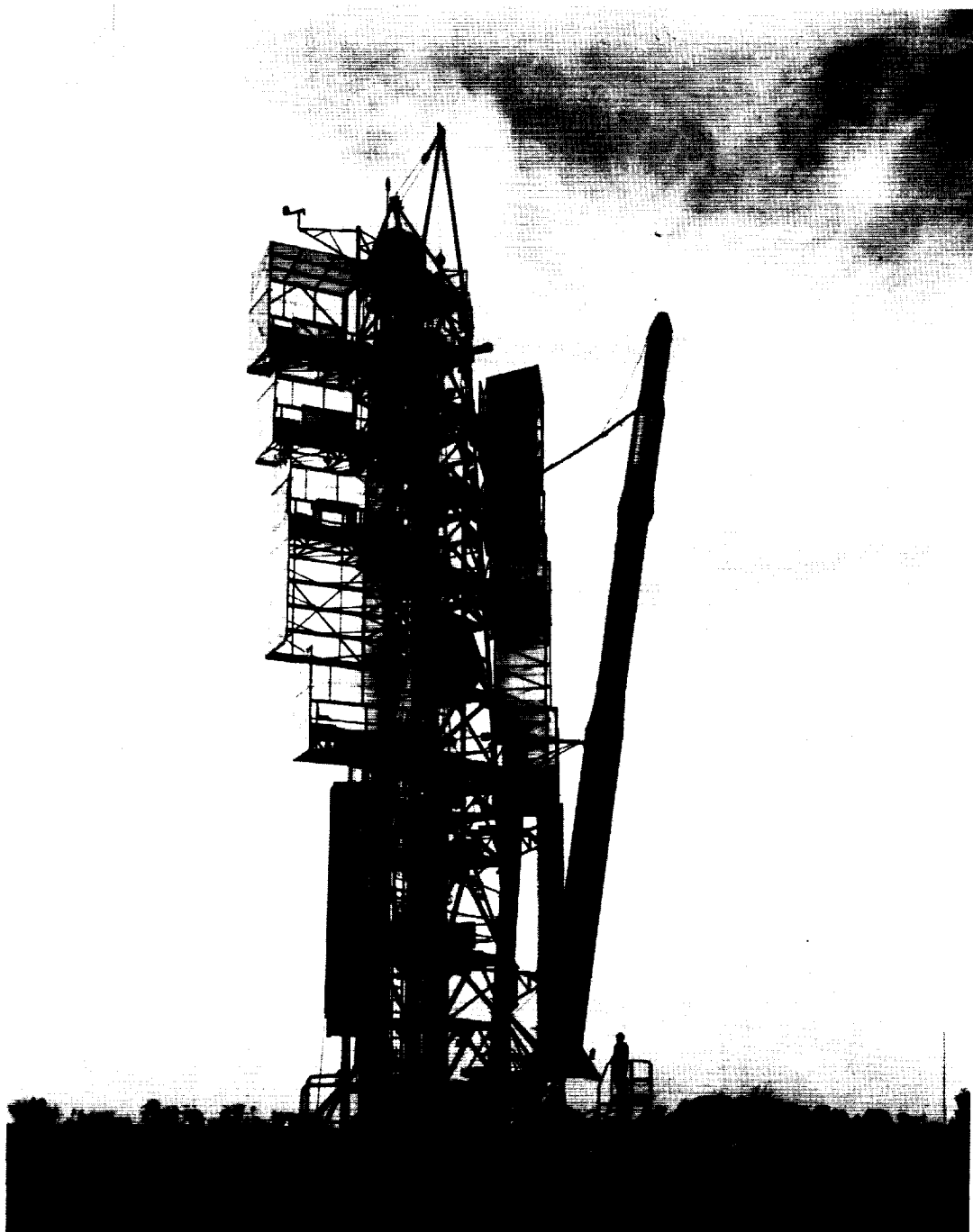
Figure 5.- Scout launch vehicle and launch tower.   L-61-3853
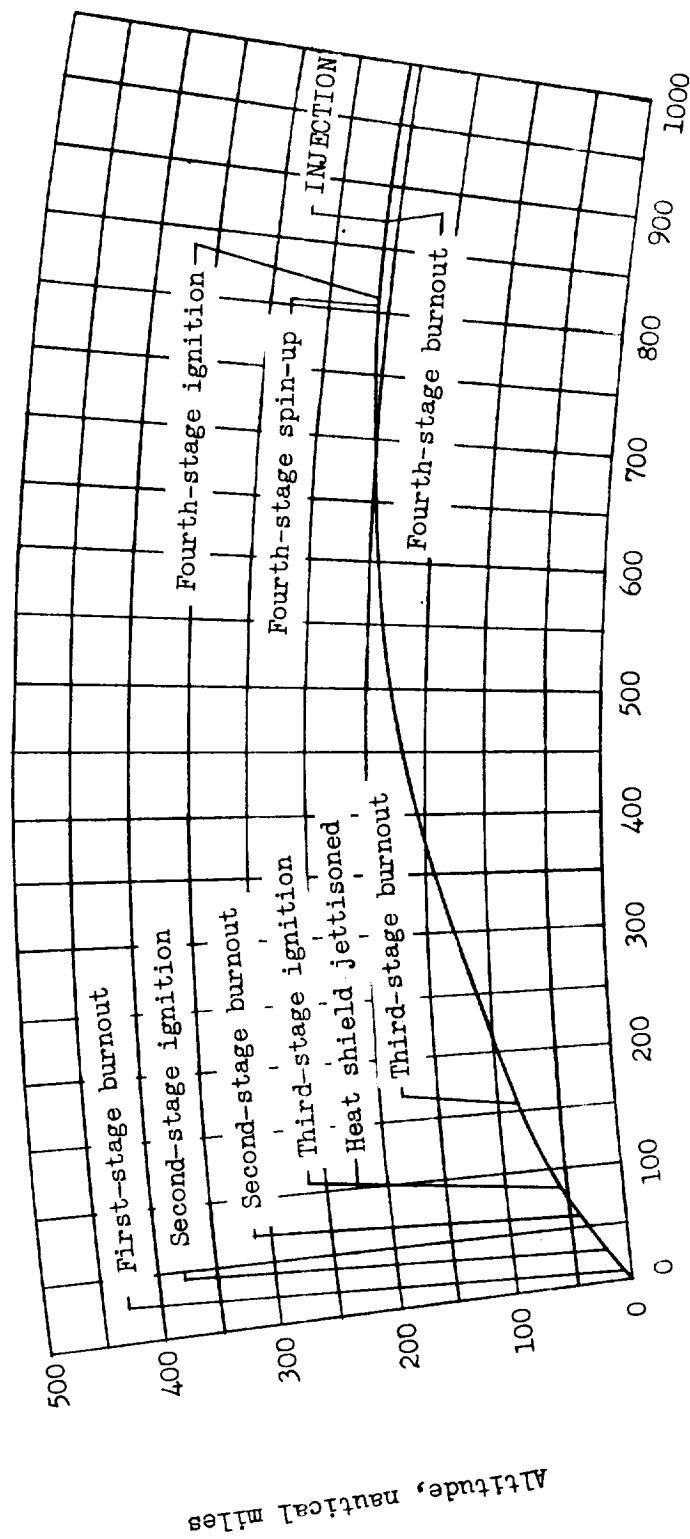
Figure 6.- Ascent trajectory profile.

86
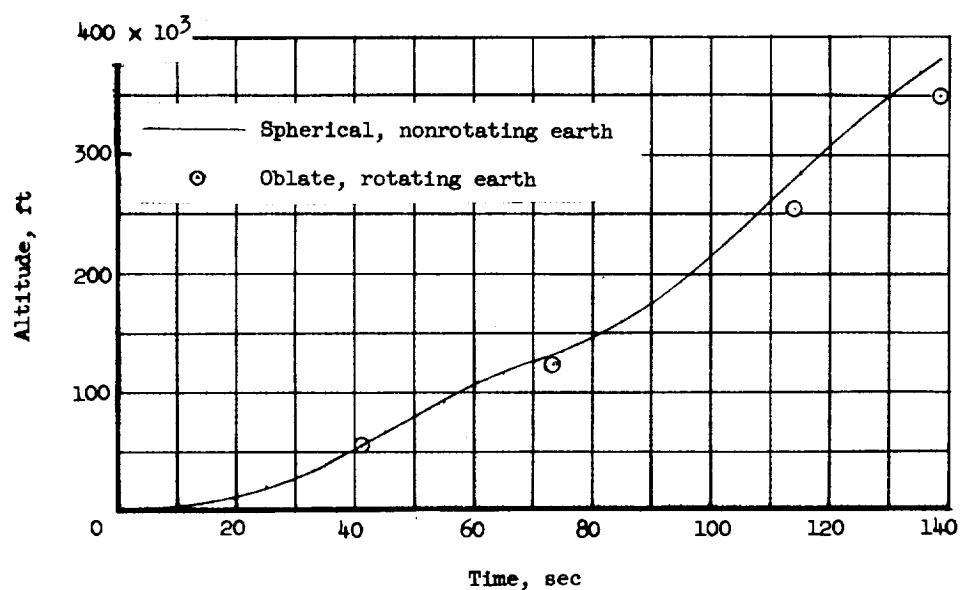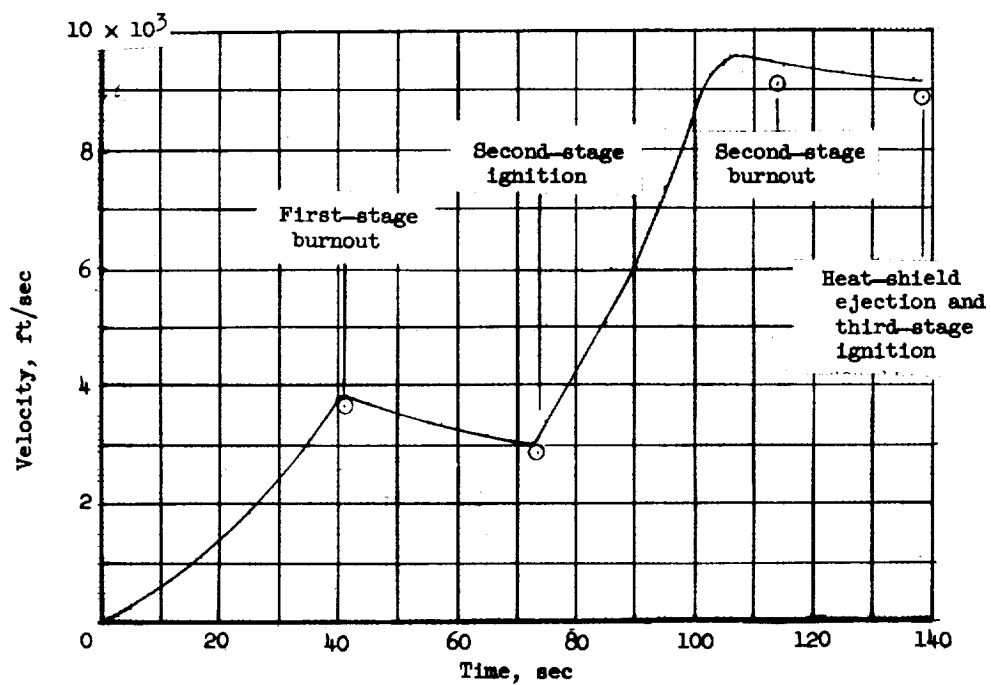
(a) Altitude.

(b) Velocity.

Figure 7.- Variation of altitude and velocity with time.

L-1737
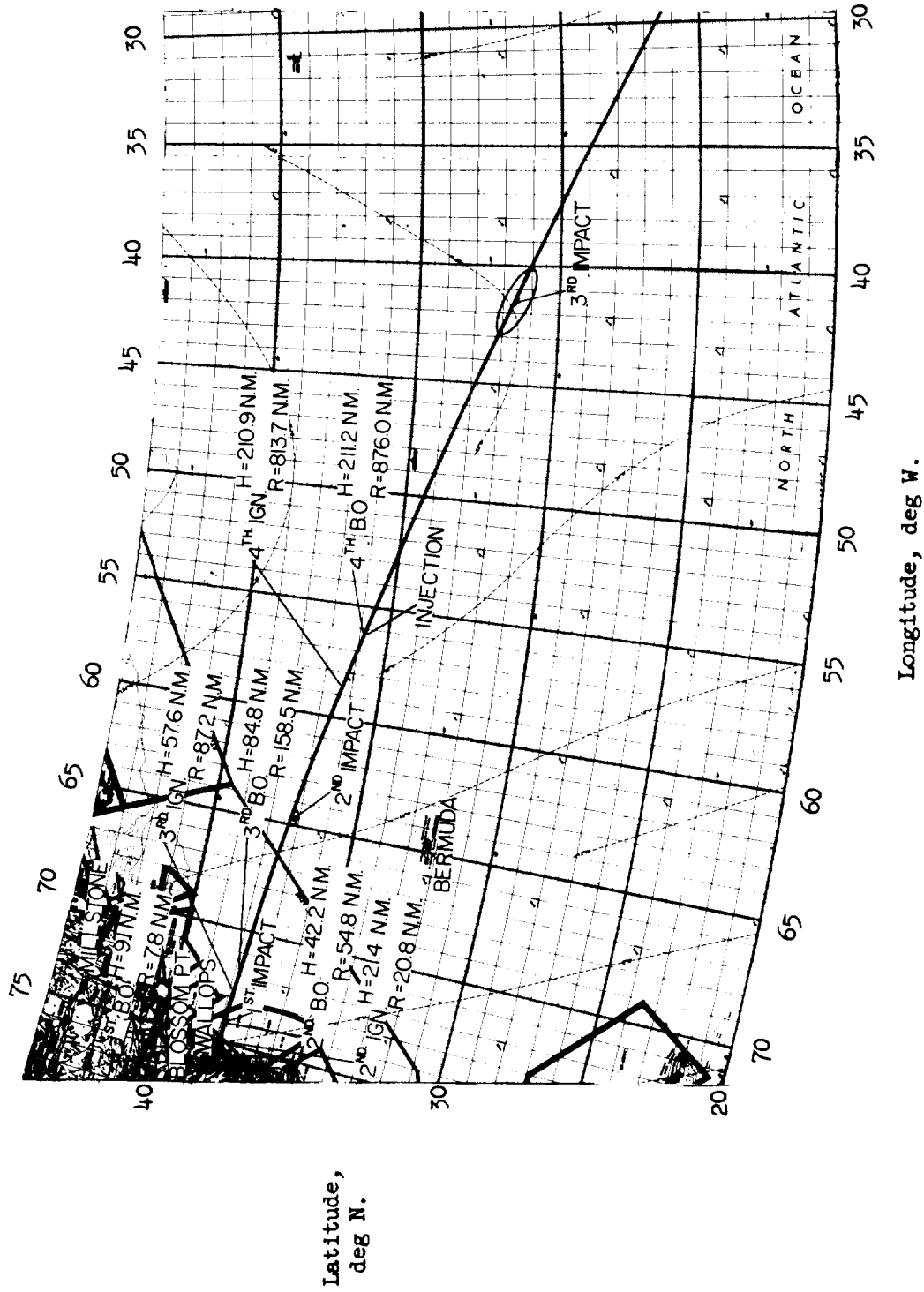
Figure 8.- Earth track during ascent.

Longitude, deg W.

Latitude, deg N.

88
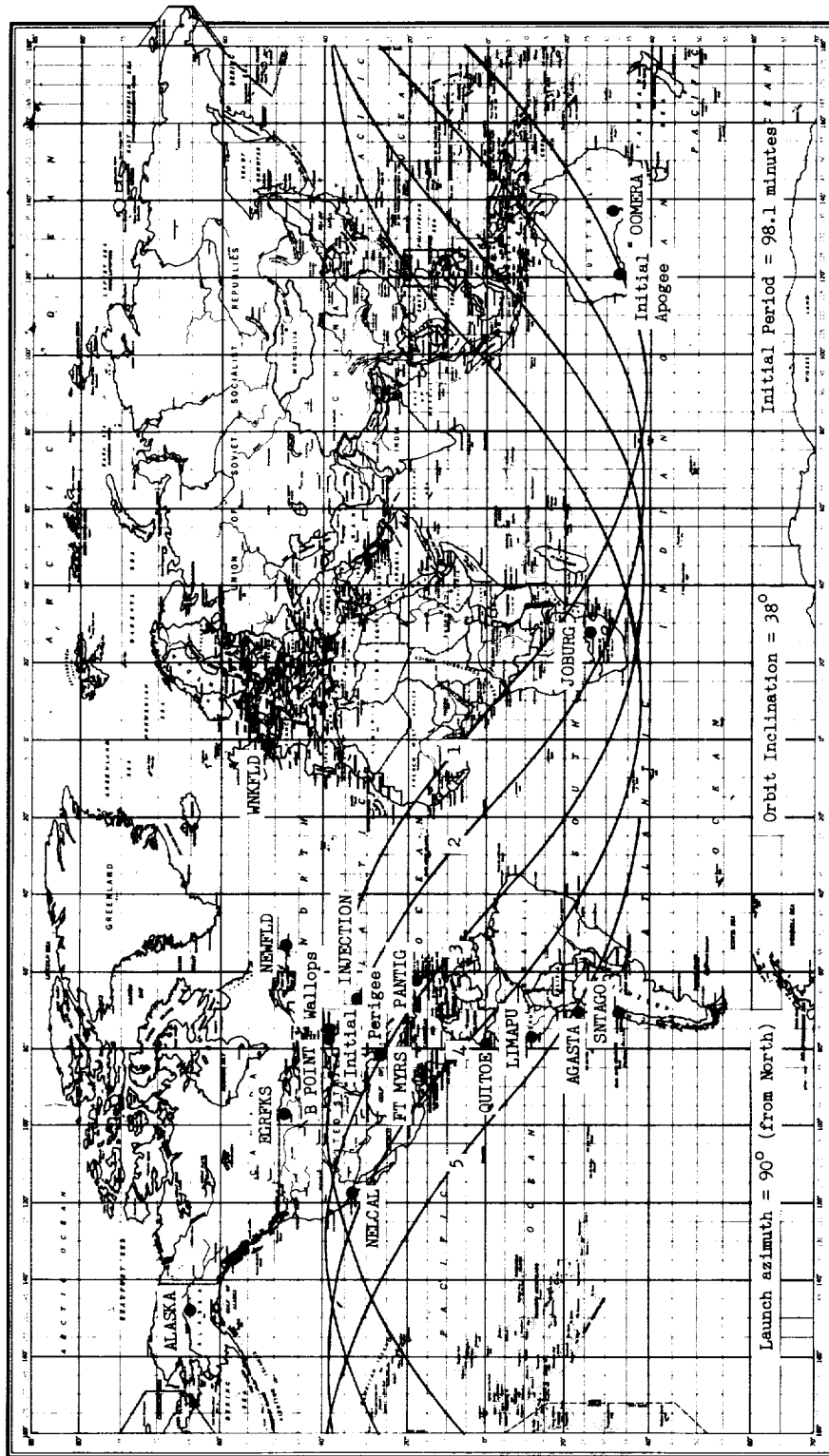
Figure 9.- Typical track of subsatellite point.

L-1737

L-1757

.05-inch laminated phenolic

.50-inch Fiberglas honeycomb

.05-inch laminated phenolic

Enlarged cross section of cover
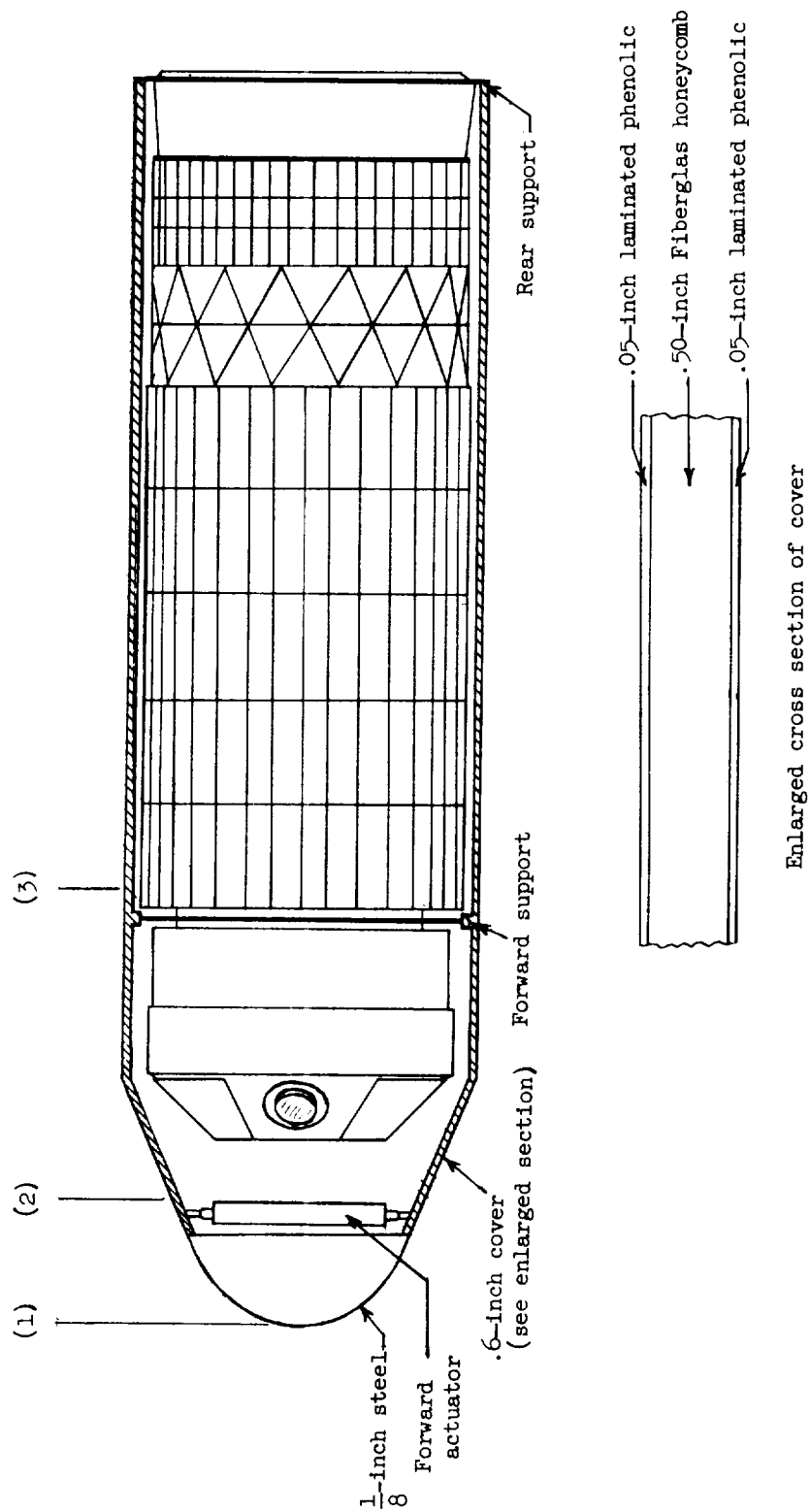
Figure 10.- Satellite enclosed in heat shield. Numbers in parenthesis indicate points at which temperature time histories were calculated.
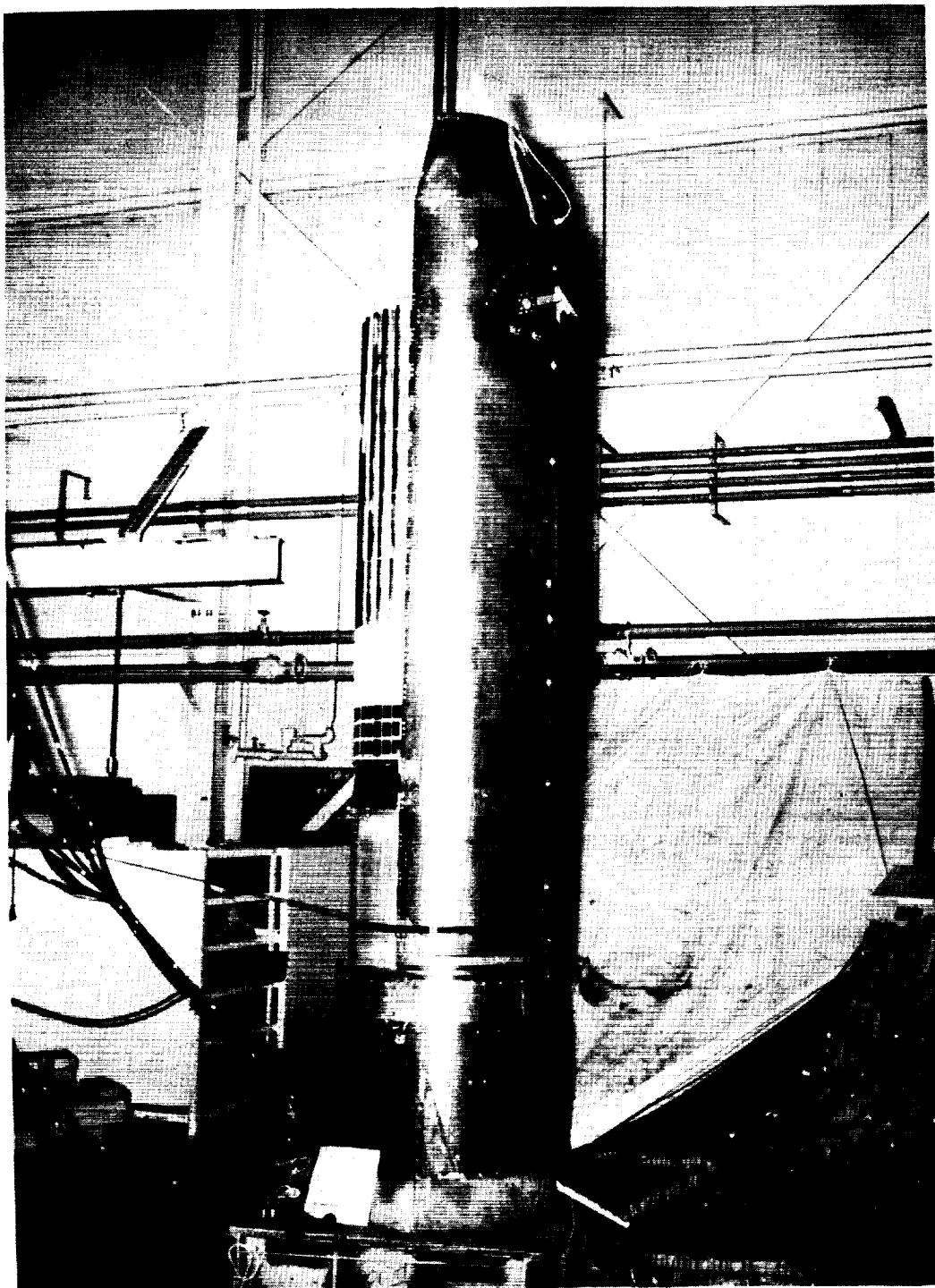
L-1737

L-62-17

Figure 11.- Satellite enclosed in half of heat shield.

L-1737
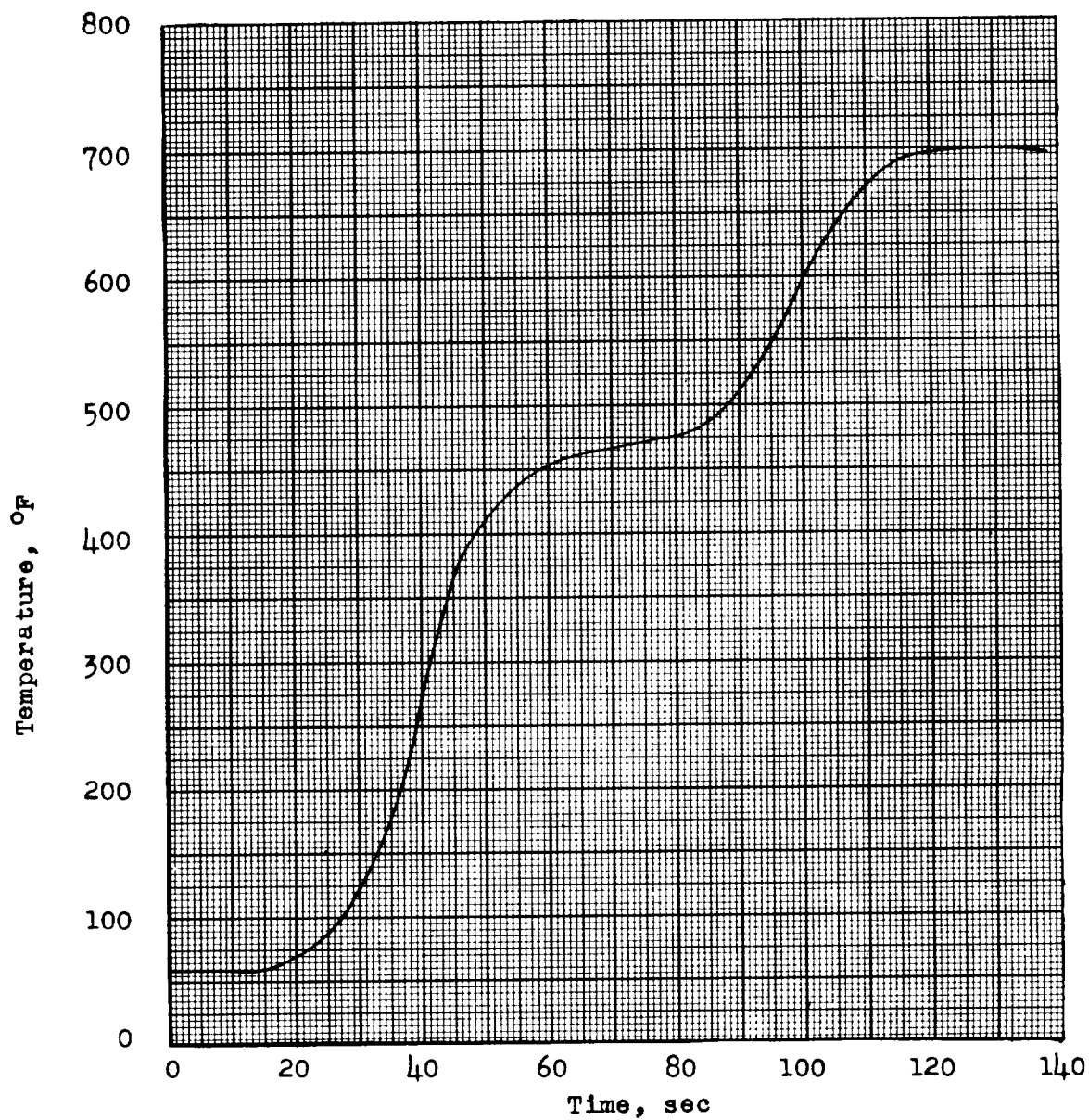
Figure 12.- Temperature time history at station (1) during ascent.
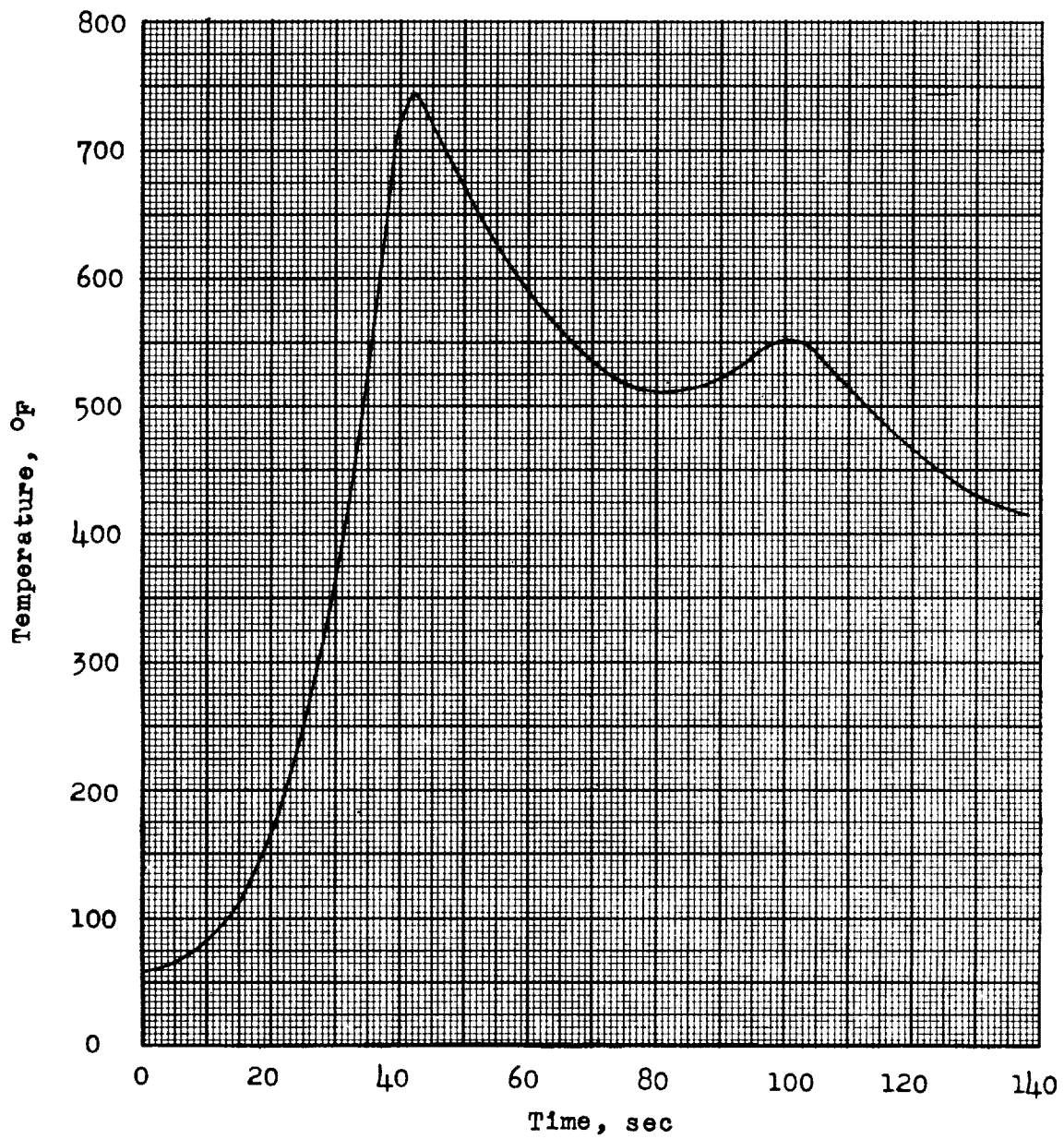
Figure 13.- Temperature time history at outside wall of station (2) during ascent.
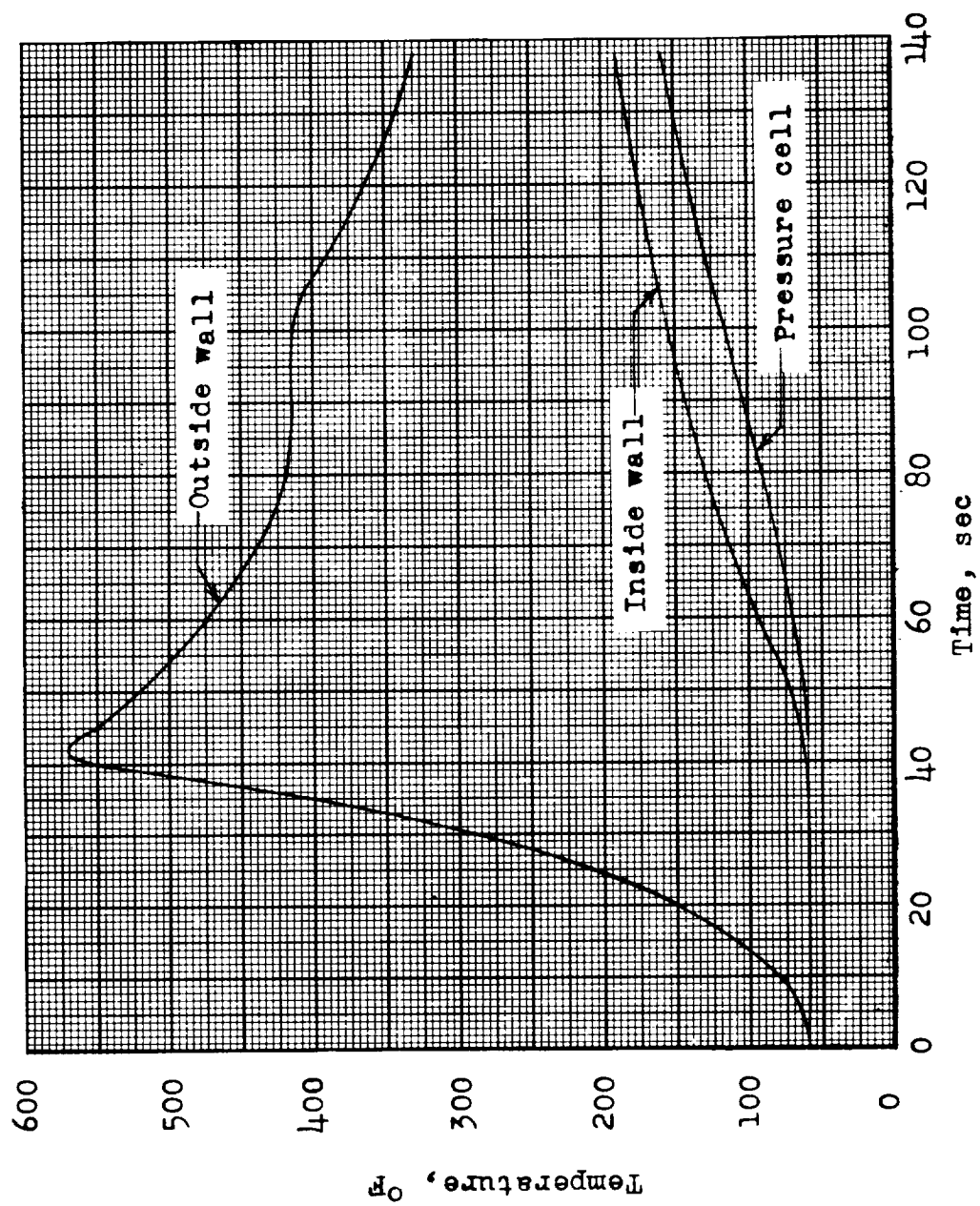
L-1737

L-1737

Figure 14.- Temperature time history at station (3) during ascent.
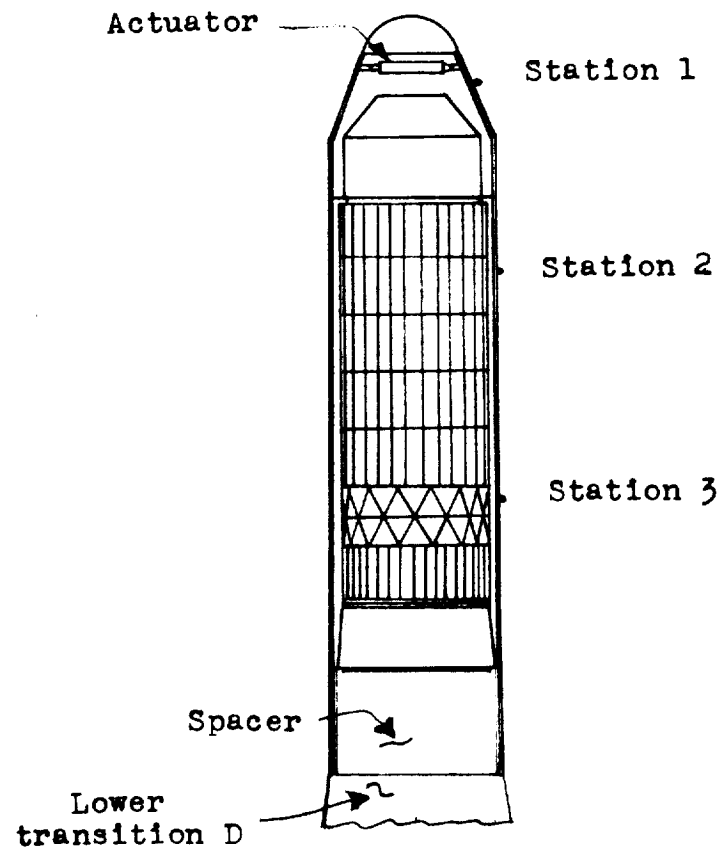
Figure 15.- Sketch showing test setup for prefiring simulation
of ascent heating.
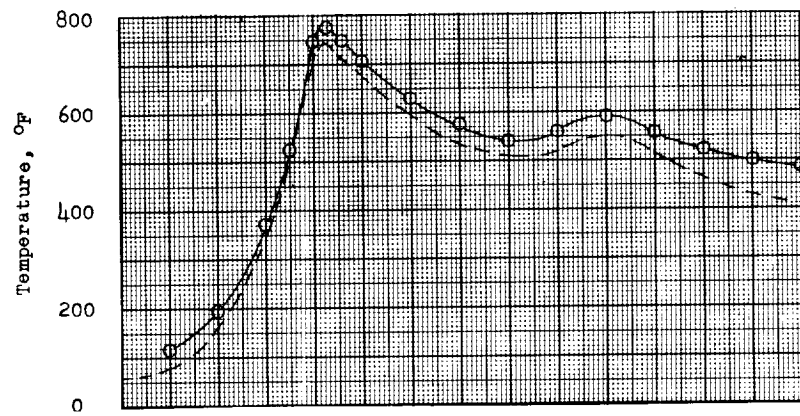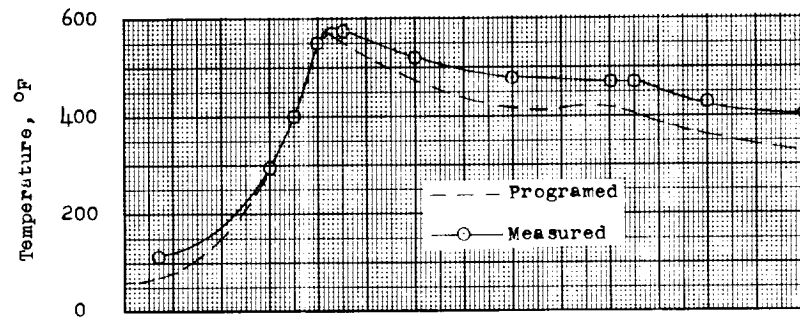
(a) Station 1.

(b) Station 2.
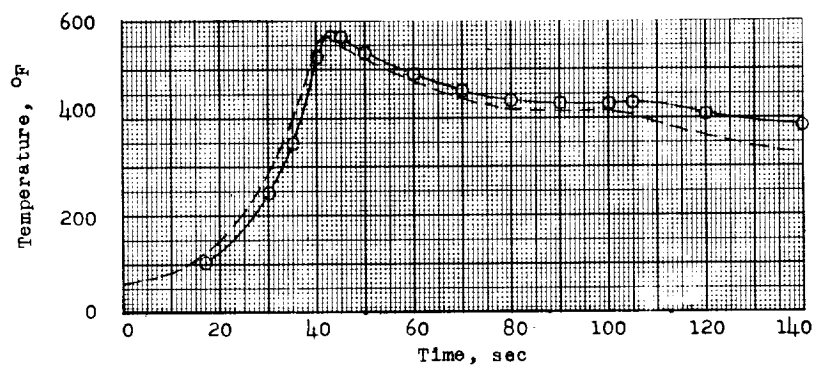
(c) Station 3.

Figure 16.- Comparison of programed and measured heat-shield
temperatures during simulated ascent heating test.
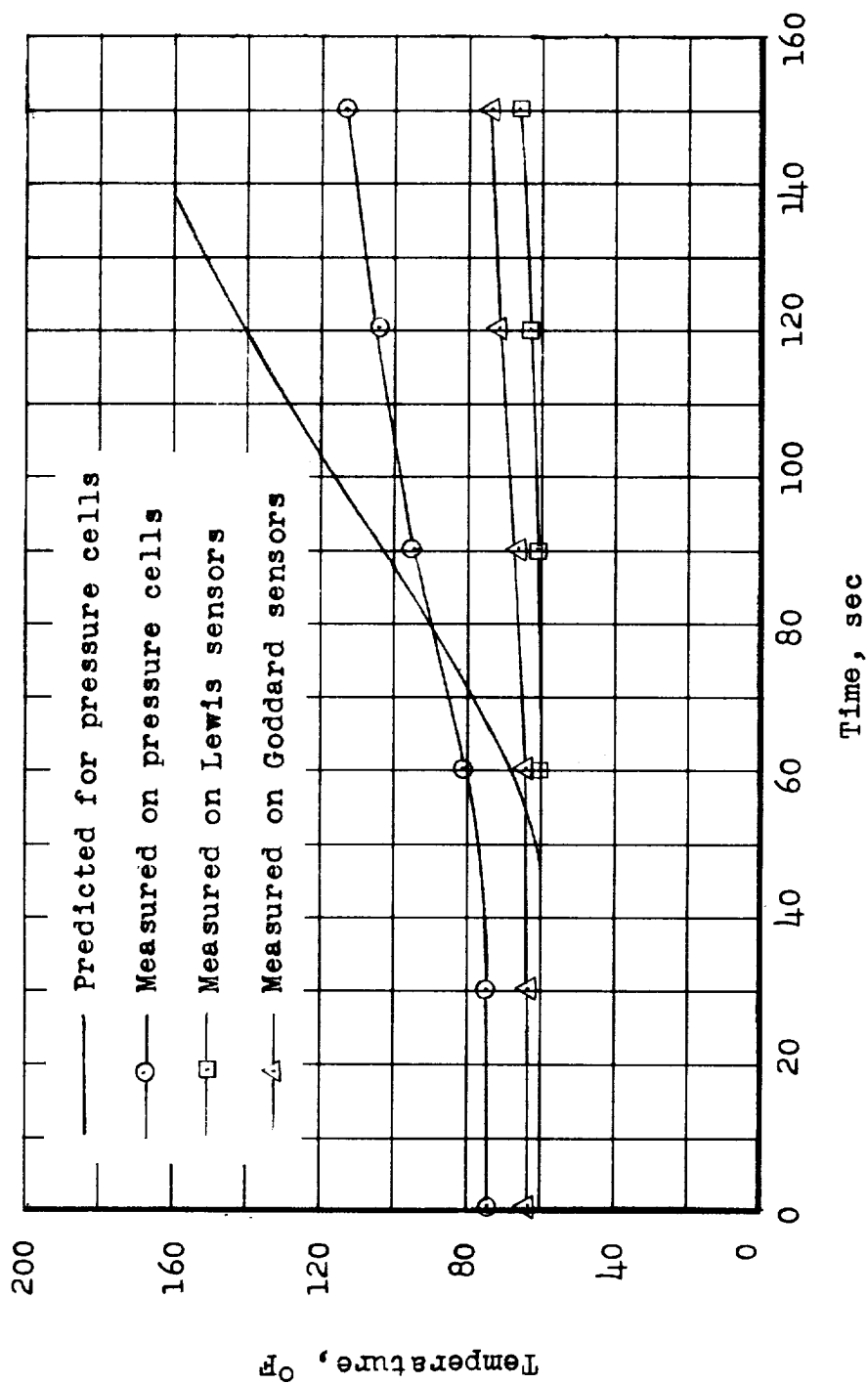
Figure 17.- Predicted and measured payload temperatures during simulated ascent heating test.

L-1737

L-1737
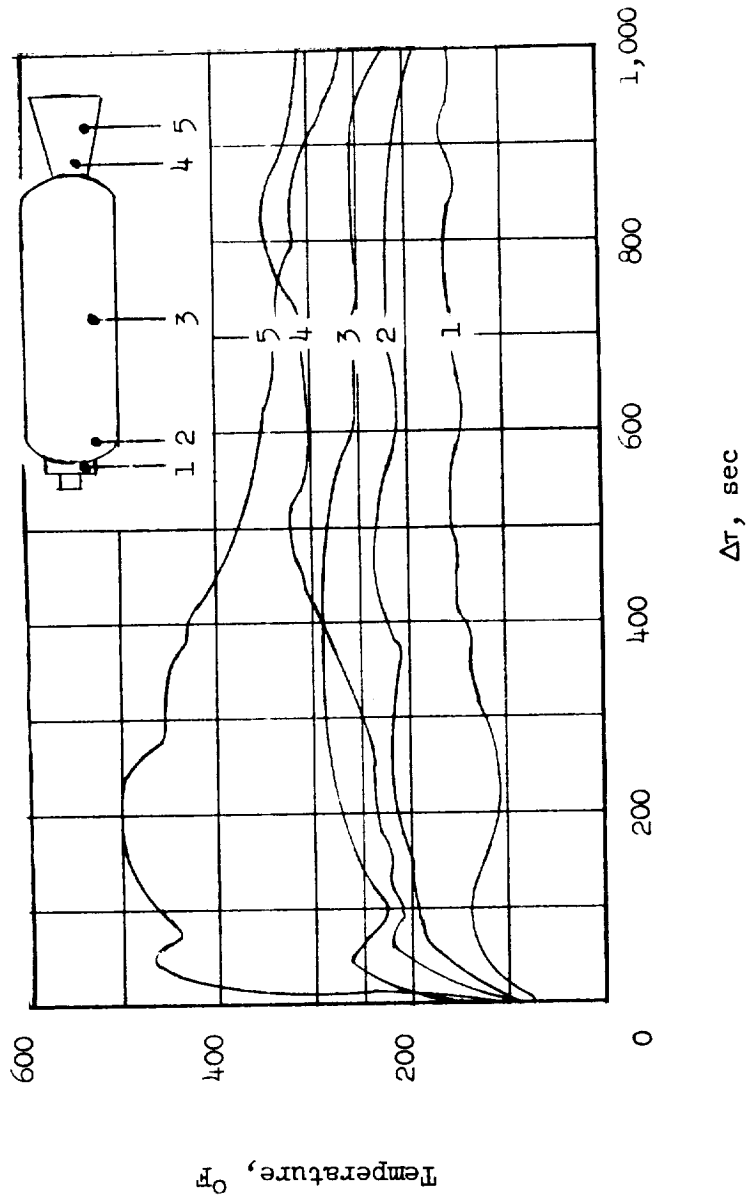
Figure 18.- Measured temperatures from static firing of ABL-X-248-A9 rocket motor.
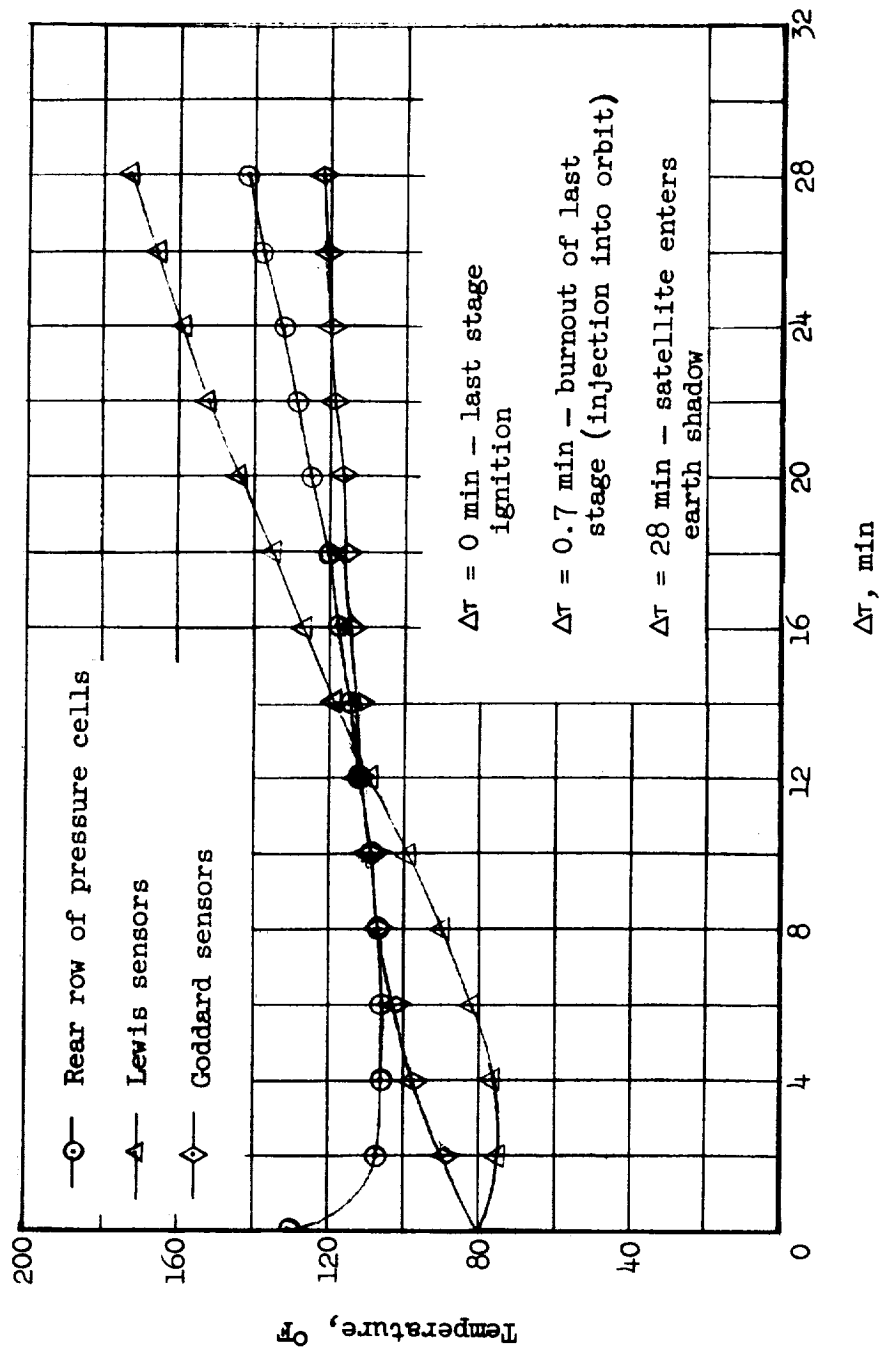
Figure 19.- Estimated satellite surface temperature due to last-stage rocket motor heating.

L-1737

L-1737
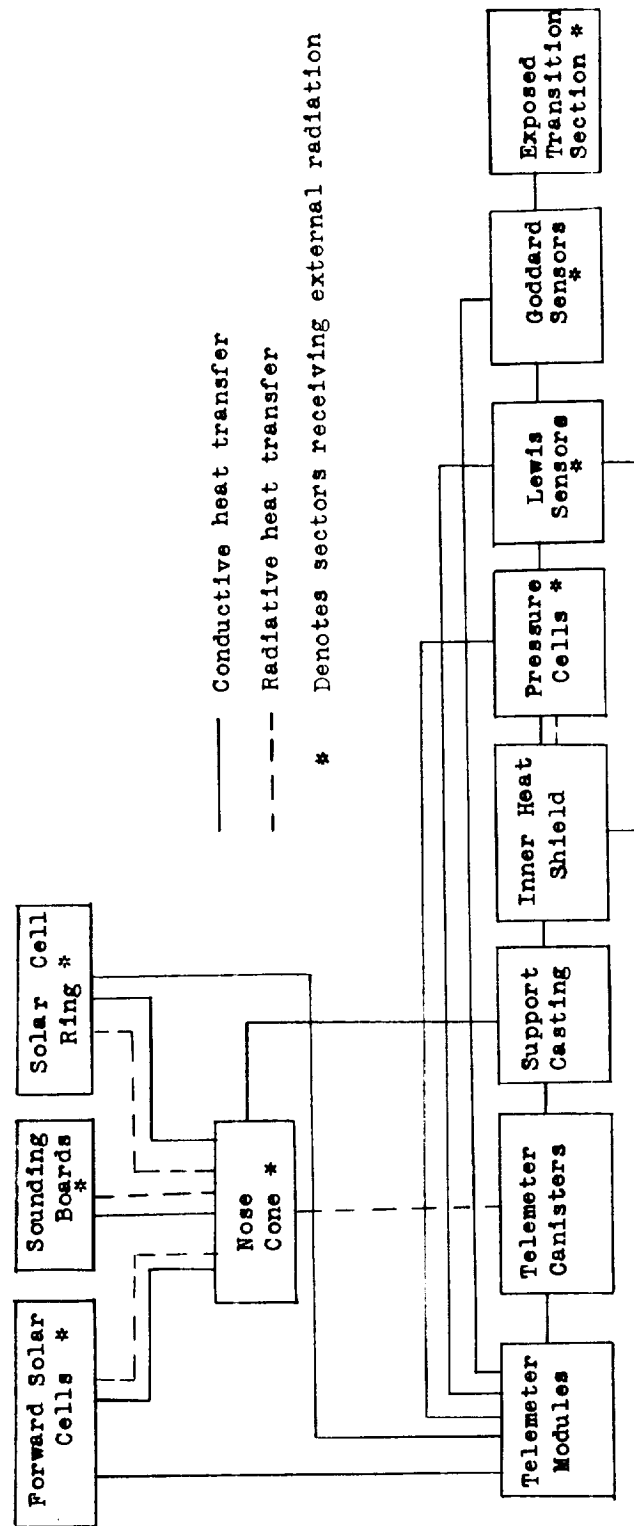
Figure 20.- Schematic diagram of heat-flow paths.
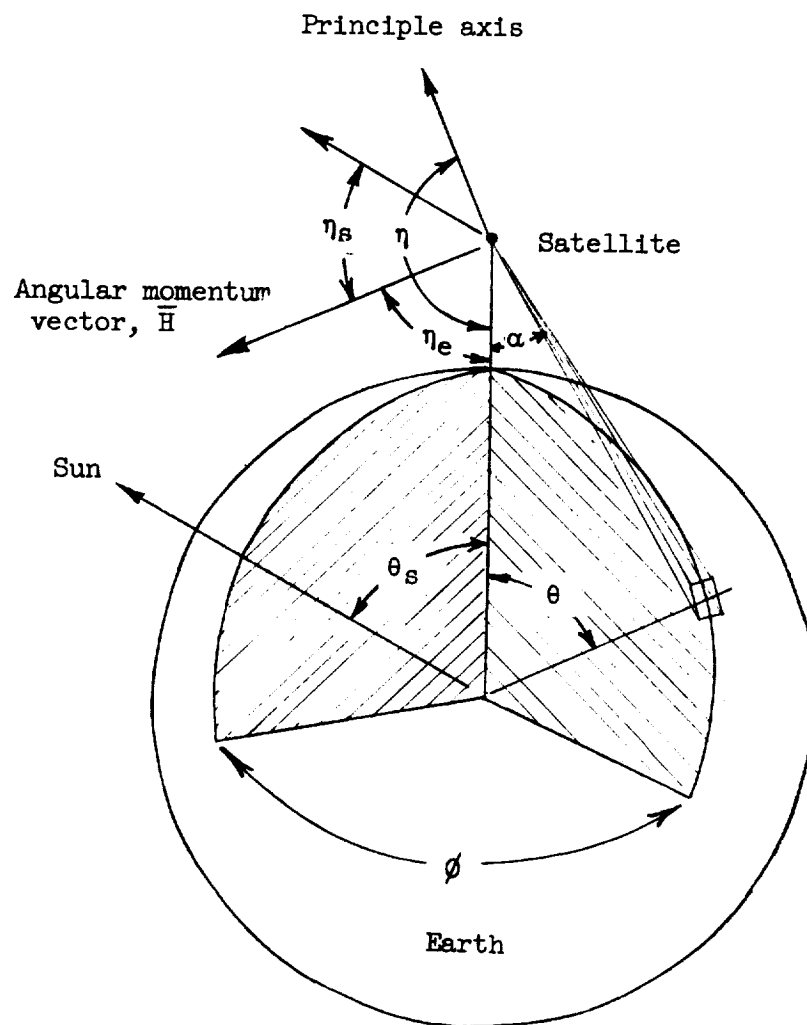
Figure 21.- Satellite orientation with respect to earth and sun.

L-1737
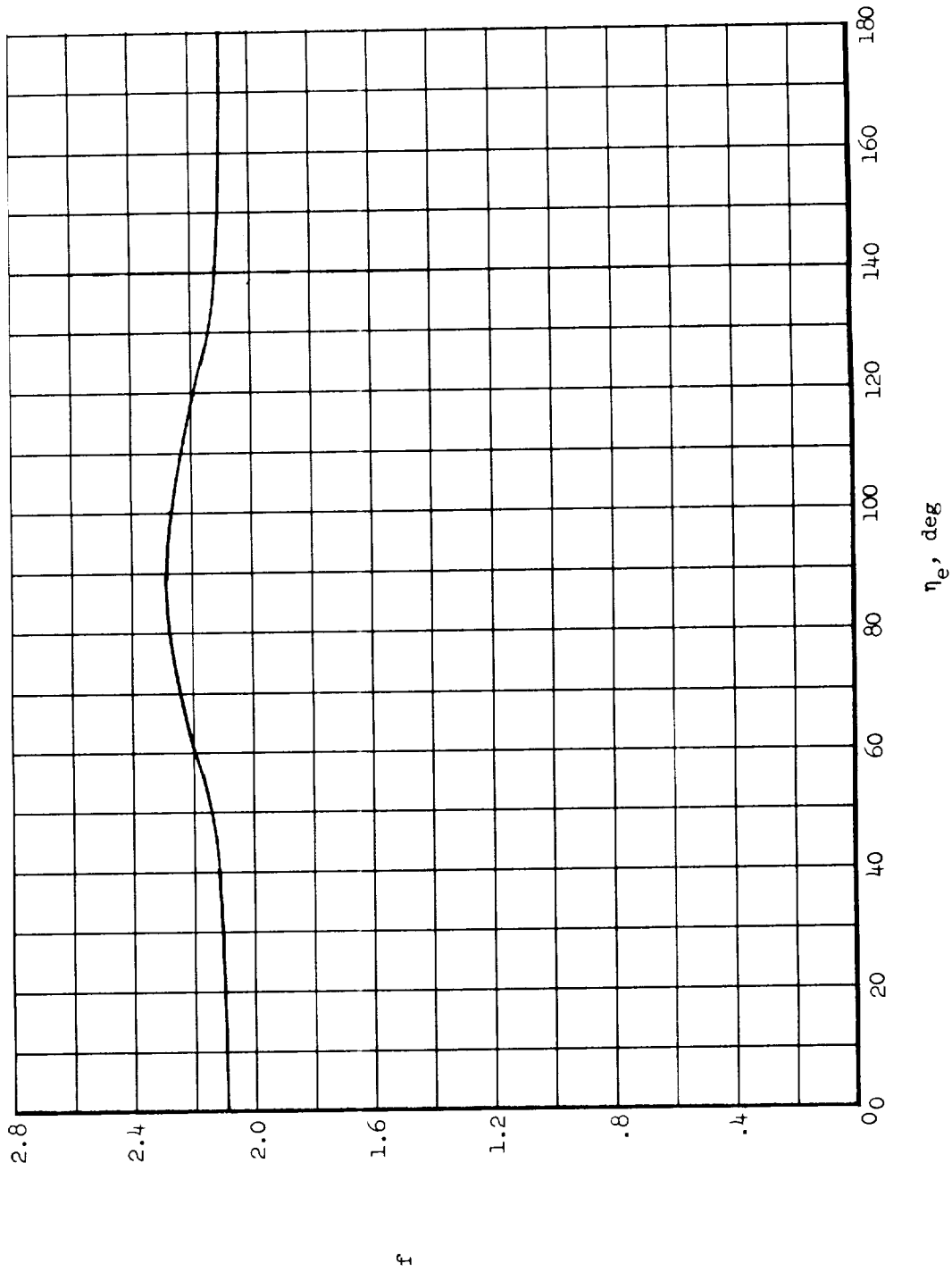
Figure 22.- Shape factor for a 45° cone as a function of orientation angle.
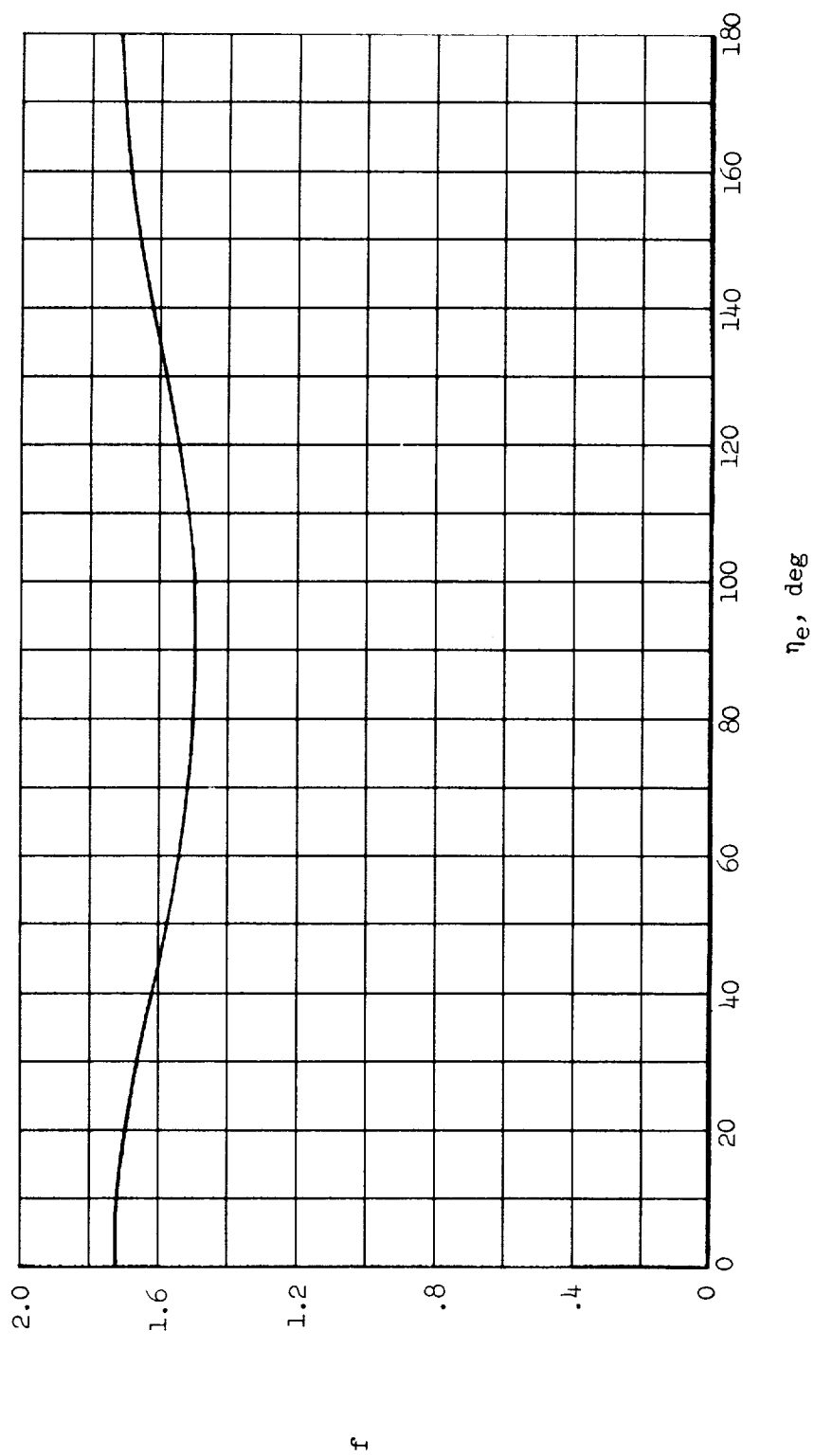
Figure 23.- Shape factor for a cylinder as a function of orientation angle.

L-1757

L-1737
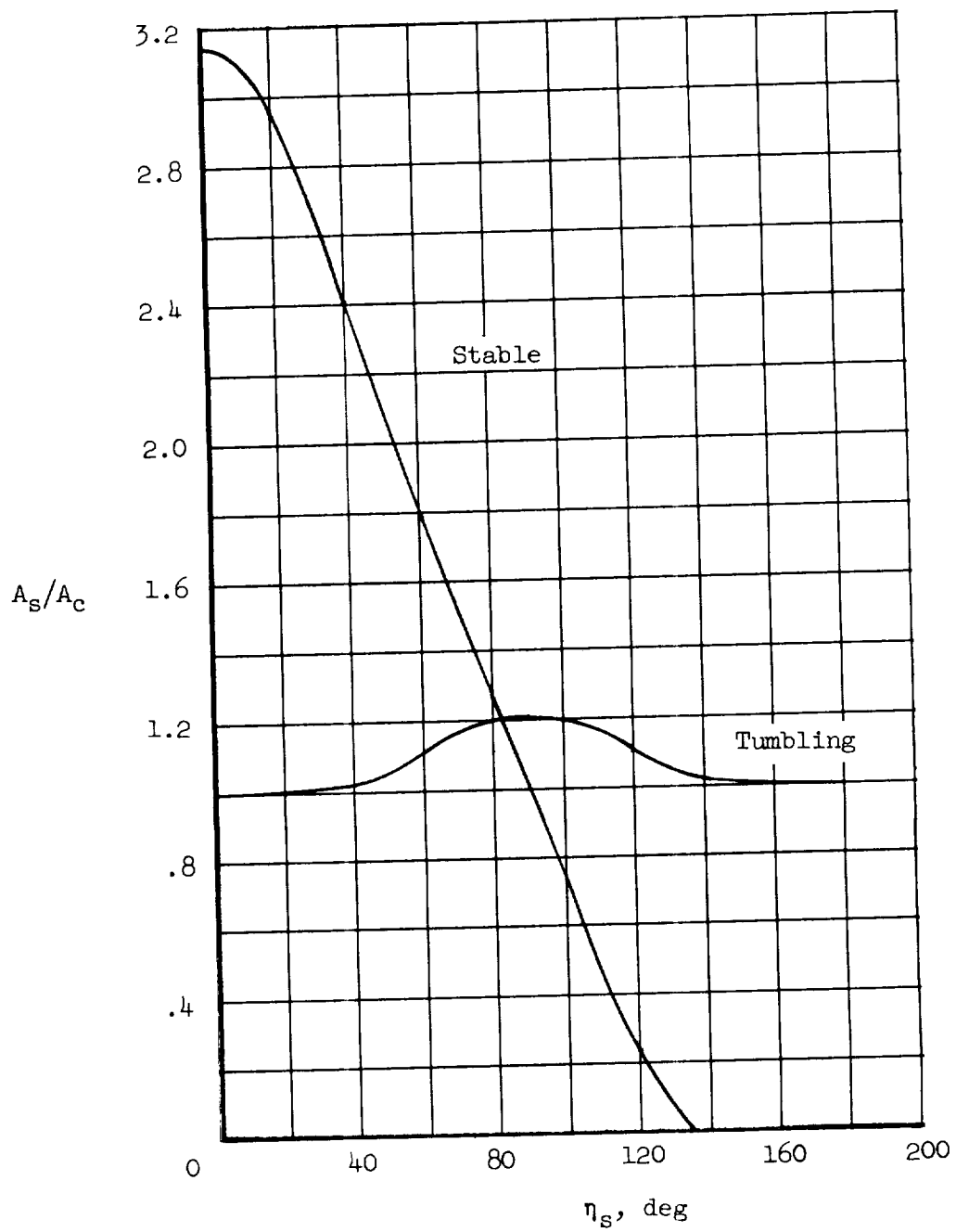
Figure 24.- Area distribution for a 45° cone as a function of orientation angle.
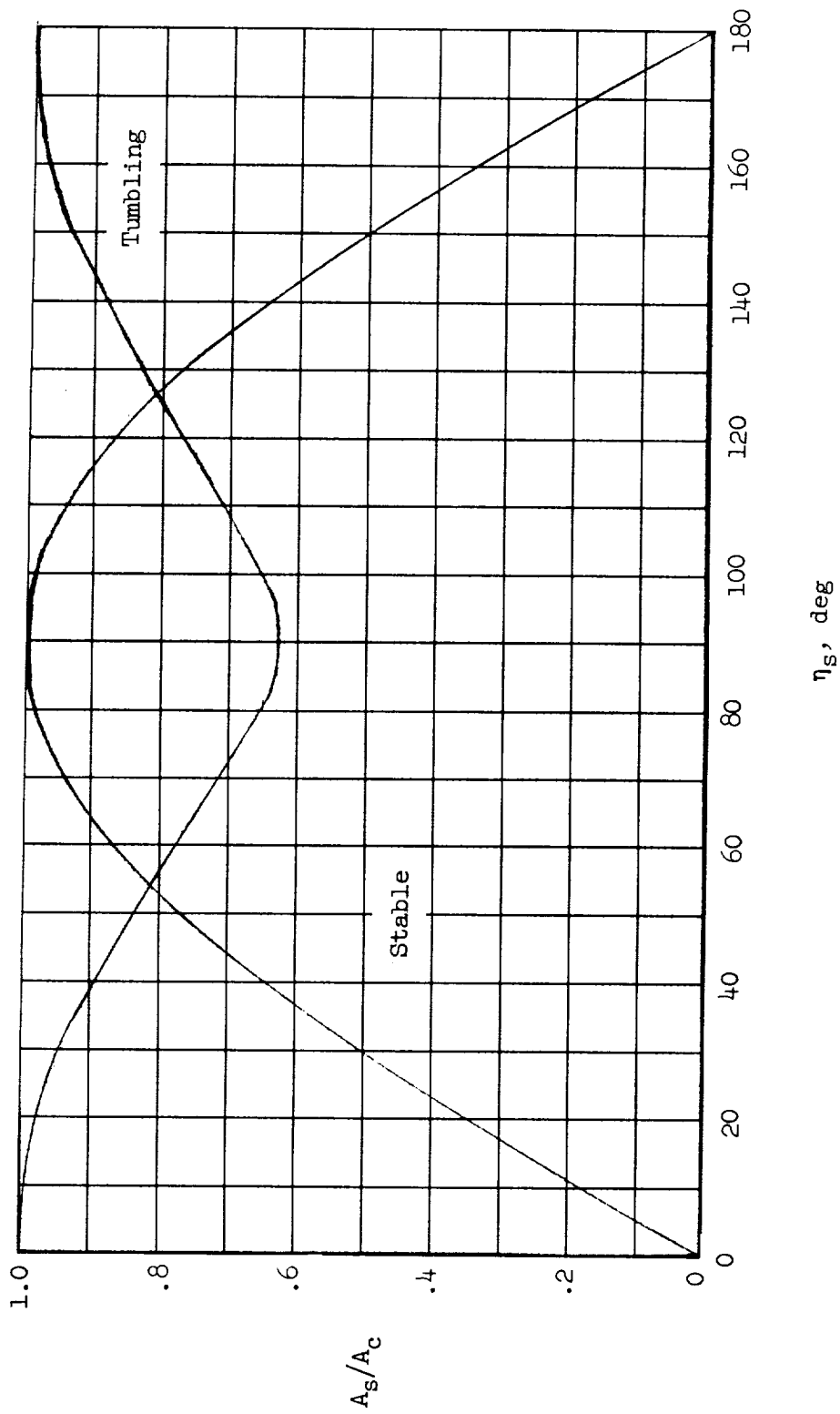
Figure 25.- Projected area of a cylinder as a function of orientation angle.

L-1737
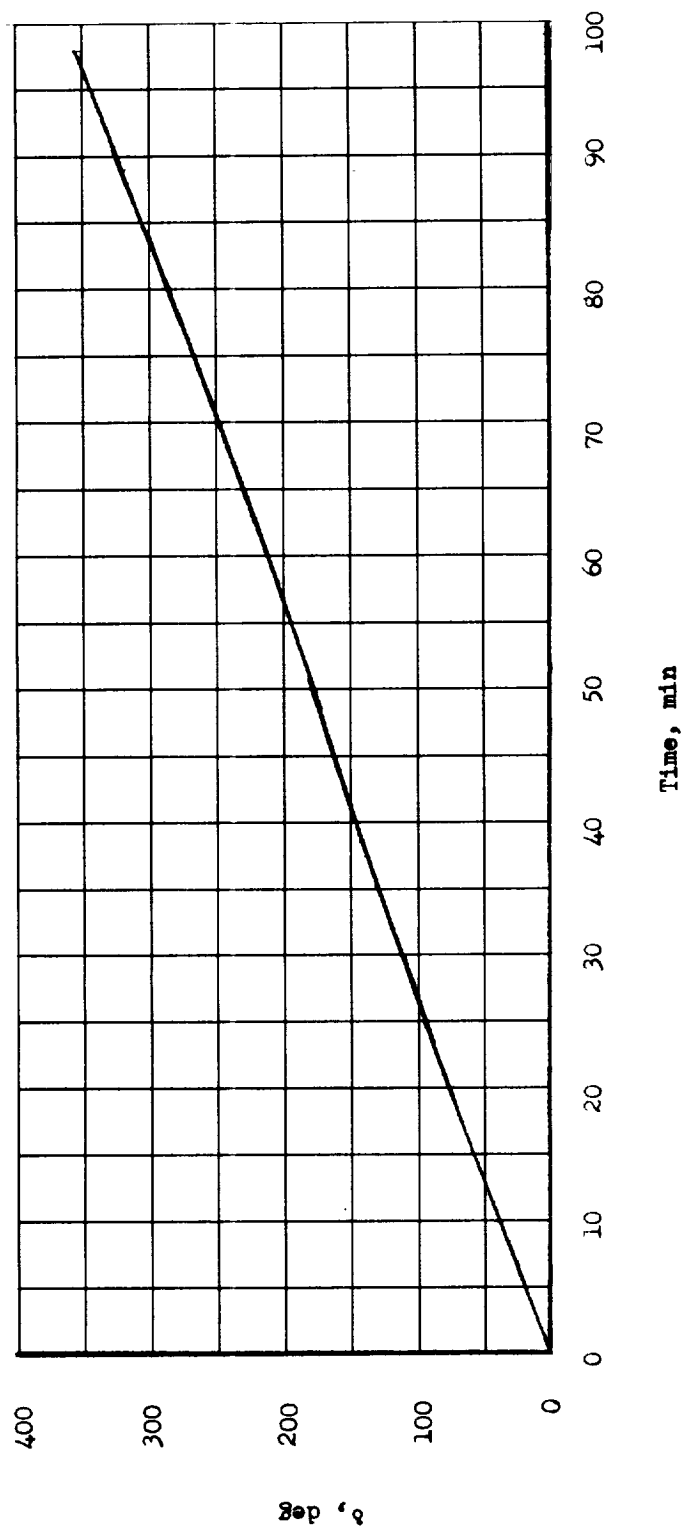
Figure 26.- Orbit angle as a function of time.
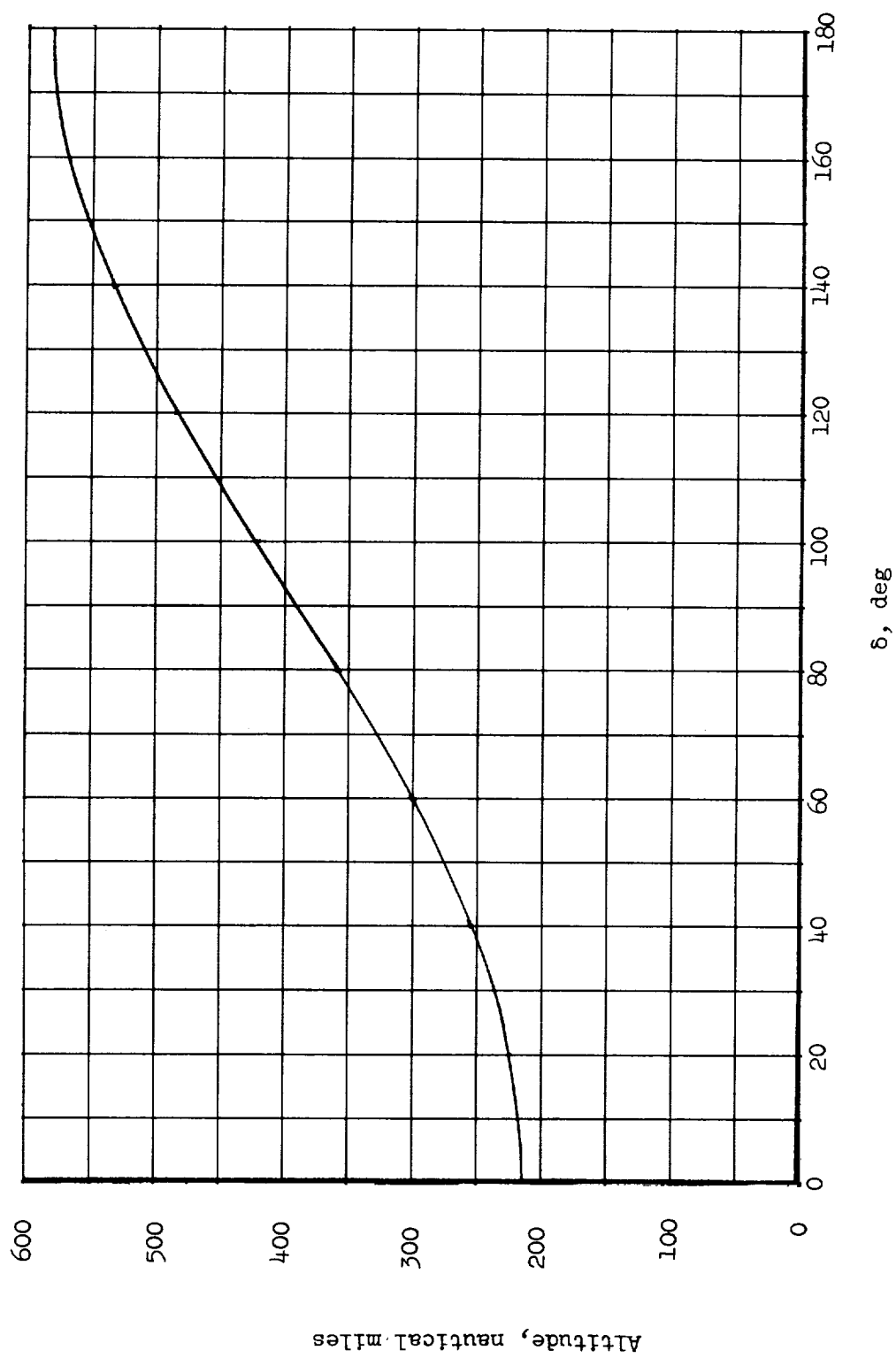
Figure 27.- Altitude as a function of orbit angle.

L-1737

L-1737

ε,deg	p
0	65.3
40	69.0
50	72.2
55	73.6
60	77.3
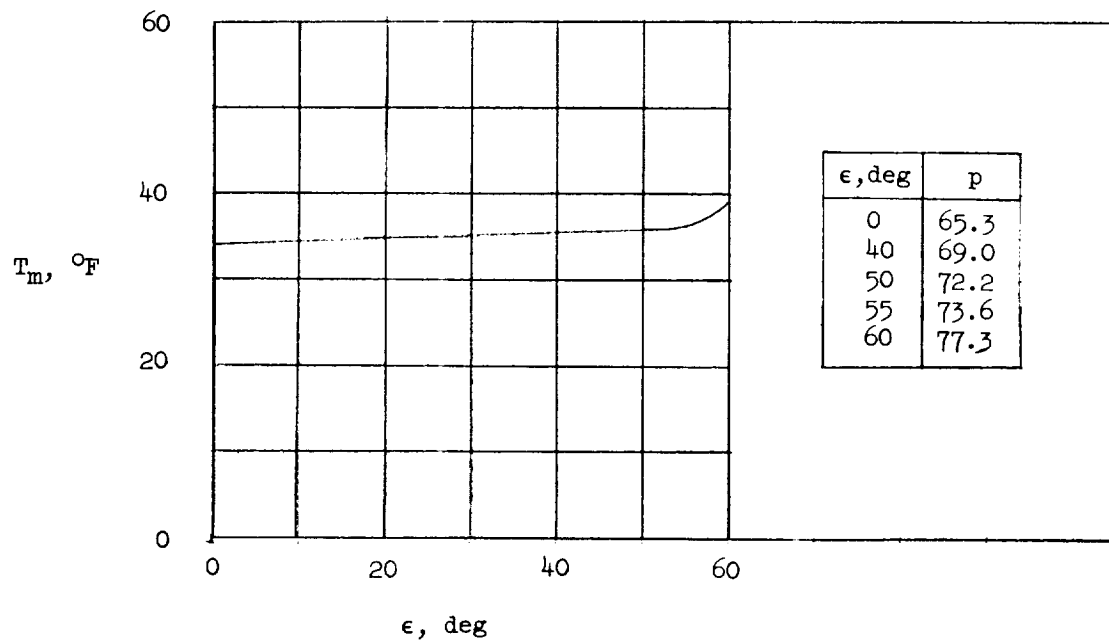
(a) $\zeta = 180°$; minimum area for tumbling condition.

ε, deg	p
0	63.0
40	68.5
50	75.6
55	80.2
60	95.9
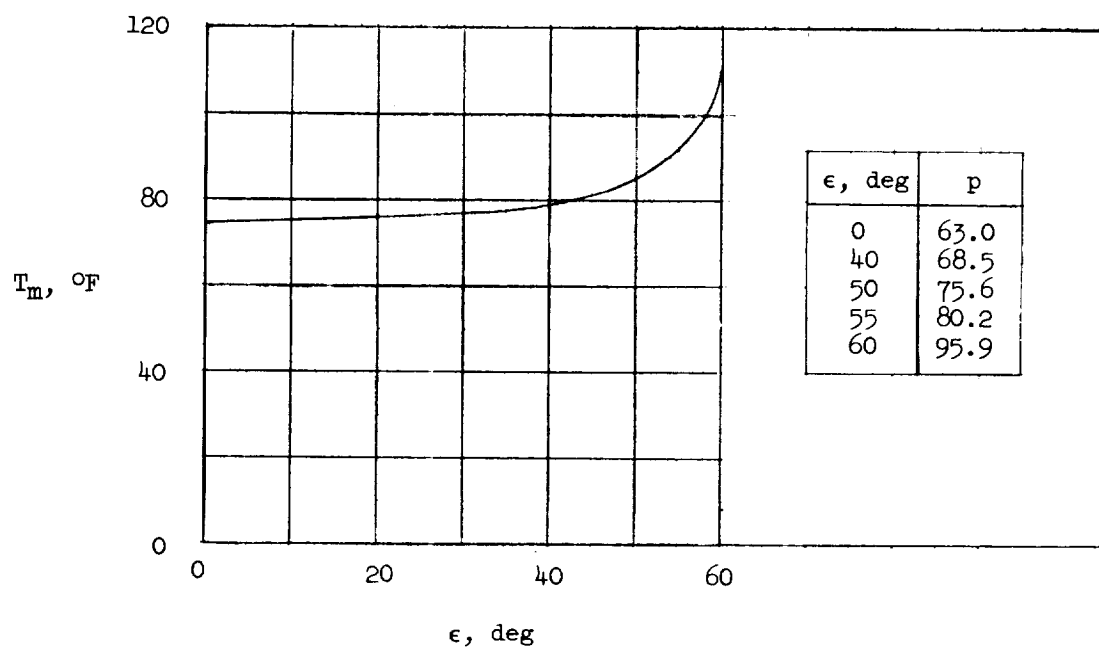
(b) $\zeta = 0°$; maximum area for tumbling condition.

Figure 28.- Mean temperature as a function of the orbit parameter ϵ.
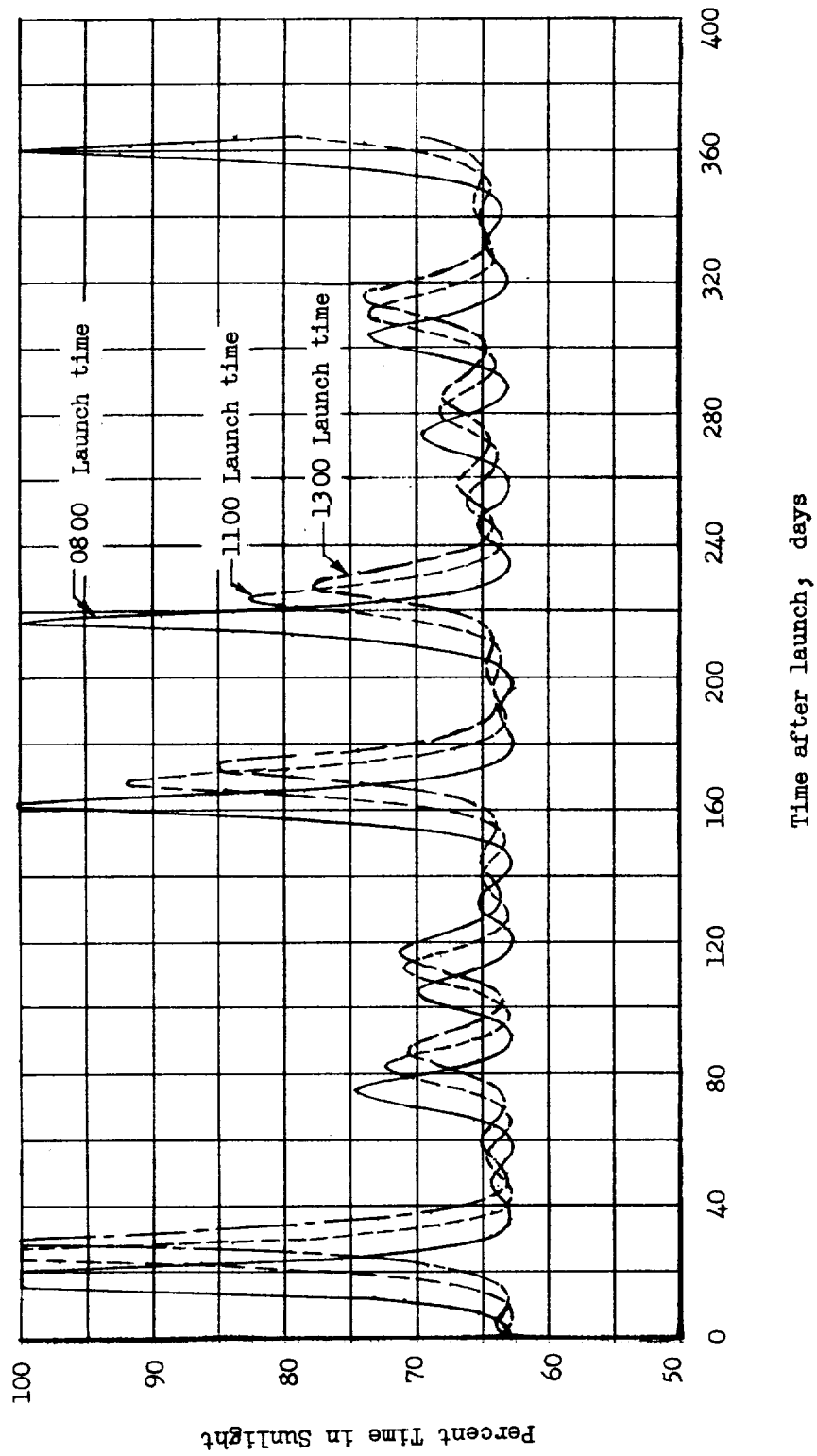
Figure 29.- Percent time in sunlight variation with days after launch.

L-1737

L-1737
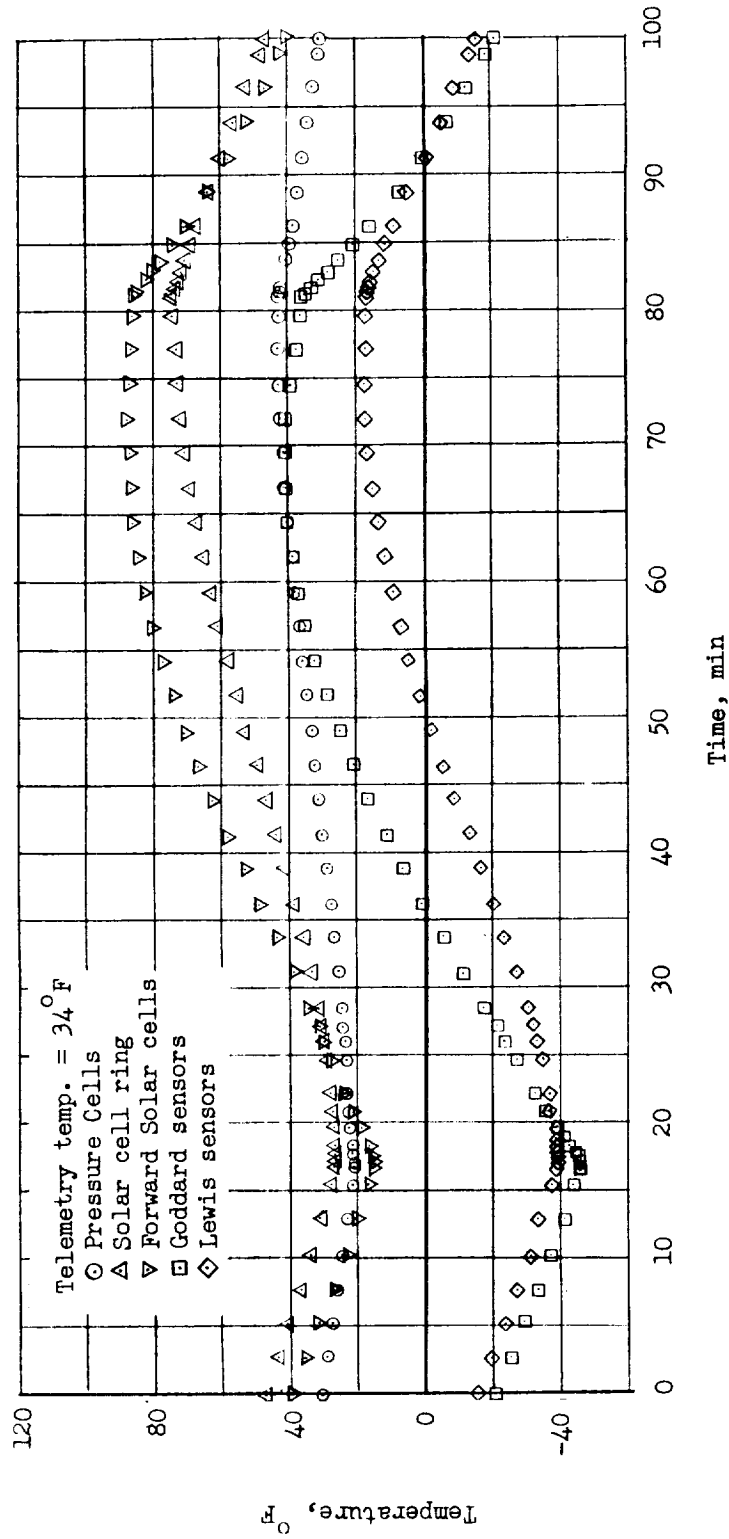
Figure 30.- Temperature time history for tumbling satellite for orbit producing lowest telemetry temperature.
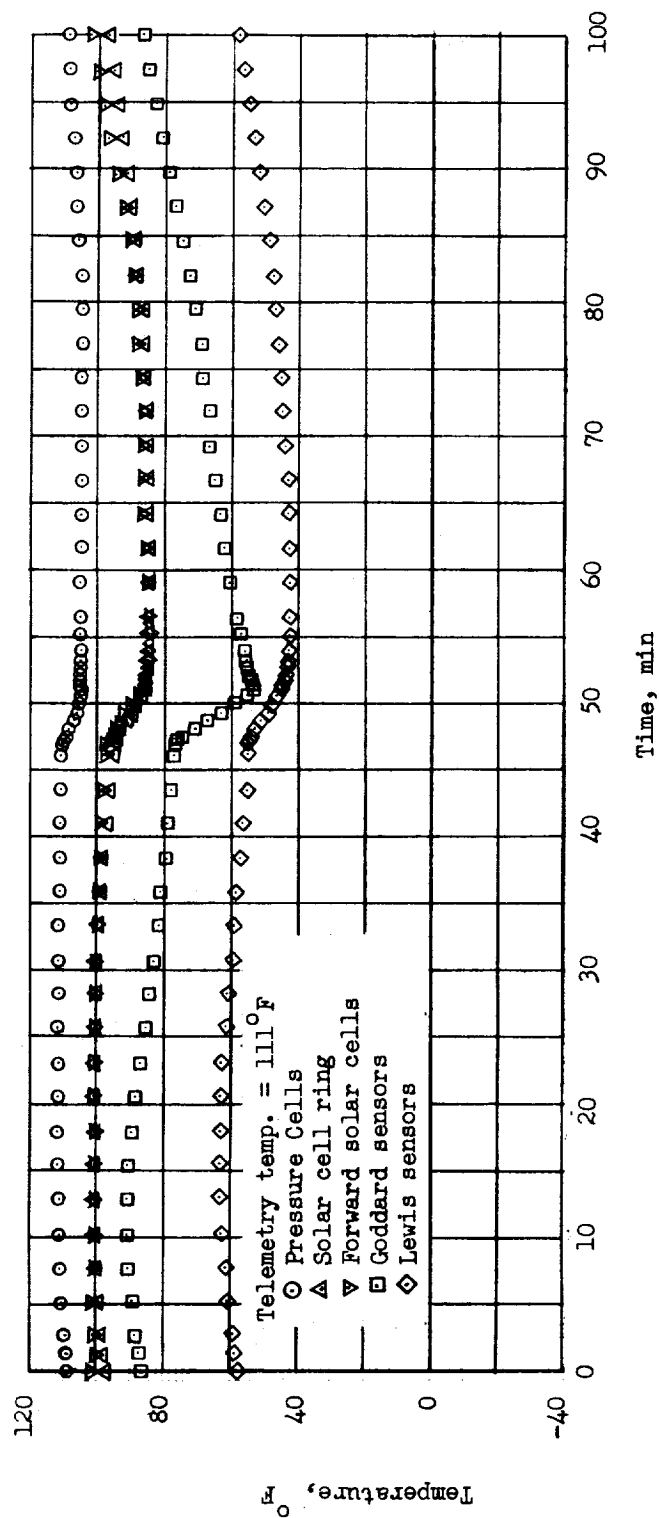
Figure 31.- Temperature time history for tumbling satellite for orbit producing highest telemetry temperature.

L-1737

L-1737
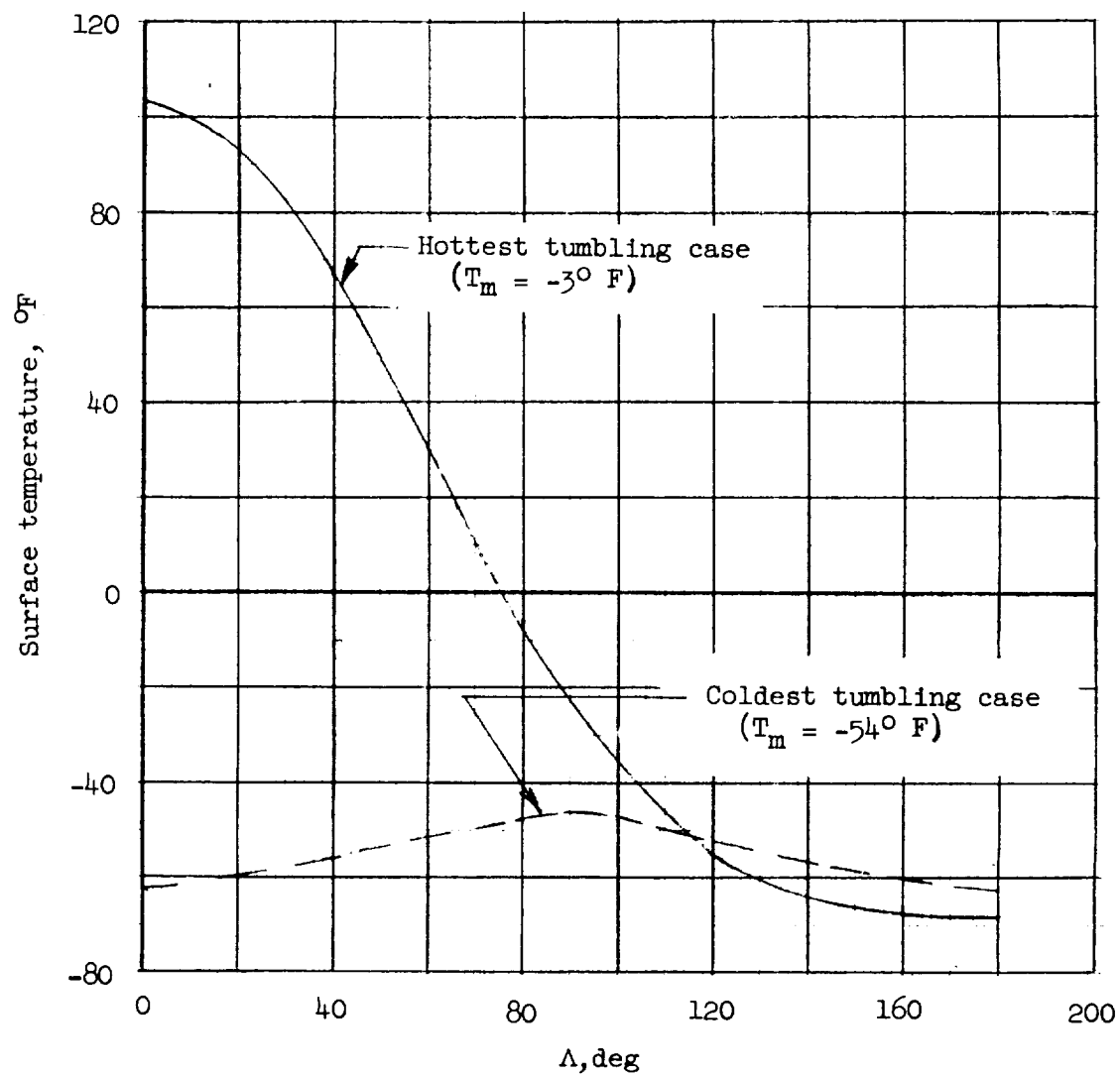
Figure 32.- Circumferential temperature distribution on Lewis sensors in hottest and coldest tumbling cases.
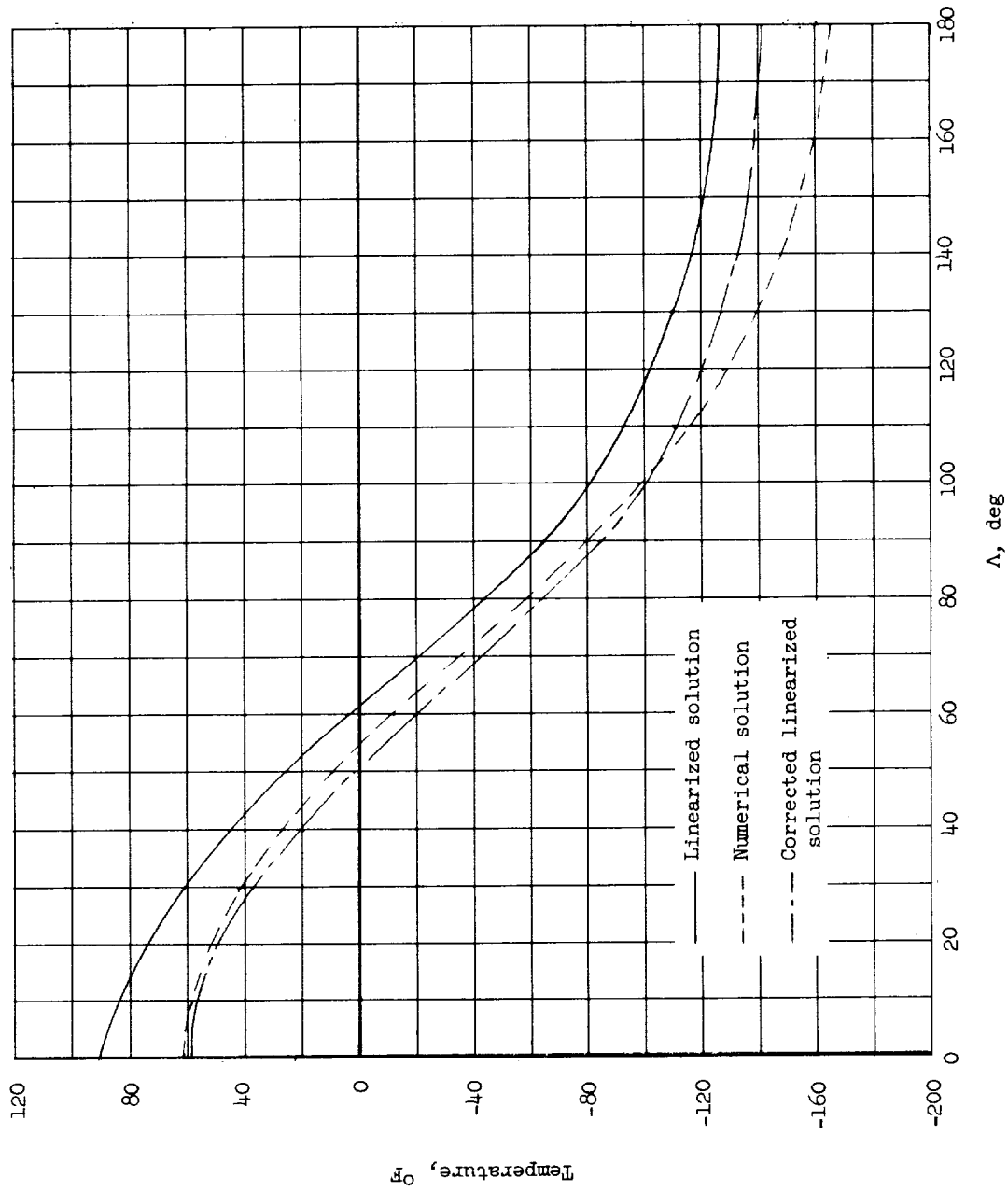
Figure 33.- Circumferential surface temperatures on an aluminum cylinder 0.02 inch thick.

L-1737
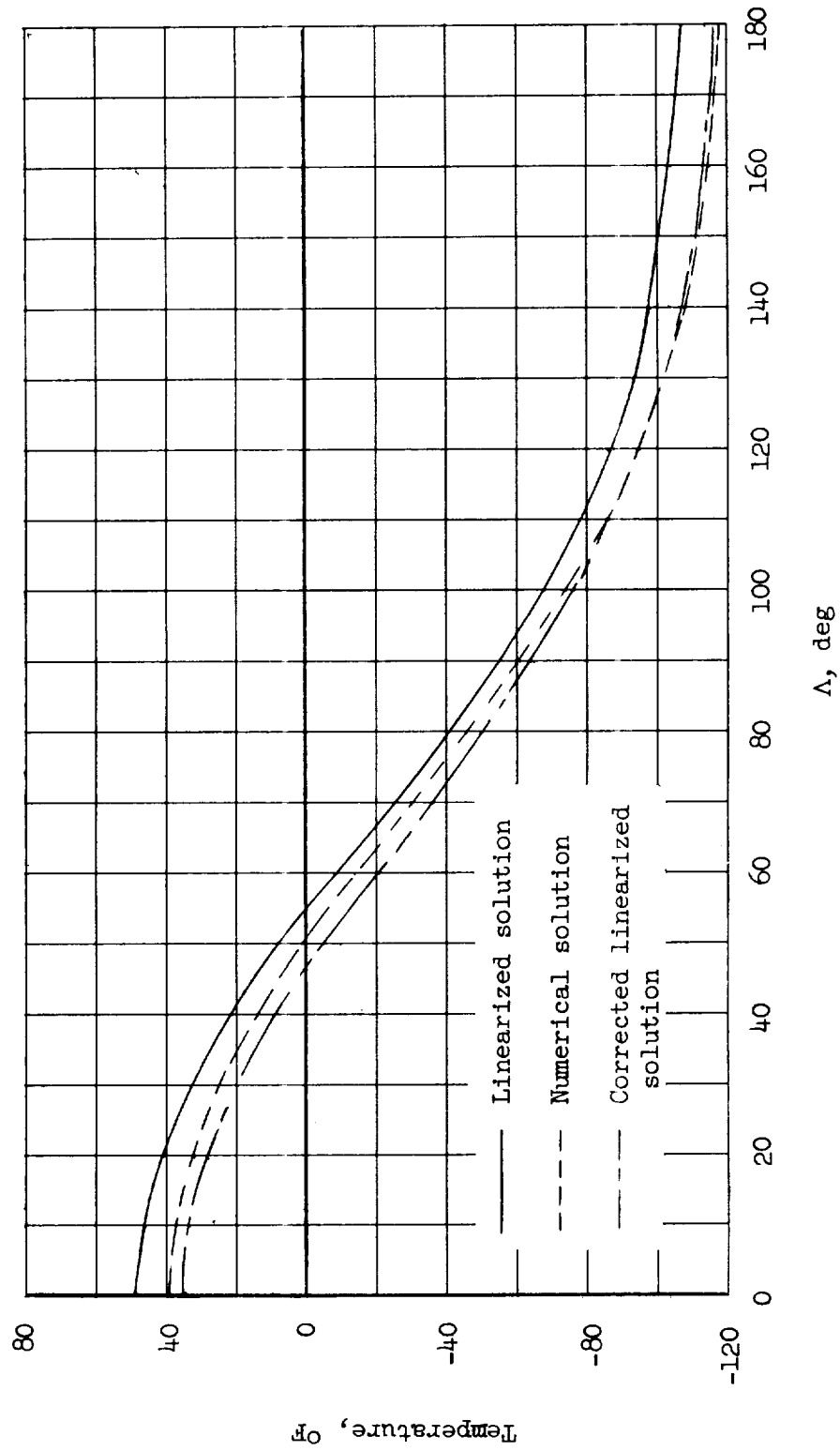
Figure 34.- Circumferential surface temperatures on an aluminum cylinder 0.04 inch thick.
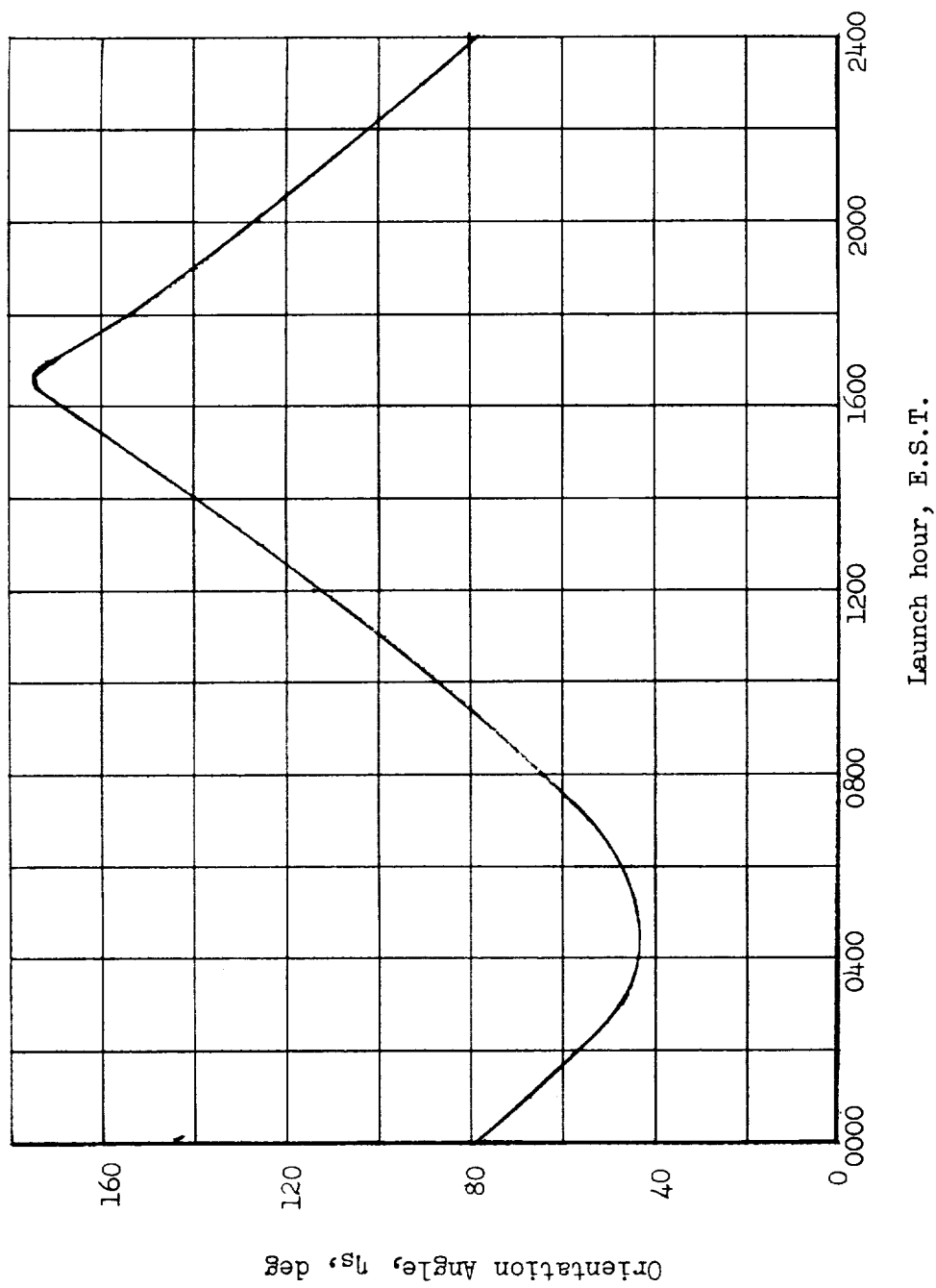
Figure 35.- Orientation angle as a function of launch time for a June 15, 1961, launch date.

L-1737

L-1737
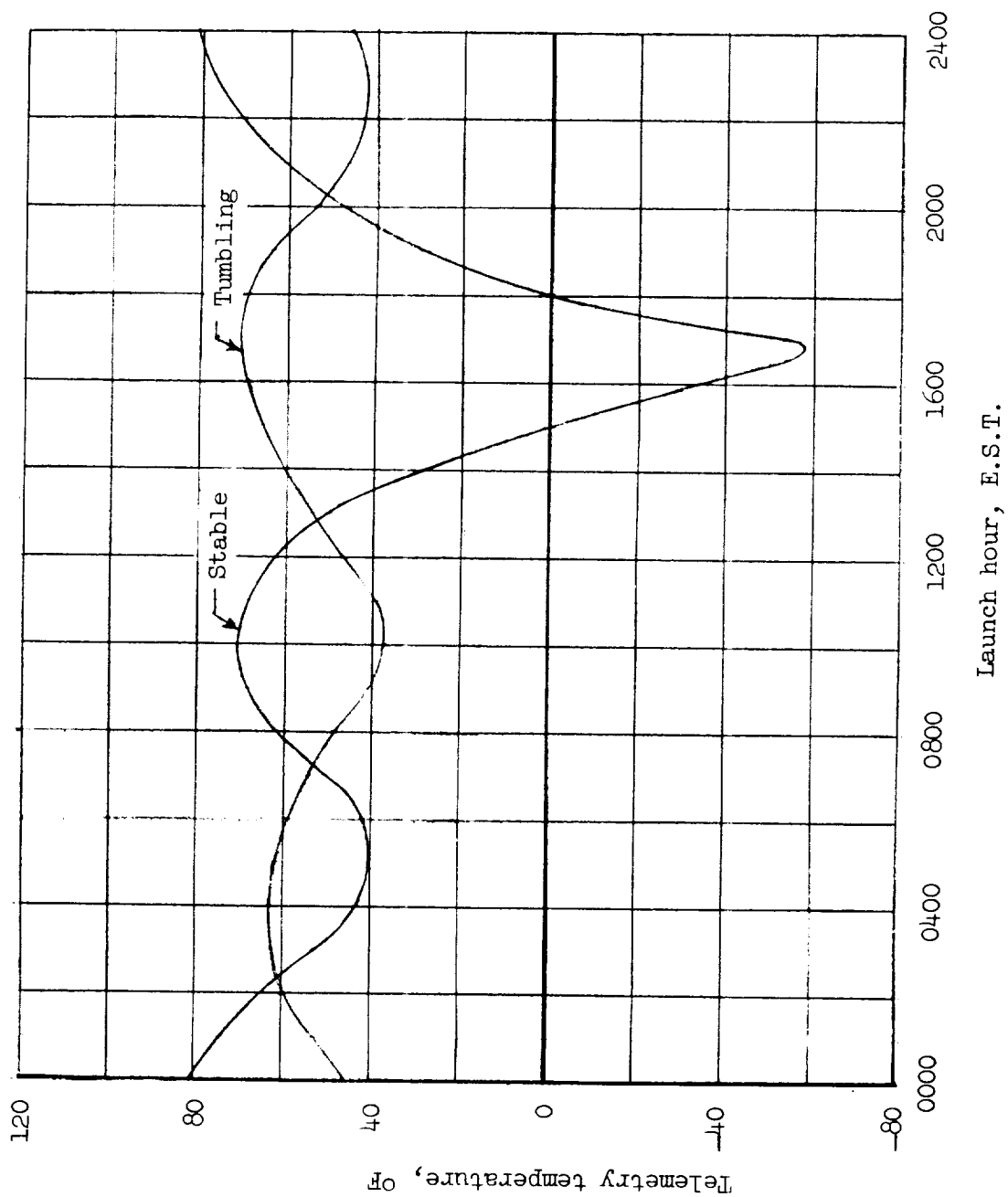
Figure 36.- Telemetry temperature as a function of launch time for a June 15, 1961, launch date.
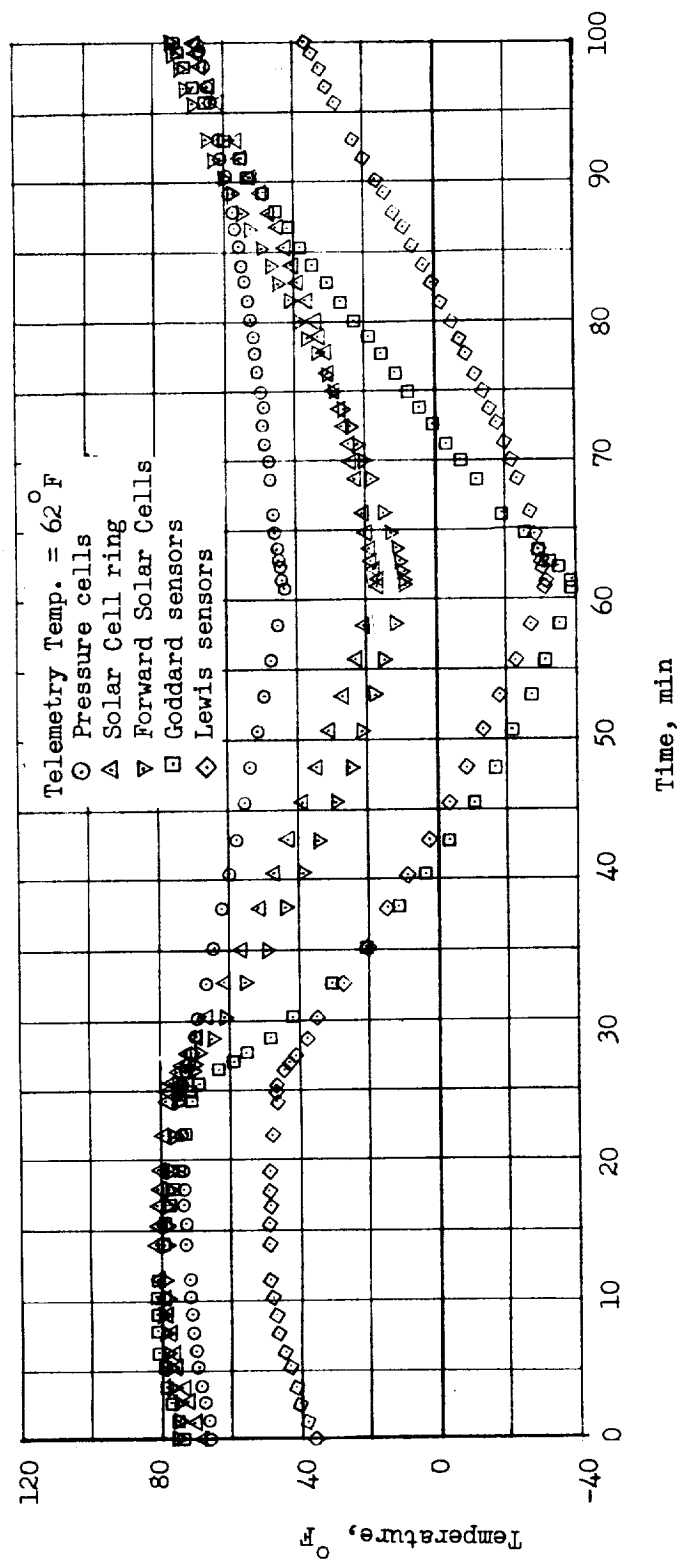
Figure 37.- Temperature time history for the stable satellite launched at 1200 hours on June 15, 1961.
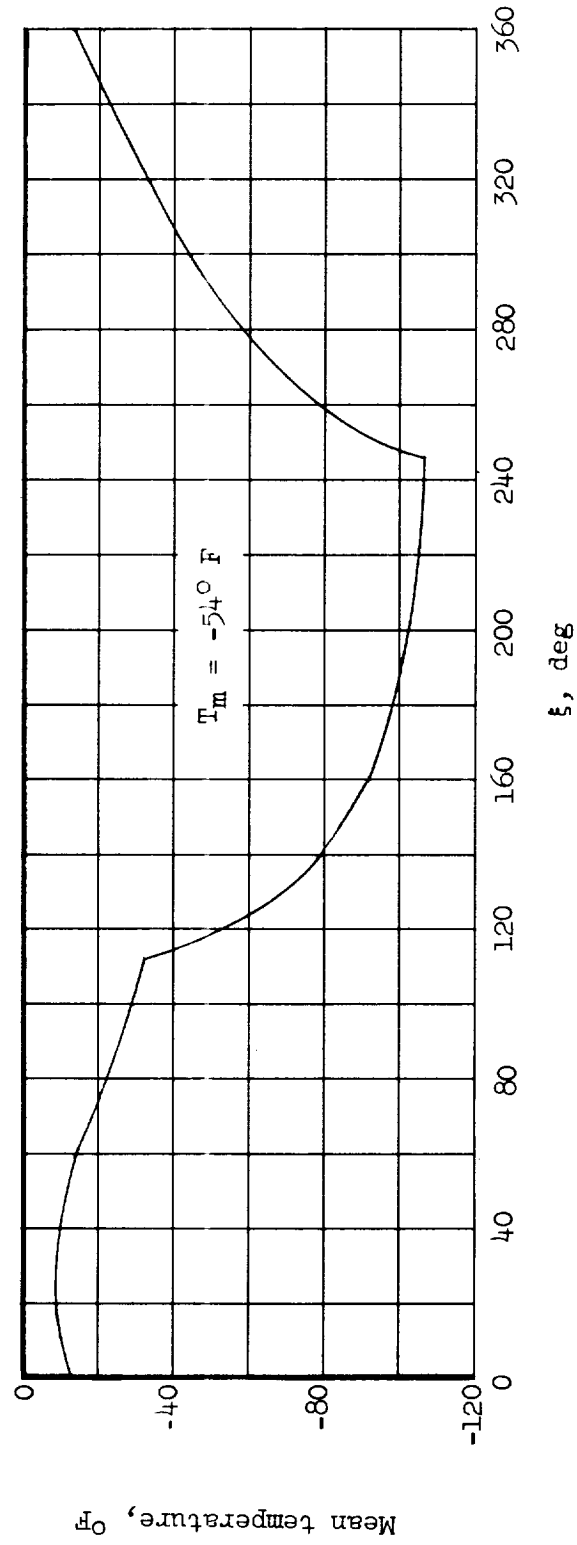
T-1737

Figure 38.- Mean surface temperature as a function of the orbit parameter ξ for an aluminum cylinder 0.02 inch thick (conductivity neglected).
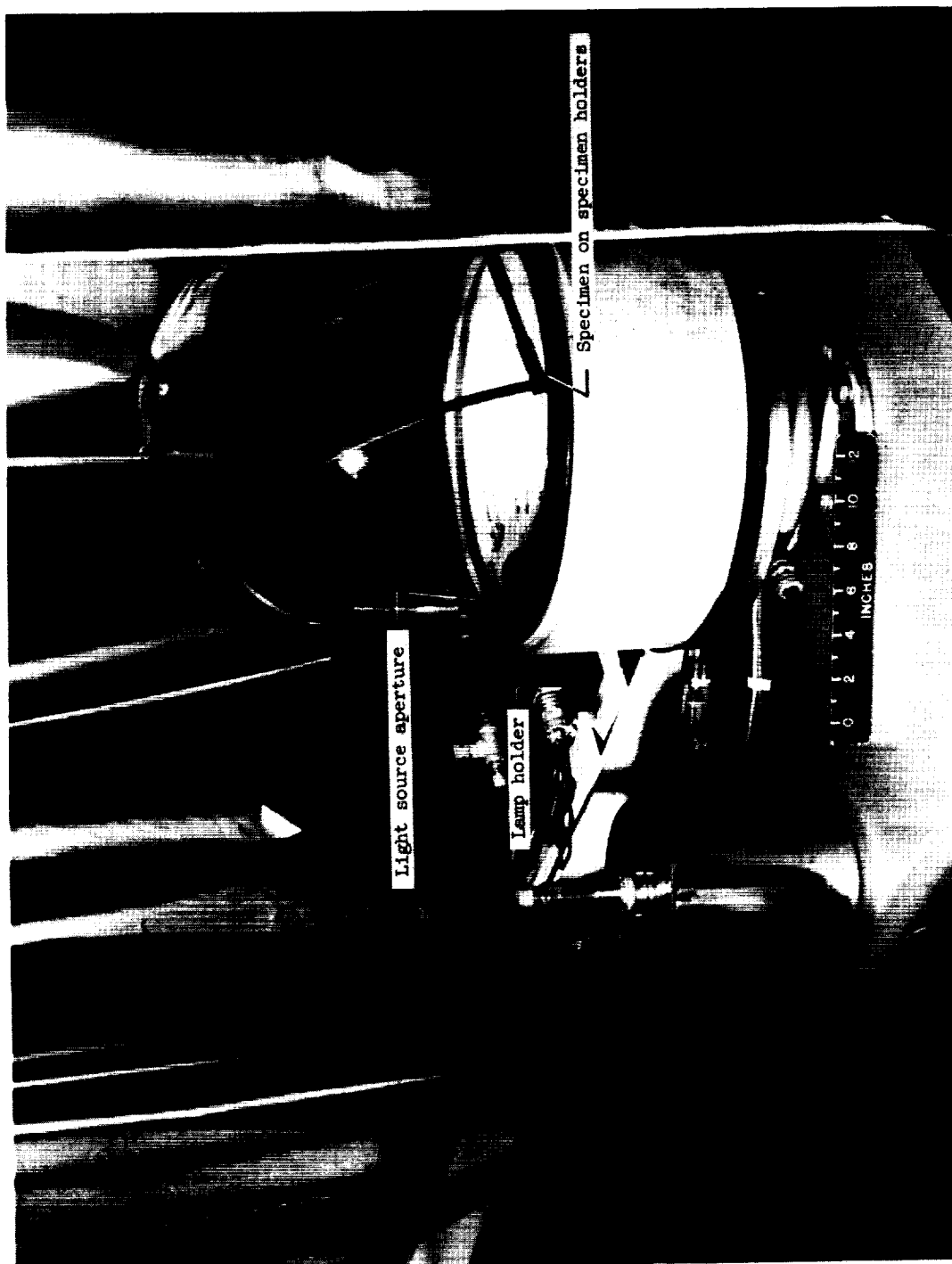
Figure 39.- Ultraviolet radiation test setup.   L-60-8654.1

L-1737